Coláiste na Tríonóide, Baile Átha Cliath
Trinity College Dublin
Ollscoil Átha Cliath | The University of Dublin

Fabrication of Surface-Porous Metallic Coatings by Cold Spray Additive Manufacturing and Their Applications in Heat Transfer

---

Yan Chen

Supervisor: Prof. Rocco Lupoi

Department of Mechanical, Manufacturing & Biomedical Engineering

Trinity College Dublin, the University of Dublin

2026

A thesis submitted to the University of Dublin in partial fulfilment of the requirements for the degree of

Doctor of Philosophy

Declaration

I hereby declare that this thesis represents my own work which has been done after registration at Trinity College Dublin, the University of Dublin, for the degree of the postgraduate programme, named Doctor in Philosophy in the Department of Mechanical, Manufacturing, and Biomechanical Engineering, and has not been previously included in a thesis or dissertation submitted to this or any other institution for a degree, diploma, or other qualifications.

Signed: ____________ Date: July 03, 2026

Abstract

This dissertation presents a systematic investigation into the formation mechanisms of surface open pore structures in cold spray solid state additive manufacturing and their functional application in boiling heat transfer enhancement. The objective is to establish an integrated research framework that spans from structural formation mechanisms to engineering performance validation. In response to the limitations of conventional porous heat transfer surfaces in terms of structural controllability, fabrication cost, and scalability, this work proposes a design pathway based on deposition non-uniformity in cold spray processing to enable both formation and controllable construction of surface open pore architectures.

Under identical cold spray processing conditions, a comparative study was conducted on Al, Cu, and Ti-6Al-4V (Ti64). The results demonstrate that only Ti64 spontaneously forms a honeycomb like surface open pore network during deposition. Cross sectional observations and three dimensional micro computed tomography reconstruction reveal that this structure originates from spatially selective bonding during the initial deposition stage. Owing to the high critical deposition velocity and intrinsic strength of Ti64, particle velocity dispersion leads to pronounced deposition non-uniformity. This non-uniformity is continuously inherited and amplified during multilayer accumulation, ultimately forming through thickness open channels and wall like skeletal structures.

On this basis, pool boiling heat transfer was employed as a performance evaluation platform to systematically investigate the functional behavior of cold sprayed porous Ti64 surfaces. Experimental results show that such surfaces significantly reduce nucleation superheat and enhance critical heat flux. The enhancement mechanism can be attributed to two primary effects. First, the cavity structures provide abundant and stable nucleation sites that promote early bubble generation. Second, the wall like skeleton acts as a geometric barrier to suppress lateral bubble coalescence, thereby delaying dry spot propagation and hydrodynamic instability. It was also observed that as coating thickness increases, the relatively low thermal conductivity of Ti64 introduces additional thermal resistance, partially diminishing the structural enhancement effect. This finding indicates a pronounced coupling between structural functionality and intrinsic thermophysical properties, highlighting the necessity of balancing pore structure enhancement and

conductive heat transfer pathways in optimized design.

To further achieve structural designability and material transferability, a substrate pre-treatment driven geometric regulation strategy was proposed. By pre-fabricating pore arrays and related structures on aluminum substrates, low deposition efficiency regions were intentionally introduced to guide the formation of controllable open pore networks during subsequent cold spray deposition. Through orthogonal experimental design and response surface analysis, the influences of pore diameter, pore spacing, and coating layer number on critical heat flux were systematically evaluated, establishing quantitative correlations among geometric parameters, structural morphology, and heat transfer performance. The results indicate that pore diameter and pore spacing are the dominant parameters, and appropriate matching can significantly enhance heat transfer performance while maintaining manufacturability.

Overall, this dissertation systematically elucidates the formation mechanisms and functional enhancement principles of cold spray induced surface open pore structures and establishes the intrinsic relationship among deposition behavior, structural evolution, and heat transfer performance. The findings provide both theoretical foundations and practical engineering pathways for the design and scalable fabrication of efficient boiling heat transfer surfaces with multiscale architectures and material adaptability.

Acknowledgements

Time passes swiftly, and my doctoral journey is now drawing to a close. Looking back on this period, from the initial stage of exploration and uncertainty upon joining the research group to the gradual development of research direction, the execution of experiments, and the completion of this thesis, I fully recognize that this achievement is not solely the result of individual effort. It has been shaped and supported by many people who have offered guidance, encouragement, and care along the way. Throughout these challenging and rewarding years, every step forward has been accompanied by the support of those around me. I would like to take this opportunity to express my sincere gratitude to all those who have contributed to my academic and personal growth.

First and foremost, I would like to express my deepest gratitude to my supervisors, Rocco Lupoi and Shuo Yin. During my doctoral studies, they provided invaluable guidance in defining research directions, structuring research frameworks, and developing rigorous scientific thinking. Their insightful advice on experimental design, data analysis, and academic writing greatly improved the quality of my research work and helped me to grow into an independent researcher. Beyond academic guidance, they also offered continuous support and understanding in my daily life, which enabled me to focus on my research with confidence while studying abroad. In times of difficulty and uncertainty, their encouragement and trust gave me the strength to persevere. Their mentorship, combining academic rigor with genuine care, has had a profound impact on both my professional development and personal growth.

I would also like to thank all members of our research group, especially the senior and junior colleagues represented by Tianqi Zhu. The group has provided a supportive and collaborative academic environment where ideas could be freely exchanged and discussed. Throughout my doctoral studies, I benefited greatly from numerous discussions, constructive feedback, and shared experiences. My colleagues offered valuable assistance in experimental techniques, equipment operation, and data processing, as well as thoughtful suggestions during the writing process. Through our joint efforts in learning and research, we not only enhanced our academic capabilities but also built lasting friendships. These shared experiences will remain among my most cherished memories of this journey.

My sincere thanks also go to my three close friends, Xinhao Guo, Qijian Deng, and

Shuqing Liu. They have accompanied me throughout many years of study and have witnessed my development from the early stages of my academic path to the completion of my doctoral degree. Whether through academic discussions or personal support, they have always been there for me. Their encouragement helped me maintain a positive mindset in the face of challenges, and their understanding and companionship provided strength during moments of uncertainty. This enduring and sincere friendship is one of the most valuable aspects of my life and will continue to inspire me in the future.

Finally and most importantly, I would like to express my deepest gratitude to my parents. Thank you for your unconditional support, understanding, and dedication throughout my life. You have always respected my choices and trusted me, allowing me to pursue my academic goals without hesitation. From the very beginning of my educational journey, you have quietly taken on every responsibility so that I could focus wholeheartedly on my studies. Your constant encouragement has given me the courage to overcome difficulties and continue moving forward. Your love and support are the foundation of everything I have achieved and the driving force that sustains me. No matter where I go in the future, I will always carry this gratitude with me and strive to repay your sacrifices through my actions.

I would like to extend my heartfelt thanks to everyone who has supported me throughout my academic journey. I will carry this sense of gratitude forward and continue to pursue excellence in the next stage of my life.

致谢

日就月将，学有缉熙于光明。从八岁走进小学课堂，到三十岁完成博士阶段的学习，回头一看，竟已走过二十二年的春秋。书桌换了无数张，身份一再变化，但始终没离开“学生”这两个字。所幸，这段漫长而曲折的求学之路，最终还是画上了一个圆满的句号。一路走来，并非全凭一己之力，心中有太多需要感谢的人。

温温恭人，维德之基。回望博士阶段的求学经历，我最深的体会，正是“为师者，以德立人”。Rocco Lupoi 老师待人温厚，却自有原则，与其相处，常常能感受到一种不动声色的力量。在学业上，老师给予了我极为扎实而细致的指导，从研究方向到具体问题，都耐心推敲、反复打磨；而在更关键的时刻，老师始终选择站在我这一边，给予信任与保护。多年求学，这是我第一次如此真切地感受到被老师“护着”的感觉，这份温和却坚定的支持，成为我能够安心投入研究的重要根基。也要感谢殷硕老师，在我人生的重要路口给予我清醒而诚恳的指引。无论是关于未来工作的选择，还是在学业之外如何更好地陪伴家人，老师都愿意花时间倾听与讨论，用自身的经验帮我看清方向。两位老师以不同方式诠释了“温”“德”二字。

嘤其鸣矣，求其友声。以鸟鸣相和喻知音相求。求学多年，幸得诸多同道相伴，使漫长而孤独的科研之路始终回荡着温暖的回声。首先，谨向 朱天齐，苏威铭等 STAM 课题组的师兄师姐师弟们致以诚挚感谢。你们在实验设计、数据分析、论文写作及学术讨论中的无私帮助，使我在每一次困惑与瓶颈之际都能得到启发与支持。无数次实验室的并肩奋战，不仅提升了我的科研能力，更让我体会到团队协作与学术共同体的力量。正是这种彼此回应、彼此托举的同行情谊，使“求其友声”不止是诗句，而成为真实可感的学术日常。其次，衷心

感谢李钰洋，熊义峰，金冰倩，宋宇石，张志强，王墅，陈德志等来自国内的访问学者。你们不仅在专业问题上给予我诸多指导，更在为人处世、待人接物以及跨文化环境中的沟通方式上给予我潜移默化的影响。你们的经验与从容让我学会在学术之外建立更成熟的心态与更开阔的视野，使我明白科研不仅是技术积累，更是人格与格局的修炼。最后，我要特别感谢葛进国等师兄。从本科阶段起，你们便带领我走进科研世界，在最初懵懂之时给予方向与信心。从如何阅读第一篇论文，到如何独立思考科研问题，你们的引导贯穿我学术道路的起点与延续。回望来路，我今日的每一步成长，都与当年的耐心指点与鼓励密不可分。同行有声，前路不孤。谨以此致谢，铭记一路相伴的同窗之情。

棠棣之华，鄂不韡韡。花萼相映，喻同道相扶。感谢穆高林，程江稳，田野等曾并肩共事的前同事。虽自离开团队已逾四载，但彼此情谊未尝稍减，反而在时间沉淀中更显珍贵。你们始终与我保持联系，持续分享行业最新进展与前沿动态，使我在学术与产业之间得以保持清晰而开阔的视野；在我此次求职过程中，更是给予了毫无保留的支持与鼓励，从信息建议到经验交流，处处体现出真诚与信任。回望过往共事岁月，许多默契与理解早已超越了具体事务本身，成为彼此成长道路上的长久助力。亦由衷期望，未来在新的工作阶段中，仍能与诸位再度携手，在不同的平台上延续这份相知相助的合作情谊。

愿岁并谢，与长友兮。岁月更迭而情谊长存。谨以此句，感谢郭新浩，邓琦键，刘树青三位挚友。自高中相识至今，同行多年，从青涩年少到各自奔赴人生不同阶段，你们始终在我的求学之路上风雨相伴。无论是学业上的困惑与压力，还是生活中的欢欣与低落，总有你们可以倾诉、可以分享。许多时刻的支持并不张扬，却在漫长岁月中

成为最坚定而温暖的依靠。这些年走过的路，也许方向不同、步伐各异，但彼此从未缺席。正是这种不言而喻的信任与陪伴，让我在面对未知与挑战时始终心有归处。感谢你们在每一个重要或平凡的时刻都在身旁，亦愿未来岁月流转，我们仍能如往昔一般，守望彼此，长久相伴。

父兮生我，母兮鞠我。谨以此句致谢我最深沉也最无言的依靠——我的父母。多年来，无论我身处何地、面临何种选择，你们始终是我最坚强的后盾。你们常说的一句“实在不行，回家也行”，看似平常，却给予了我莫大的安心与底气。正因为知道身后永远有一个不设条件的归处，我才得以在求学与人生的道路上不断尝试、不断前行，在犹豫时敢于选择，在困难时不至退缩。你们或许并未参与我的具体研究，却以最朴素而恒久的方式支撑着我走到今天。那些未曾言说的牵挂、理解与包容，早已融入我每一步的勇气之中。此心所系，无以为报，唯愿岁月温柔，以平安顺遂相酬。

需要感谢的人实在太多，恕不一一列举，但这份心意同样献给所有给予我帮助与关怀的你们。

承志以远，行当笃定而致新。博士阶段的完成，并非抵达终点，而更像一次长程行旅中的驿站回望。过往数年的学习与探索，既是积累，亦是沉淀；而未来的道路，仍在缓缓展开。愿自己在新的阶段中，仍能秉持求知之心与从容之志，于时光流转之间，持续精进，不负所学。

List of publications

1. Chen Y, Garivalis A I, Shatskiy E, Robinson A J, Di Marco P, Yin S and Lupoi R 2025 Nucleate pool boiling enhancement on Ti64 cold spray additive manufacturing coatings Appl. Therm. Eng. 277 (Chapter 3 & Chapter 4)
2. Chen Y, Kangude P, Shatskiy E, Liu S, Ge J, Zhu T, Robinson A, Yin S and Lupoi R Hole array aluminum coatings fabricated by cold spray for enhanced boiling heat transfer surfaces (Chapter 5, Under Review)
3. Garivalis A I, Chen Y, Shatskiy E, Robinson A, Marco P Di and Lupoi R 2024 Enhanced Pool Boiling Heat Transfer with Porous Ti-6Al-4V-Coatings Produced by Cold Spray Metal Additive Manufacturing J. Phys. Conf. Ser. 2766 (Chapter 3 & Chapter 4)
4. Chen T, Yu P, Li Y, Chen Y, Yang C, Lupoi R, Yin S and Zhang X 2025 High speed impact induced dehydrogenation of titanium hydride and formation of cellular structure via cold spray Scr. Mater. 256 1–6 (Characterization, Data Analysis)
5. Zhang N, Wang Y, Huang C, Yang B and Chen Y 2026 Ductility Control in Laser Powder Bed Fusion (LPBF) AlSi10Mg via Silicon Precipitation and Coarsening During Heat Treatment 1–20 (Characterization, Data Analysis)
6. Ge J, Wu H, Liu H, Zhu Y, Chen Y, Zhan W and Zhang L 2025 Anisotropic Behavior in Microstructures and Properties of Refractory Tungsten Metal Produced by Laser Powder Bed Fusion 1–18 (Characterization, Data Analysis)
7. Liu H, Ge J, Zhang Y, He J, Chen Y, Zhang Y, Liu Z and Yin S 2025 Study of microstructural evolution and mechanical performance of selective laser melting pure tungsten deposit for process parameter optimization J. Mater. Res. Technol. 38 3909–25 (Characterization, Data Analysis)
8. Xiong Y, Zhang F, Huang Y, Dai T, Wan Q, Chen Y and Yin S 2025 A novel composites of laser 3D printed CoCrFeNiMn/Ti6Al4V lattice structure with B4C/AlSi10Mg interpenetrating phases Compos. Part A Appl. Sci. Manuf. 188 108579 (Characterization, Data Analysis)
9. Xiong Y, Zhang F, Huang Y, Dai T, Wan Q, Chen Y and Yin S 2024 Achieving superior strength-ductility combination in the heterogeneous microstructured Ti64 alloy via multi-eutectoid elements alloying with CoCrFeNiMn during laser powder bed fusion Virtual Phys. Prototyp. 19 (Characterization, Data Analysis)

10. Jin B, Nie S, Fan N, Xing B, Yu H, Chen Y, Zhu X, Yin S and Zhang N 2024 Enhanced wear resistance of a multi-phase reinforced Al0.5CrFeNi2.5Si0.25 high-entropy alloy via annealing J. Mater. Res. Technol. 29 5180–8 (Characterization, Data Analysis)
11. Jin B Q, Yu H S, Nie S N, Xing B W, Chen Y, You J Q and Zhang N N 2024 Effect of Si on evolution of microstructure and wear resistance of Al0.5CrFeNi2.5 high-entropy alloy fabricated via laser melting deposition J. Iron Steel Res. Int. 0123456789 (Characterization, Data Analysis)
12. Liu H, Ge J, Zhao G, Chen Y, Yue G, He S, Zhan W, Zhang Y and Liu Z 2024 An Investigation on Microstructural Characteristics and Comprehensive Performances of Equiatomic Ratio NiTi Shape-Memory Alloy Produced by Selective Laser Melting Adv. Eng. Mater. 2401245 1–12 (Characterization)

Contents

Declaration I

Abstract....III

Acknowledgements V

致谢 VII

List of publications X

Contents XII

List of figures XVI

List of tables XX

Symbols XXI

Chapter 1 Introduction....1

Chapter 2 Literature review....7

2.1 Cold spray technology....7

2.1.1 Metal additive manufacturing technology....7

2.1.2 Overview of cold spray 8

2.1.3 Principle and characteristics of cold spray 9

2.1.4 Deposition behaviour and bonding mechanism during impact of cold spray 14

2.1.5 Influential factors for cold spray 21

2.2 Porous structures in additively manufactured materials....26

2.2.1 Classification of porosity....26

2.2.2 Porosity formation in additive manufacturing....34

2.3 Boiling heat transfer 45

2.3.1 Introduction of the boiling heat transfer....45

2.3.2 Heat transfer curves....48

2.3.4 Influence of heat transfer surface properties 51

2.4 Summary for research gap 52

Chapter 3 Formation mechanism and microstructural evolution of porous Ti64 structures via cold spray 56

3.1 Material and methodology 58

3.1.1 Feedstock powder and cold spray process 58

3.1.2 Microstructure characterization 60

3.1.3 Mechanical properties 60

3.1.4 Uncertainty analysis 61

3.2 Microstructural and pore distribution characteristics 62

3.2.1 Cell–wall porous structure formation during cold spray 65

3.2.3 Micro-CT analysis of the internal architecture 71

3.3 Analysis of single-particle velocity dispersion and Its mechanism 74

3.4 Mechanical properties 77

3.4.1 Nanoindentation characterization of regional mechanical properties 77

3.4.2 Tension test 80

3.4 Summary 82

Chapter 4 Study on boiling heat transfer performance of porous Ti64 surfaces produced by cold spray 85

4.1 Experimental setup and testing methods 87

4.1.1 Raw material and cold spray process 87

4.1.2 Microstructure characterization 88

4.1.3 Pool boiling test facility and experimental procedures 88

4.1.4 Pool boiling test procedures 91

4.2 Surface characteristic analysis 92

4.2.1 Surface properties 92

4.2.2 Roughness 94

4.2.3 Tomographic reconstruction 96
4.2.4 Wettability...97
4.3 Pool boiling heat transfer...98
4.3.1 Validation of experimental apparatus 98
4.3.2. Pool boiling heat transfer performance 101
4.4 Bubble behavior during the boiling process 104
4.5 Comparison with other additive enhancement techniques 107
4.6 Summary...107
Chapter 5 Investigation of controlled patterned cold spray coating preparation and heat transfer performance based on surface pretreatment 109
5.1 Material and methodology..111
5.1.1 Feedstock powder and cold spray process...111
5.1.2 Microstructure characterization 113
5.2 Comparison of surface-pretreated coatings with different patterns and their heat transfer performance 114
5.2.1 Surface pretreatment methods and coating construction for different patterns 114
5.2.2 Comparison of boiling heat transfer performance for patterned coatings 115
5.3 Preparation of porous array coatings and enhancement of heat transfer performance 117
5.3.1 Surface characteristic analysis 117
5.3.2 Analysis of boiling heat transfer performance.......................................125
5.3.3 Bubble behavior during the boiling process 127
5.3.4 Influence of parameters 129
5.4 Comparison with other additive enhancement techniques 130
5.4 Summary...131

Chapter 6 Conclusion and prospects 134
6.1 Conclusion 134
6.2 Further work 136
Reference 139
Supplementary materials 162

List of figures

Figure. 1 Additive manufacturing (AM) in a broad sense (the inner parts show the AM processes in a narrow sense)

Figure. 2 Schematics of the main components of CS system

Figure. 3 Particle velocity over particle temperature with window of sprayability (WS) and the regime of particle impact conditions (PIC)

Figure. 4 Cold spray in the surface engineering space. CS cold spray, PVD physical vapor deposition, CVD chemical vapor deposition

Figure. 5 Stages of coating formation in the cold spray process

Figure. 6 Evolutions of equivalent plastic strain (PEEQ, left side) and temperature (TEMP , right side) of a 40μm Cu particle impacting upon a Cu substrate at the impacting velocity of 310m/s

Figure. 7 CS-ed Al particle on steel substrate: a) cross-sectional images after 180º rotation and milling; b) magnified image at the marked region in (a)

Figure. 8 Melting in CS: a) Ti particle successfully deposited onto a previously deposited layer; b) local melting under higher magnification of the boxed areas in (a)

Figure. 9 The time evolution of particle and the substrate shapes during impact of a 25-μm Cu particle onto the Cu substrate at 550 m/s: a) 4.4 ns; b) 13.2 ns; c) 22.0 ns and d) 30.8 ns

Figure. 10 In-situ observation of the bonding moment in microparticle impact. Multi-frame sequences with 5 ns exposure times showing 45-μmAl particle impacts on Al substrate at 605 m/s (top) and 805 m/s (bottom), respectively below and above critical velocity. Material jetting is indicated with white arrows

Figure. 11 Schematic diagram of particle impacting and bonding processes in cold spraying

Figure. 12 Schematic dimensions of cold spray nozzle geometry

Figure. 13 a) A small supersonic nozzle, b) a copper deposit on aluminum substrate cold sprayed by it

Figure. 14 Non-dimensional chart showing the effect of standoff distance on deposition efficiency. Note that Fd is the drag force, Mc is the centerline Mach number, Vg is the gas velocity, Vi is the particle impact velocity and Vp is the in-flight particle velocity

Figure. 15 Setup of different spray angles in one spray run

Figure. 16 Cross-sectional OM micrographs of the Ti coating deposited on the Cu substrate at different spray angles

Figure. 17 The relationship between particle impact velocity and critical velocity and particle size distribution in cold spray

Figure. 18 Microporosity in different additive manufacturing processes

Figure. 19 Mesoroporosity in different additive manufacturing processes

Figure. 20 Macroporosity during Cold Spray Processes

Figure. 21 Fabrication of diverse porous structures using LPBF

Figure. 22 Fabrication of diverse porous structures using DED

Figure. 23 Fabrication of diverse porous structures using CS

Figure. 24 Effect of boiling heat transfer at different stages

Figure. 25 1-a), 2-a), 3-a) Low magnification SEM characterization of the gas atomized Al, Cu and Ti64 amorphous powder for cold spray process. 1-b), 2-b), 3-b) High magnification SEM characterization of the gas atomized Al, Cu and Ti64 amorphous powder for cold spray process. 1-c), 2-c), 3-c) Particle size distribution of the Al, Cu and Ti64 powder

Figure. 26 In-house cold spray system in Trinity College Dublin

Figure. 27 Deposition Behavior of Cold Spraying for Different Materials

Figure. 28 a) Macroscopic and local magnification (30x) of the surface of the openings prepared by cold spray. b) Cross-section and top view of the cold sprayed one and four layers deposited samples

Figure. 29 Eight cross sections of the cellular structure from interface toward the top of the deposit

Figure. 30 Schematically illustrates the typical single particle responses of Ti 6Al 4V particles impacting an Al6082 substrate at different impact velocities during the cold spray process

Figure. 31 a) Nanoindentation SEM Images and Hardness Distribution Maps, b) Average hardness values across different regions

Figure. 32 SEM image of Ti64 coating fracture surface

Figure. 33 a) Cross-sectional schematic of the pool boiling apparatus and b) Enlarged view of the heater assembly.

Figure. 34 Images of the surface morphology of boiling samples fabricated via cold spraying for this study. Photographs of the boiling samples (a,b,c,d,e,f). Scanning electron microscopy (SEM) images of the sample surfaces (a-1,b-1,c-1,d-1,e-1,f-1). Magnified view of the region highlighted by yellow dashed lines in panel (a-2,b-2,c-2,d-2,e-2,f-2)

Figure. 35 White Light Interferometry images of tested boiling surfaces**Figure. 36** (a) Micro-CT reconstruction of the coating for Sample 2800-51-4 (b) Localized magnification showing internal voids

Figure. 36 a) Micro-CT reconstruction of the coating for Sample 2800-51-4, b) Localized magnification showing internal voids

Figure. 37 Snapshot of FC-72 droplet impinging on the surface of Sample 2800-51-4

Figure. 38 Boiling curves of the bare sample in saturated FC-72 compared with published data and the Zuber correlation

Figure. 39 a) Boiling curves of all tested surfaces. b) Effective boiling heat transfer coefficient versus heat flux. c) Boiling curves adjusted for coating thickness. The CHF is indicated with arrow.

Figure. 40 Behaviour of bubbles on the boiling surfaces at different heat fluxes

Figure. 41 a) SEM characterization of the gas atomized pure Al amorphous powder for cold spray process. b) Particle size distribution of the pure Al powder

Figure. 42 Surface and cross-sectional morphologies of coatings deposited by cold spray on substrates with different pretreated surface patterns

Figure. 43 Boiling curves (left) and heat transfer coefficient (right). CHF location is indicated with an arrow

Figure.44 a) Macrophotograph of the boiling surface, b) SEM image of the boiling surface at 30× magnification, c) SEM image of the boiling surface at 60× magnification

Figure. 45 a) 25 cross-sectional photographs from the substrate to the top of the coating, b) three-dimensional morphology reconstruction photographs and local enlargement images

Figure. 46 White Light Interferometry images of tested boiling surfaces

Figure. 47 Pool boiling curves obtained for representative samples

Figure. 48 Bubble behaviour during boiling at different heat flux levels

Figure. 49 Standardized Pareto chart and response surface analysis of the effects of hole diameter (D), Pitch (P), and coating layer number on CHF

Figure. 50 Boiling curve test results for all samples

List of tables

Table.1 Summary of Pore Material Preparation via different Additive Manufacturing

Table.2 Cold Spray Parameters for Different Powders

Table.3 Experimental parameters in cold spray process

Table.4 Measured properties of the samples

Table.5 Orthogonal design matrix for Diameter (D), Pitch (P), and Number of Layers

Table.6 Surface roughness, coating thickness, and specific surface area of the tested samples.

Table.7 Comparison with other research

Symbols

h	Heat transfer coefficient	W/(m2·K)
k	Thermal conductivity	W/(m·K)
q''	Heat Flux	W/m2
S	Coating thickness	m
T	Temperature	°C
x	Length	m
ΔT	Temperature difference	K
Δx	Distance	m
ε	Measurement error	-

Subscripts

Cu	Copper
Al	Aluminium
Ti	Titanium
sat	Saturation
$wall$	Wall

Acronyms

CT	Computed Tomography
CHF	Critical Heat Flux
HTC	Heat Transfer Coefficient
SEM	Scanning Electron Microscopy
TS	Travelling Speed
PFR	Powder Feed Rate
WLI	White Light Interferometry
AAR	Actual area ratio

Chapter 1 Introduction

With the rapid advancement of high–power-density electronic devices, advanced energy systems, and multiphase heat-transfer equipment, interfacial heat-transfer performance has gradually emerged as a critical factor limiting overall system performance and reliability. Among various heat-transfer enhancement strategies, regulating interfacial transport processes through surface structural design is widely regarded as a solution that combines strong physical effectiveness with engineering feasibility. A substantial body of research has demonstrated that surfaces featuring porous or multiscale structures can markedly promote bubble nucleation and detachment during boiling, while simultaneously suppressing lateral bubble coalescence in the transition boiling regime. As a result, such surfaces exhibit outstanding performance potential in applications involving boiling heat transfer, evaporative cooling, and multiphase flows. Consequently, the controllable and scalable fabrication of functional porous surfaces has become an important research topic in surface engineering and advanced manufacturing.

Despite the well-recognized advantages of porous structures in enhancing interfacial transport, their practical fabrication remains challenging. On the one hand, conventional approaches such as chemical etching, sintering, or templating can generate porous features to some extent, yet precise control over pore size distribution, spatial uniformity, and structural stability is often difficult to achieve. On the other hand, additive manufacturing technologies based on melting–solidification mechanisms, such as selective laser melting or electron beam melting, offer a degree of geometric design freedom but are constrained by high thermal input, high cost, and limited processing area, which restrict their applicability to large-area functional surfaces. From a manufacturing science perspective, the development of a low-cost, scalable method that can naturally generate porous structures is t`herefore of great significance for the engineering deployment of porous functional surfaces.

Cold spray, as a representative solid-state additive manufacturing technique, accelerates powder particles to supersonic velocities via a high-speed gas–solid flow and achieves deposition through particle impact onto a substrate under fully solid-state conditions.

Unlike conventional thermal spray or fusion-based additive manufacturing processes, particles in cold spray do not undergo melting; instead, deposition is governed primarily by severe plastic deformation induced by high-velocity impact and subsequent interfacial bonding. This solid-state nature endows cold spray with notable advantages in avoiding oxidation, phase transformation, and thermal damage, while also imparting distinct deposition kinetics. Notably, cold spray does not always result in uniform and continuous deposition under all conditions. Particularly during the initial deposition stage, whether particles can successfully adhere to the substrate depends strongly on local impact conditions and material properties. This coexistence of "successful" and "failed" deposition provides a potential physical basis for the formation of porous structures.

In existing cold-spray studies, most efforts have focused on producing dense coatings through process optimization, whereas regions associated with deposition failure and their structural implications have received limited attention. However, for material systems with high strength and high critical deposition velocity, such as Ti-6Al-4V (Ti64) titanium alloy, cold spray inherently exhibits low initial deposition efficiency. During the early stages of deposition, only certain regions satisfy the critical conditions required for effective particle bonding, while particles impacting other regions rebound or fragment, preventing continuous deposition. This spatially selective deposition behavior is not a random defect but rather a material-governed characteristic dictated by intrinsic mechanical properties, resulting in the spontaneous formation of surface porosity with non-uniform length-scale distribution.

Although cold spray technology has traditionally been employed for the fabrication of dense coatings and additively manufactured components, materials with relatively high critical deposition velocities, such as Ti-6Al-4V, often exhibit pronounced deposition inhomogeneity and low deposition efficiency during the initial stages of deposition. Conventional studies have generally regarded this phenomenon as a detrimental factor affecting deposition quality, while its potential value for the fabrication of functional structures has remained largely unexplored. The present study reveals that such deposition inhomogeneity, arising from selective particle bonding, can naturally generate surface-open porous structures during the cold spray process. Accordingly, this thesis addresses the following central scientific question: can the intrinsic inhomogeneous deposition behavior in cold spray be understood, exploited, and further controlled to enable the fabrication and design of porous functional surfaces?

Based on the above research background, this thesis aims to investigate whether the inherent non-uniform deposition behavior in the cold spray process can be transformed from a traditionally perceived "deposition defect" into a usable structure formation mechanism, and further applied to the design and fabrication of porous functional surfaces. Unlike existing studies that mainly focus on improving deposition efficiency and obtaining dense coatings, this work emphasizes the structural formation characteristics and potential engineering value associated with deposition failure regions. In particular, it seeks to establish the intrinsic relationship between cold spray deposition behavior, porous structure formation, and functional performance.

To achieve these objectives, the thesis is organized around the following research tasks:

(1) investigating the formation mechanism of porous structures during the cold spraying of Ti64, with particular emphasis on the relationship between particle deposition behavior, deposition efficiency, and pore formation;

(2) using boiling heat transfer as a functional validation platform to systematically evaluate the heat transfer performance of cold-sprayed porous surfaces and analyze the corresponding enhancement mechanisms;

(3) based on the understanding of the above mechanisms, exploring methods for the controllable fabrication of porous structures through substrate surface pretreatment, thereby extending the material-driven pore formation mechanism into a geometry-driven pore design strategy; and

(4) establishing the relationship between cold spray deposition behavior, surface structural characteristics, and functional performance, in order to provide a theoretical basis for the design and engineering application of cold-sprayed porous functional surfaces.

Following the clarification of these research objectives, the subsequent chapters are developed progressively around these themes, constructing a comprehensive research framework from the perspectives of mechanism investigation, performance validation, and controllable fabrication.

To answer this question, the thesis first investigates the formation mechanisms of porous structures during the cold spraying of Ti-6Al-4V, elucidating the relationships among particle deposition behavior, deposition efficiency, and pore formation. Subsequently, pool boiling heat transfer is employed as a functional validation platform to systematically evaluate the heat transfer performance of the resulting porous structures and to clarify the underlying enhancement mechanisms. Finally, based on the mechanistic understanding established in the preceding studies, substrate surface pretreatment is introduced to extend the pore formation mechanism from a material-driven process to a geometry-driven process, thereby enabling the controllable fabrication of porous structures. Through these investigations, this thesis aims to establish the relationships between cold spray deposition behavior, porous structure formation, and functional performance, providing a theoretical foundation for the design and manufacture of porous functional surfaces using cold spray technology.

Based on this understanding, Chapter 2 of this thesis systematically investigates the formation mechanism of porous surfaces during the cold-spray deposition of Ti64. By analyzing initial deposition behavior, deposition efficiency, and coating microstructure, the intrinsic origins of porous surface formation in high-critical-velocity materials under cold-spray conditions are elucidated. The results indicate that the porous surface of Ti64 originates from spatially non-uniform particle bonding during the initial deposition stage, rather than from post-processing or the accumulation of random defects. This finding provides important insight into the fundamental nature of porous structures formed by cold spray.

Building upon this mechanistic understanding, Chapter 3 employs boiling heat transfer as an application platform to systematically evaluate the functional performance of cold-sprayed Ti64 porous surfaces. Boiling heat transfer is highly sensitive to surface microstructure, particularly in terms of bubble nucleation, growth, detachment, and critical heat flux (CHF). Porous structures are capable of strongly modulating interfacial interactions during these processes. Experimental results demonstrate that cold-sprayed Ti64 porous surfaces enable bubble nucleation at relatively low wall superheat and, under certain conditions, significantly enhance CHF. This performance enhancement is primarily attributed to an increased density of nucleation sites, enhanced capillary liquid replenishment, and suppression of lateral bubble coalescence introduced by the porous structure. Nevertheless, owing to the intrinsically low thermal conductivity of Ti64, the additional thermal resistance associated with increasing coating thickness becomes increasingly pronounced, ultimately limiting further heat-transfer enhancement. This observation highlights the importance of simultaneously considering structural functionality and intrinsic thermophysical properties in the design of porous surfaces.

While the cold-spray process of Ti64 naturally reveals the mechanism of porous formation, the resulting porous structures still exhibit a degree of spatial randomness, and material selection is constrained by intrinsic deposition characteristics. To achieve controllable porous design and material transferability, Chapter 4 proposes a conceptual transition from "material-driven porosity" to "geometry-driven porosity" based on the preceding mechanistic insights. By pre-treating aluminum substrates to introduce artificial geometric defect regions on the surface, areas that are intentionally unfavorable for effective deposition are created. These predefined regions are functionally equivalent to the naturally occurring deposition-failure zones during the initial cold-spray deposition of Ti64, thereby enabling the replication and regulation of porous surface formation even in material systems with high deposition efficiency. Experimental results confirm the effectiveness of this strategy in aluminum-based systems, demonstrating that the mechanism of porous structure formation in cold spray possesses good generality and design flexibility.

In summary, this thesis addresses the core scientific issues associated with the fabrication of porous surfaces by cold spray, systematically investigating formation mechanisms, structural characteristics, and functional performance in boiling heat transfer. By identifying selective deposition during the initial deposition stage as a key mechanism in Ti64 and extending this concept to a geometry-controlled design strategy, this work not only deepens the understanding of cold-spray deposition behavior but also provides new perspectives for the designable manufacturing of porous functional surfaces. In this study, boiling heat transfer serves as a highly sensitive and quantitatively assessable application platform to validate the functional effectiveness of porous structures, rather than as the ultimate research objective.

The organization of this thesis is as follows. Chapter 2 systematically reviews research progress related to porous structures produced by cold spray, with emphasis on deposition non-uniformity and pore-formation mechanisms. Chapter 3 focuses on the microstructural characteristics and boiling heat-transfer performance of cold-sprayed Ti64 porous surfaces. Chapter 4 extends the identified mechanisms to aluminum-based systems, achieving controllable porous construction through substrate pre-treatment. Finally, the main conclusions are summarized, and future prospects for cold-sprayed porous functional surfaces in engineering applications are discussed.

Chapter 2 Literature review

2.1 Cold spray technology

2.1.1 Metal additive manufacturing technology

Additive manufacturing technology, also known as rapid prototyping technology, commonly known as 3D printing, since the development of the 1980s, the development is very rapid[1][2][3][4][5][6]. The technology is a process for manufacturing metal parts by stacking materials layer by layer, using digital technical files as a guide[7][8]. To be more specific, the technology is based on the principle of 'discrete stacking', where a three-dimensional model is first created on a computer using drafting software such as AutoCAD. The 3D model is then layered down to a 2D planar model using slicing software. Finally, additive manufacturing equipment is used to carry out point-by-point or layer-by-layer deposition to form the final three-dimensional solid parts[9][10][11].

Among the additive manufacturing technologies, metal additive manufacturing is the most promising technology with a wide range of applications. The technology can be used for prototyping in aerospace research. Boeing had used this technology to make F-15 pylons[12]. Apart from this, it can also be used in defense business, automotive industry, biomedical and other fields[3][13][14][15]. Compared to traditional manufacturing methods (e.g. casting, welding), metal additive manufacturing offers the possibility of preparing workpieces with complex geometries[16][17][18][19]. Rapid prototyping, printing of large components, reduction of printing defects and enhancement of mechanical properties are the key factors driving the development of metal additive manufacturing technology. A variety of metal additive manufacturing technologies have been developed to meet the demand for high-resolution printing of complex structures.[20]

Metal Additive Manufacturing technology in the narrow sense is mainly a process in which powdered raw materials or metal wires are completely melted by the energy input of laser or electron beams and transformed layer by layer into workpieces of arbitrary geometrical shapes. Common metal additive manufacturing technologies can be categorized in terms of the nature of the feedstock, the state of aggregation, and the bonding mechanism between the material layers[21]. The most used additive manufacturing processes laser beam melting (LBM), electron beam melting (EBM), and laser metal deposition (LMD). The LBM process is also known as selective laser melting (SLM), direct metal laser sintering (DMLS), laser metal fusion (LMF), or industrial 3D printing[22][23][24]. The LMD process is also known as direct metal deposition (DMD), laser engineered net shaping (LENS), laser cladding, or laser deposition welding[25][26][27].

Broad additive manufacturing technologies include adhesive jet molding techniques that have emerged in recent years, cold spraying, stir friction welding, direct metal writing and related diode-based processes[28][29][30].

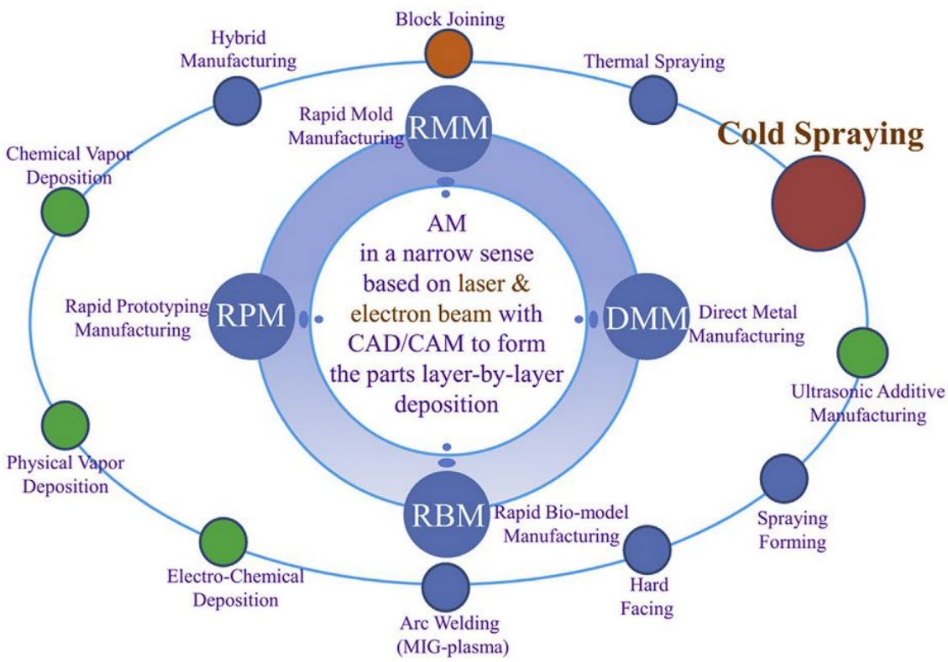

Figure. 1 Additive manufacturing(AM) in a broad sense (the inner parts show the AM processes in a narrow sense)[31]

2.1.2 Overview of cold spray

As an emerging additive manufacturing technology, cold aerodynamic spraying (Cold Spraying) has a wide range of applications in the field of materials processing. Cold spraying is a powder deposition method that uses the self-solidifying ability of solid powder particles to combine with each other, and the self-solidification of this powder can only be realized under the condition of high-speed impact[28][29][32].

The concept of cold spraying corresponds to the concept of thermal spraying, where ‘cold’ or ‘hot’ is not defined in terms of an absolute temperature, but rather in relation to the melting point of the material[33]. In thermal spraying, the temperature of the flame stream generally exceeds the melting point of the material, and the powder particles are softened or melted in the flame stream and deposited in a molten or semi-molten state. In the cold spraying process, the temperature is much lower than the melting point of the material, and the raw material powder does not melt and is deposited in a completely solid state. It is the low temperature and non-melting properties that make cold spraying avoid the oxidation, phase change, diffusion and thermal stress problems commonly associated with thermal spraying, making it a unique prospect for industrial applications[34][35][36][37].

This technique was originally developed by Thurston in the early twentieth century[38]. Later researchers used blast or pressurised gas to accelerate metal powders to a maximum of 300m/s and then hit the substrate to form layers. By the 1950s, Rocheville[38][39] had made important innovations to the technique. In his design, a bi-directional particle-gas flow through a Delaware nozzle allowed the particles to achieve higher velocities and form a uniform coating on the substrate. In the 1980s, Alkhimov and others at the Institute of Theoretical and Applied Mechanics of the Russian Academy of Sciences found that when the velocity of metal particles exceeded a certain critical value, the effect of particles on the substrate changed from erosion to adhesion, and carried out in-depth research on it, and their findings contributed to the advancement of the modern cold spraying device and cold spraying technology. Since the introduction of Alkhimov's cold spraying equipment, a large number of patents and publications have appeared every year related to the cold spraying process and applications, and the research directions involved have expanded from fluid mechanics to solid mechanics, etc., which has ultimately led to the development of cold spraying as a manufacturing technology with a wide range of applications in the fields of aerospace, automotive, energy, medical, and oceanographic applications[40][41].

2.1.3 Principle and characteristics of cold spray

Cold spray technology is a new solid-state coating preparation technology based on supersonic gas-solid two-phase flow and high-speed collision dynamics, Fig .2 is a schematic diagram of the cold spray system. Compressed gas (nitrogen, helium, air or gas mixture, etc.) as an accelerating medium, driving metal particles in the solid state at very high-speed collision substrate, so that the particles undergo strong plastic deformation and deposition of the coating[42] [43].

From a gas-dynamic perspective, the cold spray process can be described as a compressible supersonic gas flow coupled with particle acceleration. Rab et al.[44] developed a three-dimensional multicomponent CFD model for the cold spray process using nitrogen and air, in which the gas flow was considered as a steady-state supersonic turbulent flow with heat transfer. In their model, the selected CFD program solved the Navier–Stokes equations for compressible flow, and the governing equations included the continuity equation, momentum equation and total energy equation.

The continuity equation for the gas phase can be expressed as:

$$\frac{\partial \rho}{\partial t} + \frac{\partial}{\partial x_j}\left(\rho U_j\right) = 0 \tag{2.1.3.1}$$

where ρ is the density of the fluid, U_j is the velocity component of the fluid and t is time. x_i denote the Cartesian spatial coordinates.

For the compressible turbulent gas flow in cold spray, the momentum equation can be written as:

$$\frac{\partial \rho U_i}{\partial t} + \frac{\partial}{\partial x_j}\left(\rho U_i U_j\right) = -\frac{\partial p'}{\partial x_i} + \frac{\partial}{\partial x_j}\left[\mu_{eff}\left(\frac{\partial U_i}{\partial x_j} + \frac{\partial U_j}{\partial x_i}\right)\right] + S_M \tag{2.1.3.2}$$

where p' is the modified pressure, μ_{eff} is the effective viscosity responsible for turbulence, and S_M is the sum of body forces. U_i and U_j are the velocity components in the $i-$ and $j-$ directions, respectively. x_j denote the Cartesian spatial coordinates.

The total energy equation, expressed in terms of total enthalpy, is given as:

$$\frac{\partial(\rho h_{tot})}{\partial t} - \frac{\partial p}{\partial t} + \frac{\partial}{\partial x_j}\left(\rho U_j h_{tot}\right) = \frac{\partial}{\partial x_j}\left(\lambda \frac{\partial T}{\partial x_j} + \frac{\mu_t}{Pr_t}\frac{\partial h}{\partial x_j}\right) + \frac{\partial}{\partial x_j}\left[U_i\left(\tau_{ij} - \rho\overline{u_i u_j}\right)\right] + S_E \tag{2.1.3.3}$$

where htot is the total enthalpy, λ is the thermal conductivity, T is the temperature, μt is the turbulent viscosity, Prt is the turbulent Prandtl number, h is the static enthalpy, τij is the stress tensor and SE is the energy source term.

The total enthalpy is further defined as:

$$h_{tot} = h_{stat} + \frac{1}{2}(U_i \times U_i) + k \qquad (2.1.3.4)$$

where hstat is the static enthalpy and k is the turbulent kinetic energy.

The total temperature of the inlet gas can be described as:

$$T_{tot} = T_{stat} + \frac{U^2}{2c_p} \qquad (2.1.3.5)$$

where Ttot is the total temperature, Tstat is the static temperature, U is the velocity and cp is the specific heat at constant pressure.

Several dimensionless quantities are also relevant to the description of cold spray gas dynamics. Rab et al. listed the local Mach number and Reynolds number as important parameters in the cold spray CFD model. The Mach number describes the ratio between the local gas velocity and the local speed of sound, and is used to characterise whether the gas flow is subsonic, sonic or supersonic. This is particularly important in cold spray because particle acceleration is achieved by a supersonic jet generated through a converging–diverging De Laval nozzle. The Reynolds number describes the relative importance of inertial and viscous effects in the gas flow. In the context of gas–particle interaction, the particle Reynolds number is also commonly used to characterise the flow around an individual moving particle and is closely related to the drag behaviour. These dimensionless quantities help to describe the gas flow regime, particle acceleration environment and subsequent impact conditions during cold spray deposition.

In the cold spraying process, the particle size of a certain case, only in a certain speed range to collide with the substrate to form an effective deposition (Fig.3), the lower limit of the speed is called the critical speed[43] [45] [46], the upper limit is called the erosion speed. When the particle velocity is below the critical velocity, the particle will rebound when it collides with the substrate. Conversely, when the particle velocity is higher than the erosion velocity, the particles will erode against the substrate and detach from it.

Therefore, the critical velocity is a very important parameter in the cold spraying process, and the factors affecting the critical velocity will be discussed later[47][48][49][50][51].

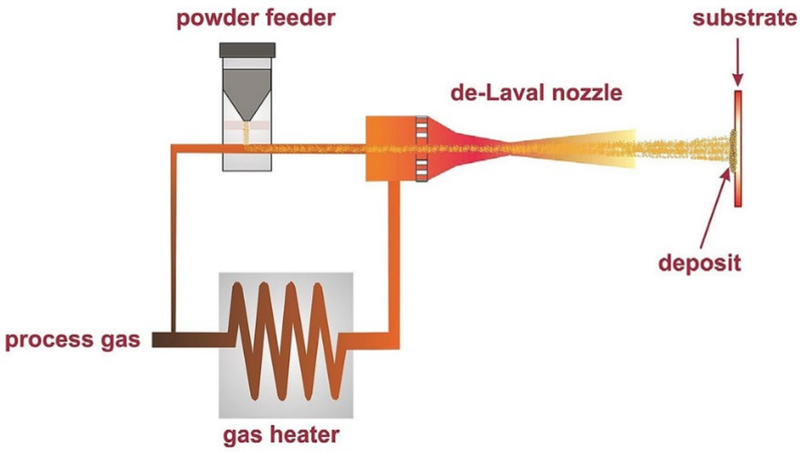

Figure. 2 Schematics of the main components of CS system[52]

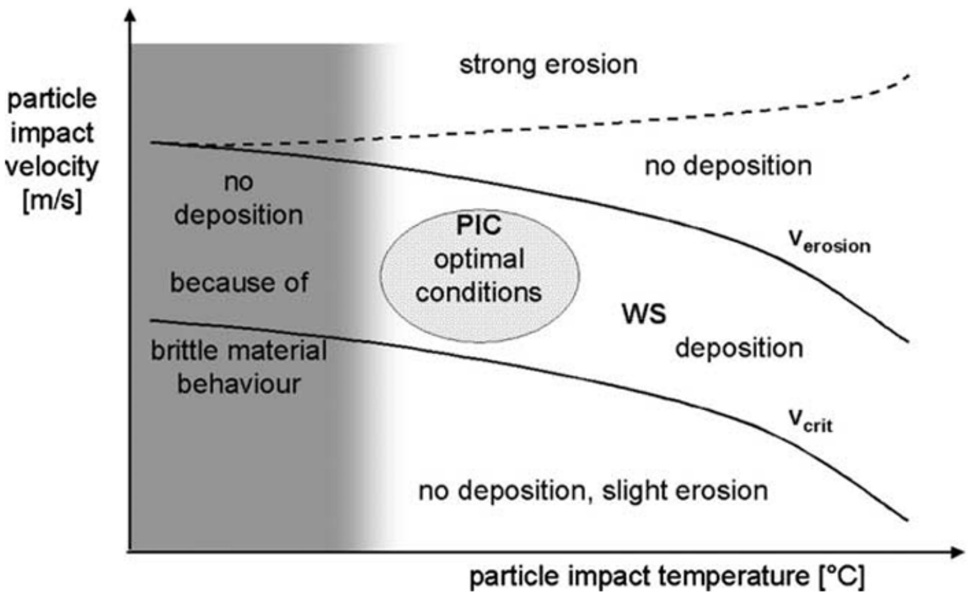

Figure. 3 Particle velocity over particle temperature with window of sprayability (WS) and the regime of particle impact conditions (PIC)[43].

Cold spraying technology is characterized by high particle velocity and low temperature, therefore, compared with traditional thermal spraying, cold spraying technology has the following advantages[52][53][54][55]:

(1) The oxidation, phase change, decomposition and grain growth of the powder can

be effectively avoided or reduced, so that the chemical composition and microstructure of the coating can be consistent with the original powder;

(2) Dense coating, low porosity, densities up to 98% or more, to ensure that the coating of good thermal and electrical conductivity;

(3) Small thermal influence on the substrate;

(4) The residual stress of the coating is relatively low, and for the compressive stress, reducing the limitations on the thickness of the coating;

5) No pollution, and simple and safe operation.

In view of the above advantages, cold spraying technology is now widely used in the preparation of protective coatings and functional coatings, and in the aerospace, automotive, shipbuilding, electrical engineering and instrumentation manufacturing industries. Fig.4 shows a typical comparison of the thickness of coatings prepared by traditional surface engineering techniques and cold spraying techniques [10], from which it can be seen that cold spraying has the advantage that the thickness of the coating is basically unlimited, and therefore cold spraying has also been applied to repair and additive manufacturing and other fields.

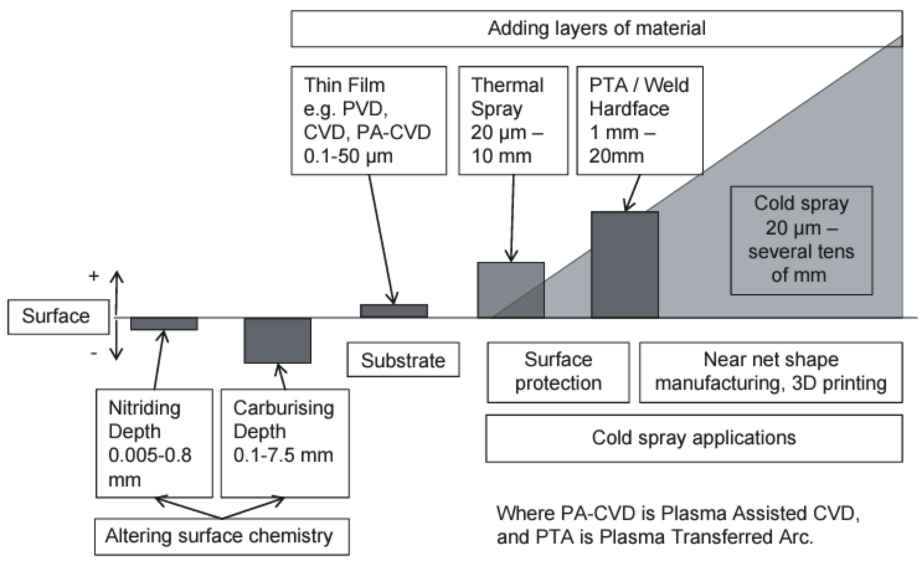

Figure. 4 Cold spray in the surface engineering space. CS cold spray, PVD physical vapor deposition, CVD chemical vapor deposition[39]

2.1.4 Deposition behaviour and bonding mechanism during impact of cold spray

Van Steenkiste et al. summarised the formation process of a cold sprayed deposited layer into four stages, as shown in Fig. 5:

(1) deformation of the particles and the substrate after impact, forming the first deposited layer;

(2) deformation and reorganisation between the particles as loading continues;

(3) metallurgical bonding between the particles is achieved, with a reduction in the porosity of the deposited layer;

(4) further densification of the coating.

Overall, the formation and growth of the deposited layer in cold spraying can be divided into two steps, firstly, the combination of particles and substrate, and secondly, the combination between particles[56].

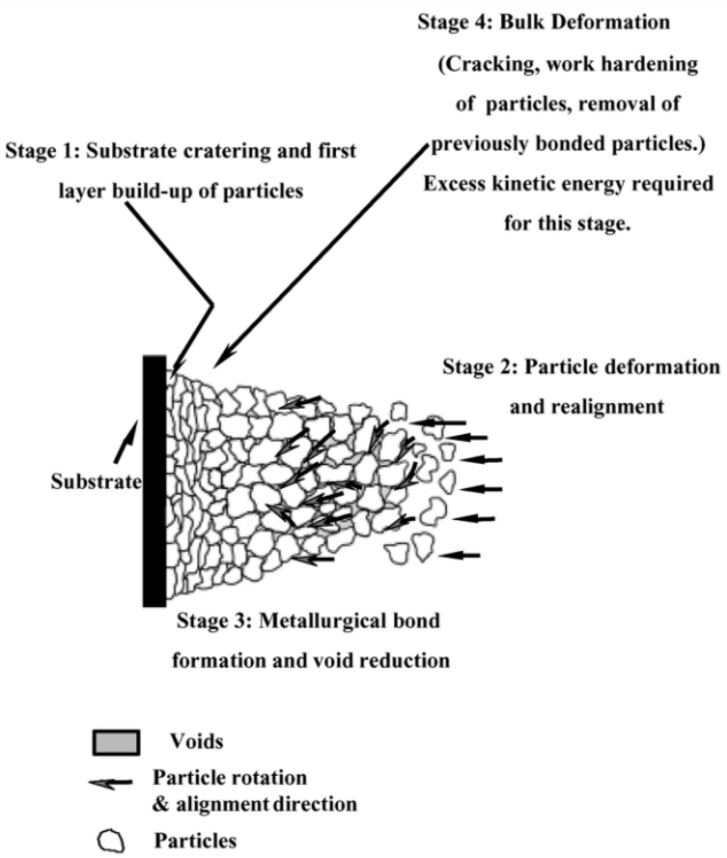

Figure. 5 Stages of coating formation in the cold spray process[56]

A number of researchers have made studies on the deposition behaviour of single particles in cold spraying by means of numerical simulations and experimental studies[57] [58][59] [60][61] [62] [63]. Fig. 6 show the classical numerical simulation results when Cu particles collide. It is not difficult to find that, in the cold spraying process, when the particles are accelerated to a higher speed and hit the substrate, they will show two typical characteristics: (1) the inhomogeneity of particle deformation. While the particle undergoes strong plastic deformation, the deformation is mainly concentrated at the 'particle/substrate' interface, and the amount of plastic deformation near the interface is as high as 10, while the amount of strain in the upper part of the particle is lower than 0.5. In addition, the collision bonding time of the particles is very short, which is only 10-50ns, and thus results in the plastic deformation rate as high as 10^9/percent in the vicinity of the cross-section. Kim[63] et al. found large strain bands at the interface of cold sprayed aluminium particles(Fig. 7); (2) the heat generated by the plastic deformation of the solid particles in a short period of time meets the condition of adiabatic pre-shear instability during the deformation time, and produces a rapid heating and cooling at the 'particle/substrate' interface, with a heating rate of up to 10^{10}K/s, and the cooling rate is also as high as 10^9K/s. Due to the coupling of extreme conditions such as high strain, high strain rate, adiabatic warming, and rapid cooling, amorphous regions are generated at the interface, and when the interface temperature is higher than the recrystallisation temperature corresponding to the degree of deformation of the material, the metal at the interface of the particles undergoes recrystallisation. Xiong et al[64]. found both recrystallisation and amorphisation at the interface of cold sprayed aluminium particles. For some low melting point metals or under extreme spraying conditions, the peak temperature at the particle interface can exceed the melting point of the material and melting and re-solidification can occur (Fig. 8.)[65].

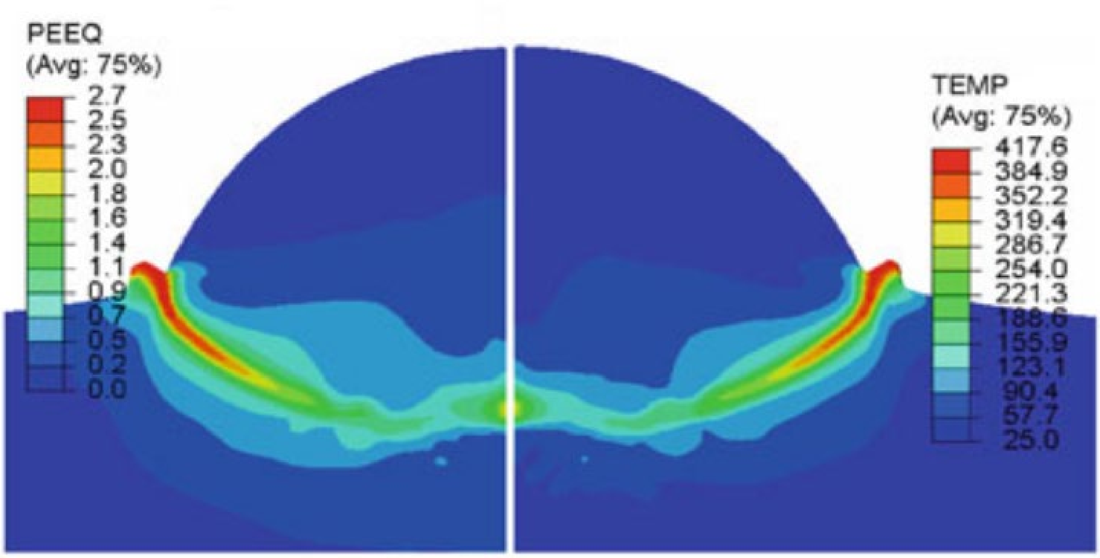

Figure. 6 Evolutions of equivalent plastic strain (PEEQ, left side) and temperature (TEMP , right side) of a 40μm Cu particle impacting upon a Cu substrate at the impacting velocity of 310m/s[57]

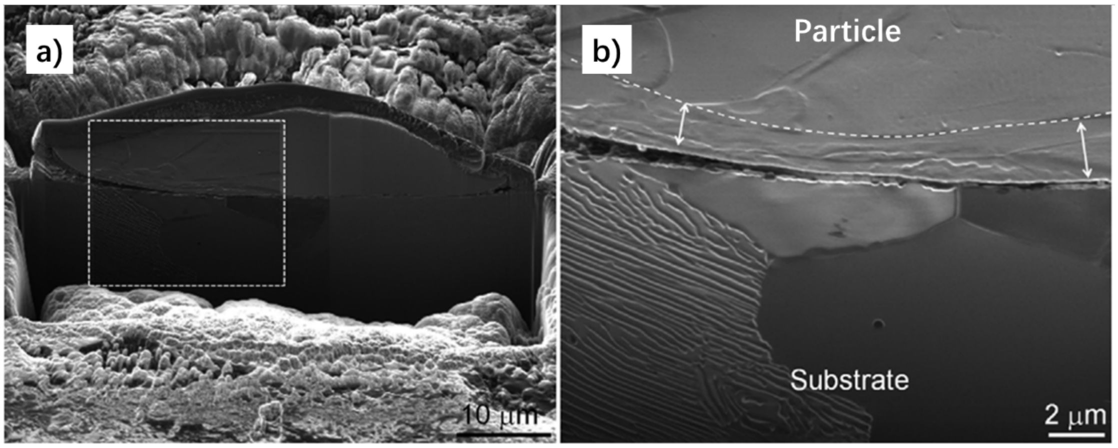

Figure. 7 CS-ed Al particle on steel substrate: a) cross-sectional images after 180º rotation and milling; b) magnified image at the marked region in (a)[63]

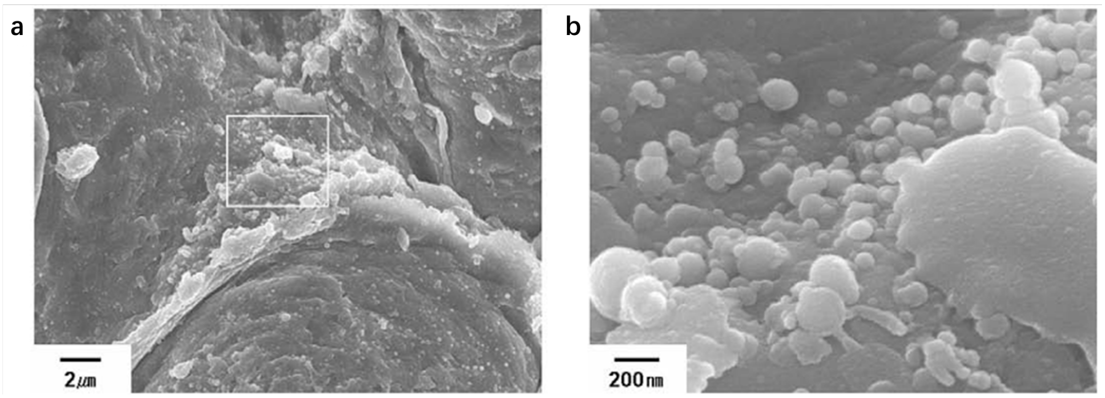

Figure. 8 Melting in CS: a) Ti particle successfully deposited onto a previously deposited layer; b) local melting under higher magnification of the boxed areas in (a)[65]

In order to obtain the desired coatings by using cold spraying, it is important for researchers to investigate the bonding mechanisms during cold spraying, i.e., how the particles bind to the substrate and how the coatings are formed. Although cold spraying has been studied for close to 30 years, the bonding mechanisms between solid particles and substrates or solid particles are not fully understood. Based on the observation of the coating microstructure by scanning electron microscopy and projection electron microscopy, as well as the assistance of other equipment, several reliable models have been proposed to explain the binding of particles during cold spraying. These explanatory models mainly include adiabatic shear instability[66] [67][68], oxide rupture[65], local melting[62] [69][70], diffusion[71], interfacial amorphization[72] and mechanical locking[73]. In addition, these mechanisms do not exist independently of each other, and one or more binding mechanisms may exist simultaneously during the deposition process, which act together to lead to the formation of the final coating.

2.1.4.1 Adiabatic shear instability:

Adiabatic shear instability is the main mechanism for the binding of solid particles during cold spraying[43] [66][65] [67][68] [71] [74]. The high strain rate adiabatic deformation occurring in the local interfacial region will inevitably cause warming, which is also important for the bonding of the particles to the substrate. Asssadi[67] et al. investigated the adiabatic shear instability during cold spraying by studying the deposition behaviour of copper particles impacting on copper substrates by means of finite element simulations.

This study showed that when the particle velocity was increased from 550 m/s to 580 m/s, the plastic deformation, temperature and flow stresses on the substrate and particle impact surfaces were altered, and these alterations indicated the occurrence of adiabatic shear instability. In addition, M Grujicic et al[68]. showed that the formation of jets is also due to adiabatic shear instability due to local plastic strain and softening effects, as shown in Fig. 9.

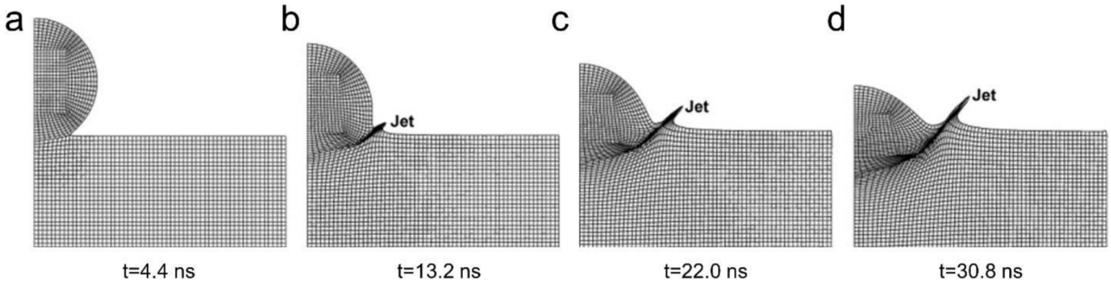

Figure. 9 The time evolution of particle and the substrate shapes during impact of a 25-μm Cu particle onto the Cu substrate at 550 m/s: a) 4.4 ns; b) 13.2 ns; c) 22.0 ns and d) 30.8 ns[68]

The results of the present study indicate that the occurrence of adiabatic shear instability in materials plays an important role in the binding of particles, and the main types of binding that may result from this are as follows:

(1) Mechanical bonding.

The material undergoes adiabatic shear instability and produces plastic flow under pressure, which contributes to intermixing and mechanical interlocking between the substrates and particles, resulting in mechanical bonding. Grujiciic et al. suggest that mechanical occlusion at the nano- and micrometre scales is the main mechanism, and that instability at the interface will give rise to the Kelvin-Helm-holtz phenomenon, that is, when two fluids are picked up and have different velocities, roll-ups and vortices are created[62][75][76].

(2) Metallurgical bonding

Computer simulations have shown that the onset of adiabatic shear instability can lead to localised temperatures at the particle/substrate contact surface reaching the melting point, resulting in metallurgical bonding at the interface. This bonding occurs mainly in low melting point materials, such as zinc, and is unlikely to occur in high melting point materials[62][77][78].

(3) Physical bonding

The jet produced by adiabatic shear instability removes the oxide film from the surface of the particles and the substrate, creating a clean surface and forming a physical bond at higher pressures, i.e., Van der Waals forces, and is more favorable to bonding when both the particles and the substrate are capable of generating heat flow[68].

As mentioned earlier, under different material and process parameters, one or more of the above three bonding modes may be present in the coating, but one of them plays a dominant role. Also, the region where adiabatic shear instability occurs is limited to localised interfaces[79][80][81].

2.1.4.2 Stress wave induced material jet formation mechanism

Adiabatic shear instability during particle bonding is mainly based on simulation results from finite element analysis, but this theory has not been sufficiently confirmed experimentally. It is extremely important to understand how the particles bond together during the cold spraying process as they impact the substrate at high speeds. By using a high-speed camera and simultaneous quasi-continuous laser imaging, Hassani[82] et al. have observed in detail the impact of individual particles at supersonic speeds and concluded that bonding between particles occurs through the formation of material jets induced by stress waves. This type of in situ observation provides higher spatial and temporal resolution to the micron and nanosecond level. As exemplified in Fig. 10, when particles impact below a certain threshold velocity, they bounce off the substrate; and once the velocity exceeds this threshold, adhesion with the substrate occurs and a jet of material is observed in the direction of shear deformation, as indicated by the white arrow in the figure. Furthermore, numerical simulations show that when the pressure at the impact surface reaches a critical value, jets are formed at the edge of the interface. Therefore, this material ejection triggered by high stress waves is regarded as a key mechanism for interparticle bonding.

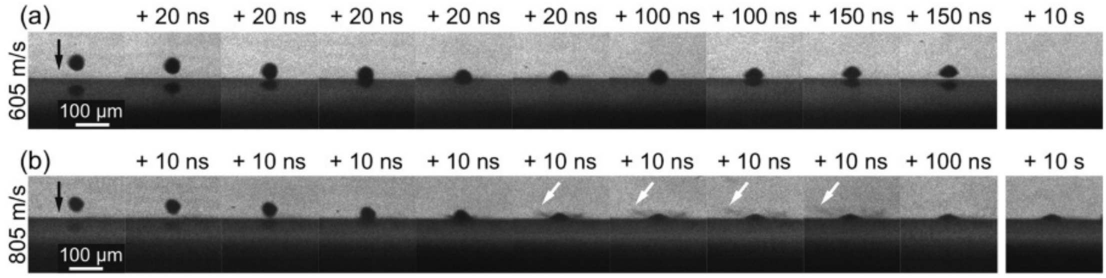

Figure. 10 In-situ observation of the bonding moment in microparticle impact. Multi-frame sequences with 5 ns exposure times showing 45-µmAl particle impacts on Al substrate at 605 m/s (top) and 805 m/s (bottom), respectively below and above critical velocity. Material jetting is indicated with white arrows[82].

2.1.4.3 Oxide layer break up mechanism

When discussing the bonding process in cold spraying, there is a view that the bonding is mainly due to the break up of the oxide layer during the impact process (see Fig.11)[58][83]. Normally, the surfaces of both the particles and the substrate are covered by a natural oxide film (as shown in Fig. 11-a). When the particles impact the substrate at supersonic speeds, a strong plastic deformation occurs at the point of impact, causing the brittle, hard oxide film to rupture (as illustrated in Fig. 11-b). This process exposes fresh metal surfaces, which are tightly bonded to each other under high pressure, facilitating effective metallurgical bonding (see Fig. 11-c). However, residual oxides at the interface between the particles may prevent complete bonding of the particles, especially in the central region of the interface (as illustrated in Fig. 11-d). By increasing the processing parameters, it is possible to obtain higher impact velocities for the cold sprayed particles, which triggers more intense plastic deformation and breaks up the oxide layer into finer fragments so that the metallurgical bonding can be further strengthened due to the increased contact area. For particles with thicker oxide films, the breakdown of the oxide layer requires more kinetic energy, which leads to higher critical velocities. Therefore, the selection of powders with low or no oxygen content as feedstock is particularly critical in the preparation of high-performance cold spray layers or deposits.

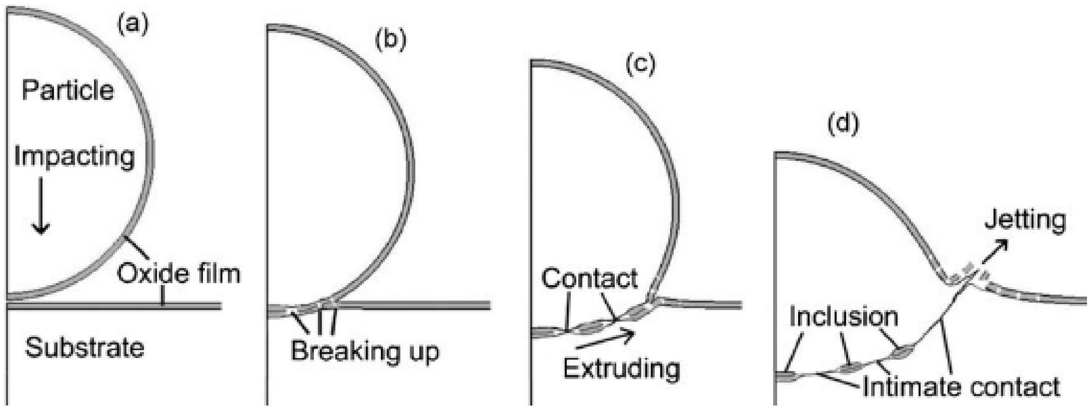

Figure. 11 Schematic diagram of particle impacting and bonding processes in cold spraying.[58]

2.1.5 Influential factors for cold spray

2.1.5.1 Nozzles

The nozzle is a key component of the cold spray system and it affects cold spraying in two main ways. One is the intrinsic parameters of the nozzle, and the other is the nozzle's trajectory during the cold spraying process.

The nozzle is generally composed of a converging interface and a dispersing interface (Fig. 12). The inherent parameters of the nozzle are mainly, respectively, including inlet diameter/area, throat diameter/area, outlet diameter/area, convergence length and divergence length. Researchers have found that the ratio of cross-sectional throat area to outlet area (expansion ratio) and divergence length are two important parameters for accelerating powder particles. Wenya Li et al. using stainless steel particles have found that the expansion ratio is affected by the gas conditions, and the particle size. Combining these influences, the optimum expansion ratio for cold sprayed stainless-steel particles is 1-10[84].

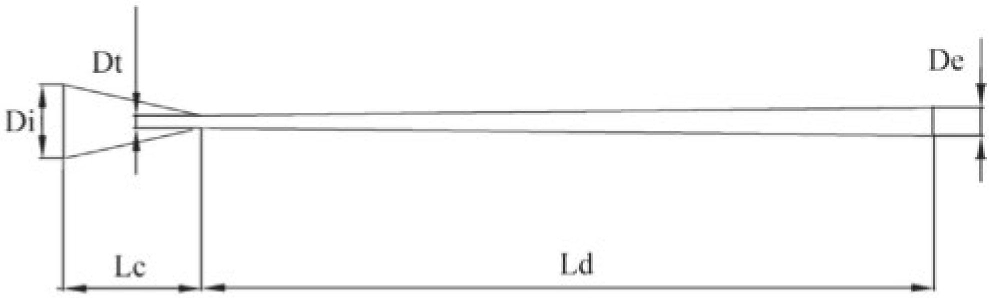

Figure. 12 Schematic dimensions of cold spray nozzle geometry[5]

In addition, the nozzle outlet diameter determines the size of the spray point and thus the manufacturing accuracy. By using a nozzle with a large throat diameter and a large outlet diameter, the machining of large parts can be accomplished, and a high work efficiency can be ensured. In this case, a single spray pass can produce a spot area with a diameter of more than 10 mm. In contrast, if the structure of the while machine to be processed is more delicate, it is necessary to design nozzles with small outlet diameters. For example, Sova et al[85] designed a supersonic micro-nozzle with an exit diameter of about 1 mm, which produces a single-pass trajectory width of about 1 mm, as shown in Fig. 13.

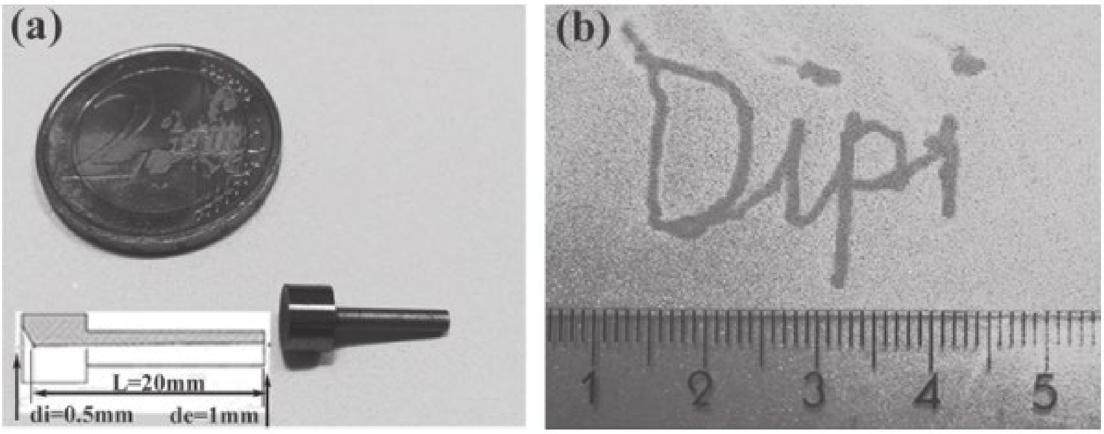

Figure. 13 a) A small supersonic nozzle , b) a copper deposit on aluminum substrate cold sprayed by it[85]

In the process of cold spraying, there are several variable parameters of the nozzle that also affect the results of cold spraying. Three of these parameters are the most important, they are spraying distance, spraying angle and travelling speed.

Spraying distance refers to the distance from the nozzle to the substrate. The effect of spraying distance on the quality of cold spraying is mainly achieved by influencing the velocity of particles hitting the substrate. Pattison et al [86] graphically demonstrated the effect of standoff distance on DE (Fig. 14). The standoff distance was divided into three characteristic zones:(1) smaller, where the DE increases with increasing standoff distance; (2) medium, where the DE remains stable; and (3) larger, where the DE begins to decrease with increasing distance. To obtain high DE, the isolation distance should be set in the intermediate region[86] [87].

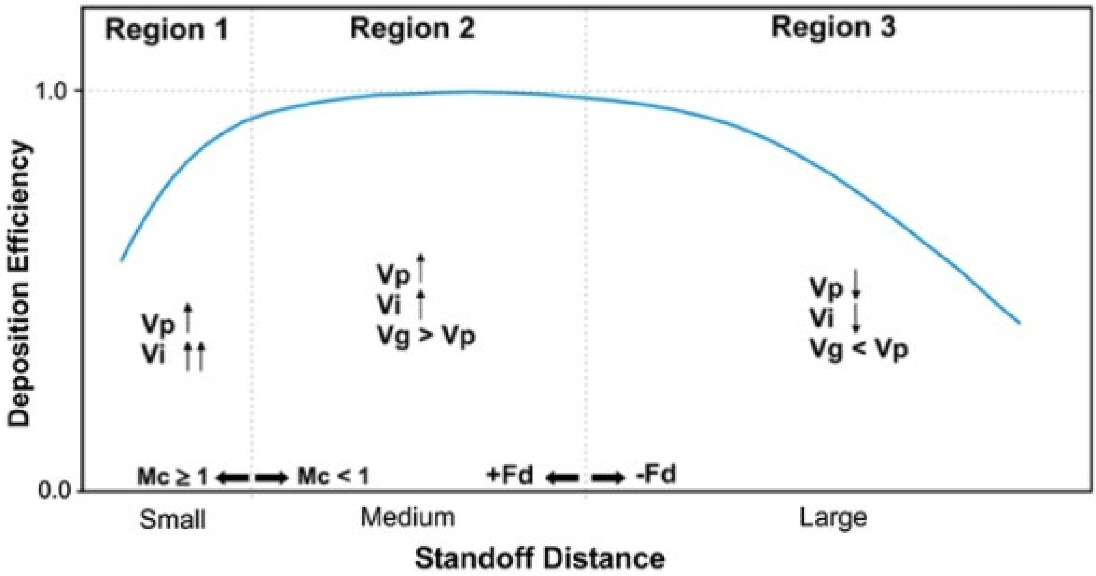

Figure. 14 Non-dimensional chart showing the effect of standoff distance on deposition efficiency. Note that Fd is the drag force, Mc is the centerline Mach number, Vg is the gas velocity, Vi is the particle impact velocity and Vp is the in-flight particle velocity[86]

The spraying angle is the angle between the nozzle and the substrate, and the spraying angle of the nozzle with respect to the substrate surface can be varied between 90° and 30°, as shown in Fig. 15[88].Yin et al.[89] found that the post attachment of the deposited layer increases with the increase of the spraying angle by means of finite element simulation plus experimental methods. However, the trend of porosity is opposite to the deposited thickness, i.e., the porosity decreases with the increase of the spraying angle.

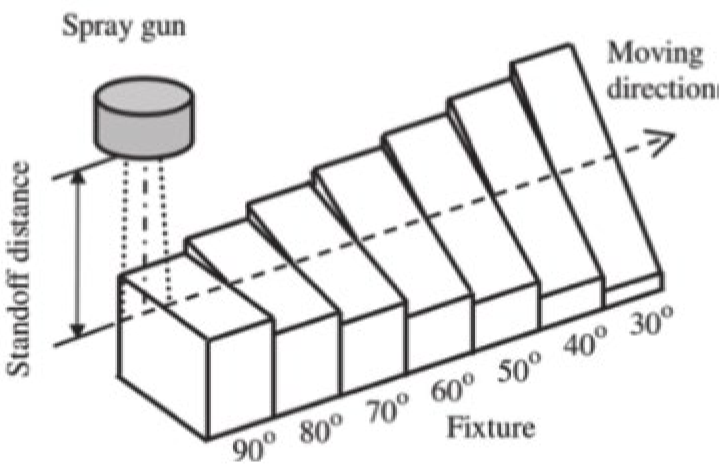

Figure. 15 Setup of different spray angles in one spray run[88]

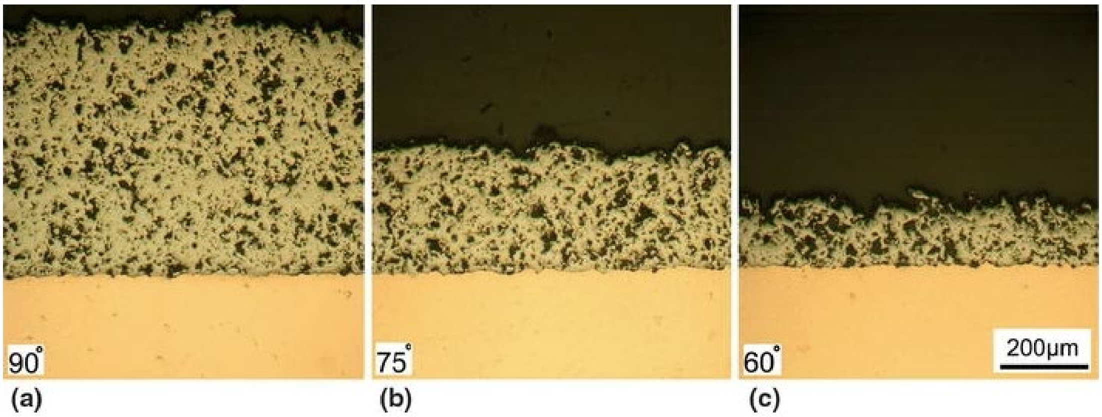

Figure. 16 Cross-sectional OM micrographs of the Ti coating deposited on the Cu substrate at different spray angles[89]

The last important parameter related to the nozzle is the transfer speed of the nozzle. Transfer speed affects the porosity, the deposited thickness, and the substrate temperature. In their study, Wong et al.[90] conducted cold spraying experiments of terylene powder using two different nozzle travelling speeds (150 mm/s and 5 mm/s). The results showed that the nozzle travelling speed and the porosity of the deposited body were positively correlated, with the porosity of the resulting components being 0.9% and 0.1%, respectively. The reason for such a significant difference is that the nozzle velocity decreases and the jet stays on the substrate for a longer period of time, which has a heating effect on the substrate and increases the deposition efficiency. A similar phenomenon has been reported by Choudhuri[91] and Tan et al.[92] in their respective studies.

2.1.5.2 Gas

Carrier gas is a medium used to feed cold spray powder into the active stream of the nozzle. The characteristics of the carrier gas and its conditions are critical to the particle movement and deposition process. Shuo et al.[93][94] used numerical simulations and experiments to investigate how the carrier gas temperature affects the particle acceleration and deposition during the cold spraying process. The results show that the temperature of the carrier gas significantly affects the supersonic flow and the particle acceleration induced by it. Previous studies have shown that increasing the carrier gas temperature enhances the acceleration of particles within the supersonic flow, resulting in higher particle impact velocities and improved deposition conditions during cold spray. N.W. Khun et al.[95][96] meticulously explored the anti-wear and anti-corrosion properties of cold-sprayed Ti64 coatings on industrial-grade Ti64 substrates using nitrogen (N2) and helium (He) as the carrying gases. When helium was used as the working gas, the Ti64 coatings obtained exhibited a denser microstructure and lower porosity. As a result, the hardness of the Ti64 coatings deposited with helium exceeded that of the corresponding coatings deposited with nitrogen. In addition, the helium-deposited Ti64 coatings exhibited higher adhesion.

2.1.5.3 Particle Condition

The particle state affects cold spraying in two main ways, particle size and particle morphology. When all other spraying parameters are the same, the larger particle size, the more difficult to accelerate and therefore the lower the kinetic energy gained by the particle. However, larger particles are more likely to achieve higher temperatures and thus lower critical velocities. The effect of particle size on particle impact velocity and critical velocity is given in Fig. 17 [43]. Interestingly, there exists an optimum particle size range where the particle velocity is much higher than its critical velocity. Particles with optimum particle size range give high quality coatings[97].

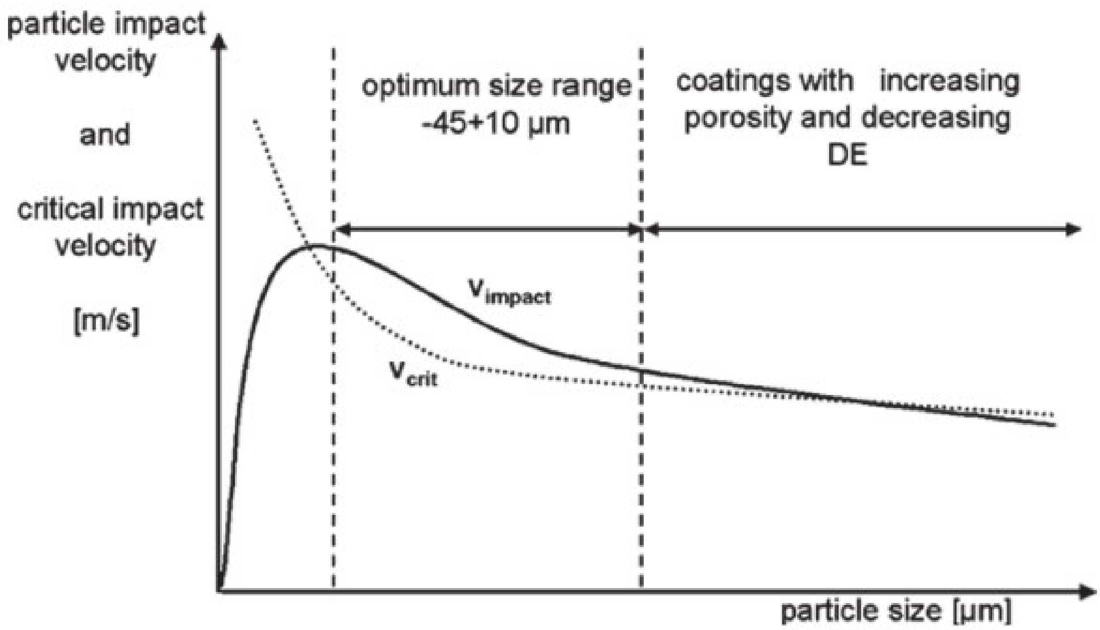

Figure. 17 The relationship between particle impact velocity and critical velocity and particle size distribution in cold spray[43]

The particles used for cold spraying can be classified as spherical and irregular shaped powders[98] [99]. For the same process parameters, irregular powders have a higher drag coefficient, which results in poorer fluidity and unfavourable deposition. Bhattiprolu's experiments with spherical and irregular shaped particles showed that irregular particles produced deposited components with higher porosity and lower microhardness.

2.1.5.4 Substrate condition

The temperature of the substrate and the surface roughness of the substrate can have a significant effect on the deposition results.

The deposition behavior of particles is different when the roughness of the metal surface is different, for example, a rougher surface has a larger contact area for high-speed particles to mechanically lock with. The effect of substrate surface roughness on the deposition behavior has been investigated using a combination of finite element simulation and experimental methods by S. Kumar et al.[100] It was shown that deposition is more likely to occur when the size of the substrate surface valleys is smaller than the particle size. In addition, a rougher surface increases the interfacial temperature during particle impact due to the higher friction provided, which increases the adhesion.

The temperature of the substrate affects the critical velocity of the particles, which in turn affects the deposition. When the substrate possesses a higher temperature, it significantly reduces the critical velocity of the particles. The study by M. Fukumoto et al.[101] shows confirmation of the above. It is very clear that even when the particles are deposited at room temperature, the Cu particles are still well deposited on the substrate when the substrate has a higher temperature.

2.2 Porous structures in additively manufactured materials

2.2.1 Classification of porosity

2.2.1.1 Microporosity

In additively manufactured materials, microporosity, which typically refers to pores ranging from a few to several tens of micrometers in size, is almost universally present across different processing mechanisms and material systems[102][103]. Unlike macroscopic lack-of-fusion defects or large voids caused by process instability, microporosity is not simply the direct result of a single mismatched process parameter. Instead, it arises from the coupled interactions among energy input mode, material flow behavior, and local densification kinetics. In recent years, related studies have gradually redefined microporosity, not merely as a "process defect," but as a key structural feature that provides crucial insight into the formation and evolution mechanisms of microstructures in additive manufacturing[104][105][106].

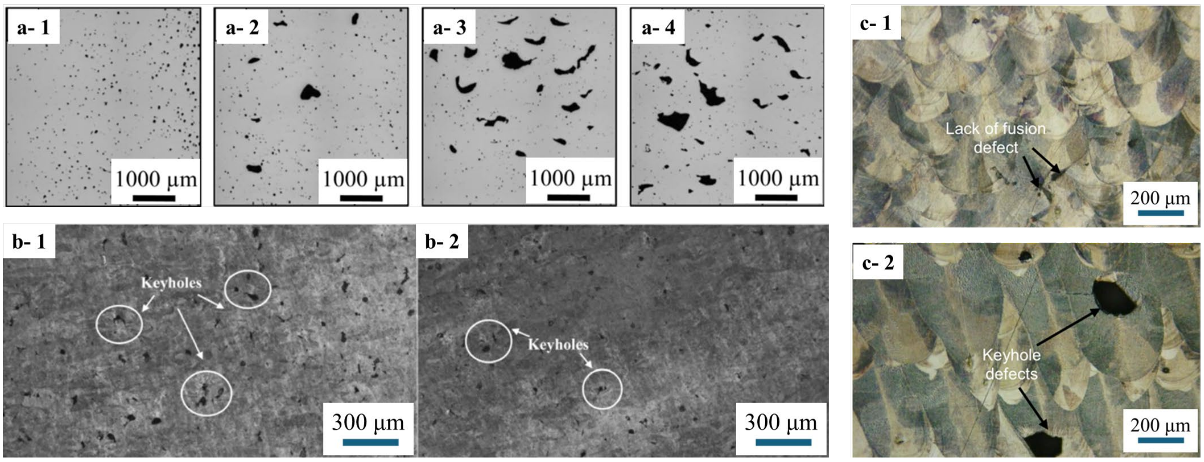

Figure. 18 Microporosity in different additive manufacturing processes[107][108][109]

In fusion-based additive manufacturing, particularly in selective laser melting (SLM/LPBF), numerous studies have revealed that the formation of microporosity is closely related to the transient geometry of the melt pool and its thermo-fluid boundary conditions. Avegnon et al.[108] investigated LPBF-processed 316 stainless steel and found that even within the conventionally accepted dense-build energy window, micropores could still exhibit distinct spatial periodicity. Through combined X-ray CT and flow field analysis, they attributed this phenomenon to weakened convective heat transfer caused by periodic obstruction of the protective gas flow by the recoater blade, which resulted in local heat accumulation, deeper melt pools, and subsequent keyhole-type micropore formation. This finding suggests that microporosity does not always originate from deviations in main process parameters, but can instead arise from local instabilities induced by equipment–environment coupling.

Building upon this, Aboulkhair et al.[107] systematically investigated the influence of scan speed on pore formation mechanisms in AlSi10Mg alloys, providing a more refined understanding of microporosity evolution. Their results indicated that at lower scan speeds, metallurgical pores dominate, whereas at higher scan speeds, the proportion of keyhole-type pores increases significantly. Furthermore, they reported that surface irregularities such as balling under high-speed conditions can promote the entrapment of partially melted powder or gas in subsequent layers, thereby enhancing the probability of microporosity formation. Notably, the authors proposed that multiple scan or pre-scan strategies can improve surface smoothness and suppress keyhole pore formation without a significant loss in productivity, highlighting that microporosity is not entirely uncontrollable but highly sensitive to melt pool evolution pathways.

Beyond fusion-based metal additive manufacturing, microporosity also plays a decisive structural role in powder-based preform–post-densification routes. Cramer et al.[103] studied binder jet–fabricated SiC preforms followed by reactive silicon infiltration, systematically analyzing pore evolution throughout the printing and post-treatment stages. The study revealed that the large number of interparticle micropores formed during the initial printing phase undergo substantial closure during infiltration, but the degree of closure is strongly governed by the competition between percolation pathways and reaction kinetics. Using combined X-ray CT and neutron Bragg-edge imaging, the authors further demonstrated that the spatial heterogeneity of micropores directly reflects the advancement behavior of the reaction front, suggesting that microporosity in such processes should not be regarded as a mere "residual defect," but rather as a microstructural signature of process kinetics.

Taken together, these studies indicate that although the formation mechanisms of microporosity differ among various additive manufacturing routes, they consistently exhibit strong process dependence and localization characteristics. In LPBF and other fusion-based processes, microporosity is primarily controlled by melt pool transient stability and thermo-fluid boundary conditions, whereas in printing–post-densification processes, it results from the competition among percolation, reaction, and densification kinetics. Therefore, microporosity should not be regarded as a simple processing defect, but rather as a naturally evolved microstructural feature arising under coupled material–process conditions. This understanding provides a crucial conceptual framework for subsequent discussions on microporosity formation mechanisms in solid-state additive manufacturing.

2.2.1.1 Mesoporosity

Mesopores typically refer to the important intermediate pore state between micropores and macropores. Compared with micropores, mesopores significantly reduce mass-transfer resistance and enhance molecular diffusion rates; relative to macropores, they offer larger specific surface areas and more active interfacial sites. Consequently, mesoporous architectures play an irreplaceable role in various applications, including adsorption and separation, catalytic support, energy transport, dielectric regulation, and acoustic and thermal management[110][111].

In porous material design, mesopores rarely exist in isolation; rather, they typically coexist with micro- and macropores to form hierarchical porous structures. Within such frameworks, mesoporosity serves as a "transport–interface bridge," connecting pores of different scales and facilitating efficient coupling between structural hierarchy and functional performance.

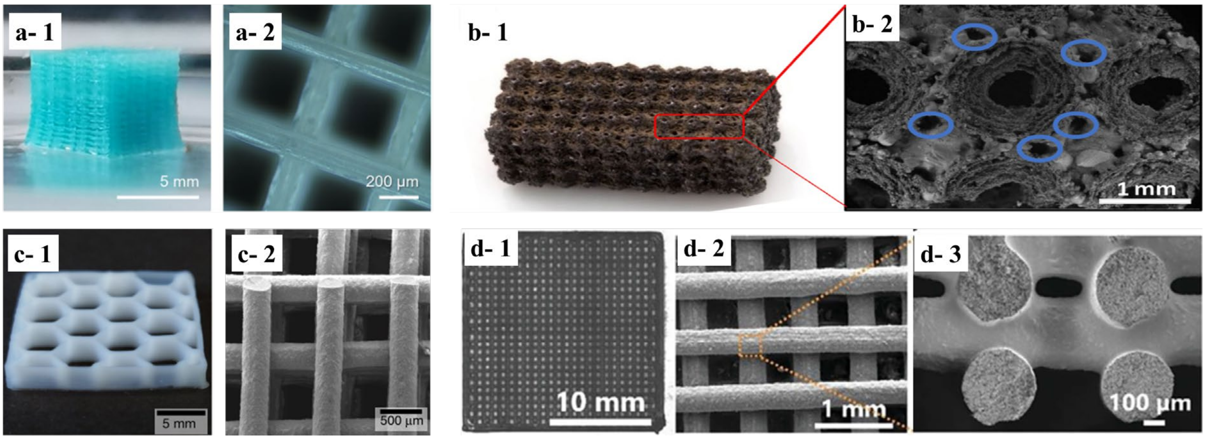

Figure 19. Mesoroporosity in different additive manufacturing processes[110][111][112][113]

In a representative study, Zhang et al.[114] systematically elucidated the mechanism of mesopore formation during solution-based additive manufacturing of porous polymers. The authors demonstrated that in ternary systems, the gradual evaporation of a volatile solvent drives the composition to cross the phase boundary, triggering spinodal decomposition and ultimately generating a continuous, interconnected mesoporous network during solidification. The resulting mesopores, predominantly in the tens-of-nanometers range, coexist with intrinsic micropores to form a multilevel pore system. Experimental results revealed that this mesoporous network markedly improves internal mass transport efficiency and suppresses the formation of dense surface skins, thereby directly enhancing adsorption and separation performance.

In another representative work, Chen et al.[113] identified mesoporosity as the dominant structural feature within polyimide aerogels fabricated by direct writing. Their review showed that the sol–gel reaction followed by drying enables the construction of a nanostructured three-dimensional network primarily composed of mesopores, yielding an overall porosity exceeding 90%. These mesopores not only endow the material with ultralow density and thermal conductivity, but also exert a decisive influence on dielectric regulation. The study further revealed that the size and uniformity of mesopores directly affect polarization behavior and dielectric loss, serving as critical structural parameters for achieving low dielectric constants and high-frequency stability.

In summary, mesoporous structures occupy a central bridging position in modern porous material systems. On one hand, their continuous nanoscale networks substantially enhance mass and heat transport as well as interfacial reaction efficiency; on the other hand, they serve as the key link that couples microscale structural properties with macroscale functional performance within hierarchical architectures. The cited studies clearly demonstrate that—whether in phase-separation-induced porous polymers or in aerogels and their additively manufactured counterparts—mesoporosity forms the structural foundation for achieving high-performance and multifunctional porous materials.

2.2.1.1 Macroporosity

Macroporosity, typically referring to pore structures ranging from several tens of micrometers to hundreds of micrometers, or even millimeter scale, represents the largest class within hierarchical porous systems. In engineering materials and metallic foams, the significance of macropores lies not in their contribution to specific surface area, but in their highly interconnected open-pore networks, which provide low-resistance pathways for the transport of fluids, gases, or biological tissues. Unlike micropores or mesopores, where transport is dominated by diffusion, macroporous structures primarily govern permeation, convection, and bulk flow behaviors, exerting fundamental influence on permeability, capillary wicking, pressure drop, and macroscopic functional response.

Jha et al.[115] systematically investigated the fabrication of high-porosity titanium foams using the space-holder method. In this process, titanium powder is mixed with removable NaCl particles, compacted, and subsequently subjected to thermal or dissolution treatment to remove the space holders, forming a highly interconnected macroporous network after sintering. The pore size and volume fraction are mainly controlled by the size and fraction of NaCl particles, typically yielding pores in the hundreds of micrometers range—representative of a classical macroporous architecture. Such structures exhibit excellent open-pore connectivity and high overall porosity, making them particularly suitable for biomedical implants and mass-transfer-related applications. However, the study also reported that insufficient diffusion between powder particles during sintering can lead to residual micropores within pore walls, degrading mechanical strength and fatigue reliability. Furthermore, since the pore geometry directly inherits the random morphology of the space-holder particles, control over pore shape and spatial distribution remains limited, restricting its applicability in load-bearing macroporous structures.

Su et al.[116] proposed a metal injection molding (MIM) process without the use of space holders for fabricating Ti64 porous materials with tunable pore structures. This method utilizes non-spherical HDH Ti64 powders of varying particle sizes, combined with conventional injection molding, catalytic debinding–thermal debinding, and vacuum sintering processes. It directly forms the porous structure by exploiting the gaps retained between particles due to incomplete densification, without introducing an external sacrificial phase. Research indicates that powder particle size and sintering temperature are the two core parameters determining pore morphology: increasing the initial powder particle size or lowering the sintering temperature both help suppress the full growth of sintering necks, thereby achieving higher porosity and larger average pore size.

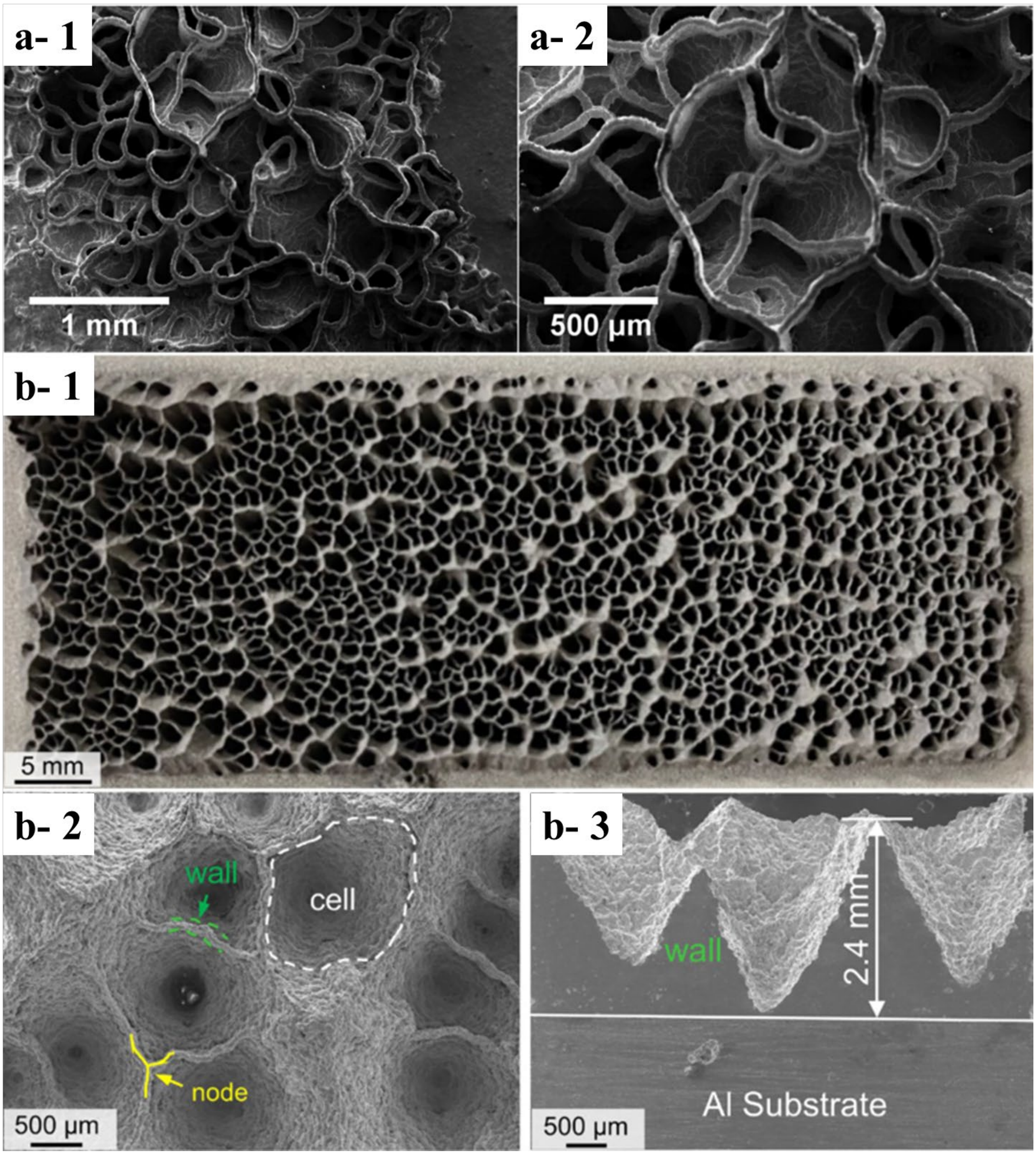

Figure 20. Macroporosity during Cold Spray Processes[117][118]

As a solid-state additive manufacturing (AM) technique, cold spray (CS) has also been explored for the fabrication of porous metallic structures. Unlike fusion-based AM, where melting and solidification dominate, cold spray relies on severe plastic deformation during supersonic particle impact, leading to solid-state bonding. Pore formation in this process primarily results from geometric mismatch between particles, non-uniform local deposition efficiency, and constrained interfacial deformation. Traditionally, such pores have been considered defects rather than functional features. Recent systematic analyses, however, have revealed that pore morphology and scale in cold-sprayed deposits are closely correlated with particle velocity, size distribution, spray path, and multilayer deposition evolution, with macropores often originating from non-uniform accumulation and topographic amplification during early deposition stages[119].

Building on this understanding, recent studies have begun to leverage inherent deposition non-uniformities to intentionally form functional macroporous structures. Notably, a 2024 study published in Scripta Materialia demonstrated[118], for the first time, the feasibility of fabricating stable cellular architectures via cold spray. Using TiH powder as feedstock, the authors exploited in-situ dehydrogenation and phase-transformation-induced mechanical contrast under ultra-high-velocity impacts to create an open cellular network composed of brick-like cells and interconnecting walls. The resulting structure exhibited clear macroporous characteristics, with cell sizes of ~400–2000 μm, wall thicknesses of 20–90 μm, and continuous pore channels extending several millimeters along the build direction. The study elucidated that these macropores originated from phase-dependent deformation heterogeneity at the impact interface, offering a new mechanistic pathway for constructing large-scale pore structures through cold spray.

Despite this progress, research on macroporous formation via cold spray remains in an early exploratory stage and faces several limitations. First, the formation of large pores is strongly dependent on specific powder systems and impact-induced phase transitions, and no generalized process design framework currently exists. Second, macroporous features often arise during early or unstable deposition stages and tend to collapse or fill with increasing layer thickness, resulting in limited structural stability and scalability. Third, the cell walls typically contain residual micropores and microcracks, whose effects on mechanical reliability and service performance remain insufficiently characterized.

Overall, existing work has primarily focused on phenomenological observation and mechanistic interpretation. Future research should aim to achieve controllable macroporous architecture design, scalable process optimization, and quantitative structure–property correlation, thereby enabling the functional utilization of macroporosity in cold-sprayed and other solid-state additive manufacturing processes.

2.2.2 Porosity formation in additive manufacturing

2.2.2.1 Laser powder bed fusion (LPBF)

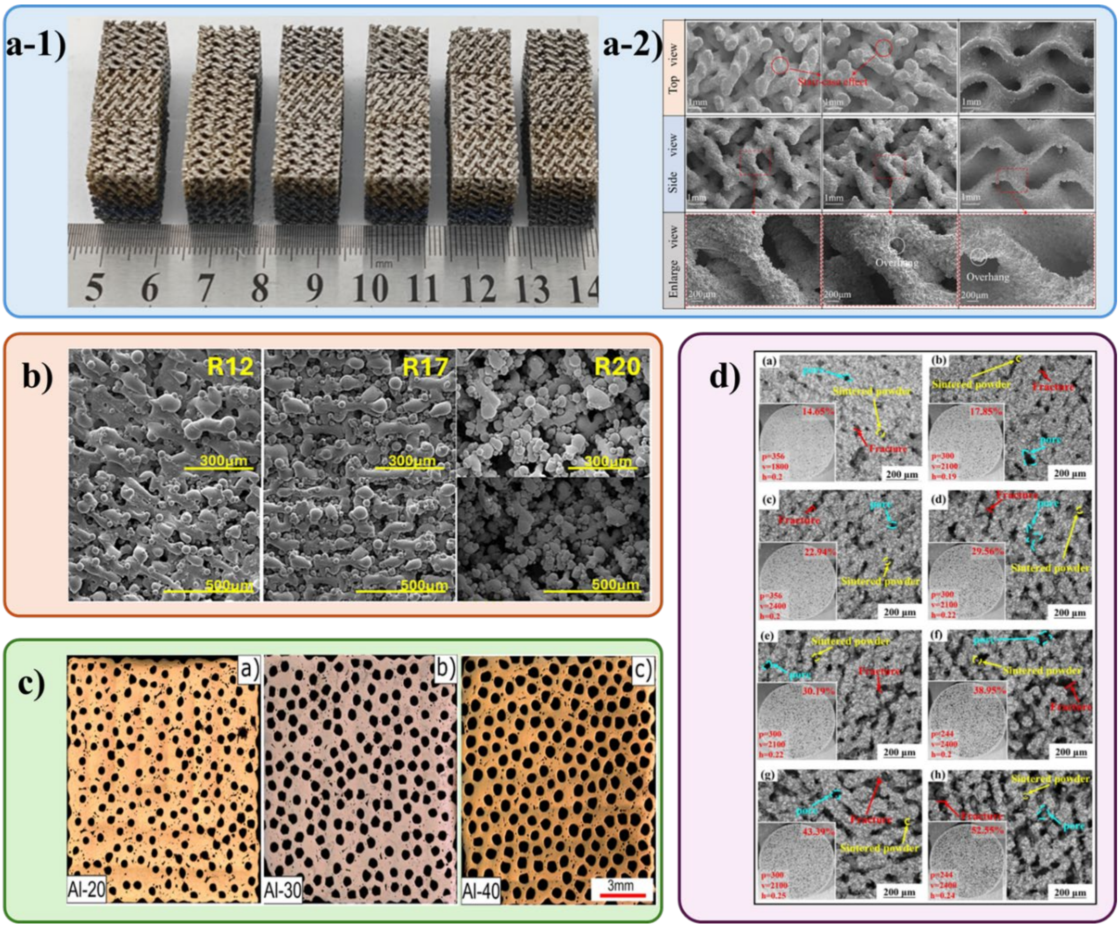

Figure. 21 Fabrication of diverse porous structures using LPBF [120][121][122][123]

Laser powder bed fusion (LPBF) is a representative fusion-based additive manufacturing technique, in which the fabrication process involves localized high energy density input, rapid melt pool formation, and subsequent rapid solidification. Fig. 21 displays several typical porous structures fabricated by LPBF. Extensive studies consistently report that porosity is a ubiquitous structural feature in LPBF components and is difficult to eliminate entirely even under optimized processing conditions. It is generally accepted that pores in LPBF primarily originate from melt pool instabilities and energy input mismatch, including lack-of-fusion defects under low energy density conditions and gas pores induced by keyhole instability and collapse at high energy densities. In addition, gas entrapment and volumetric shrinkage during solidification have also been identified as important contributors to pore formation. Accordingly, mainstream mitigation strategies have focused on optimizing the processing window in terms of energy density, adjusting scanning strategies, and employing post-processing densification treatments.

Gong et al.[124] systematically investigated the evolution of pore types as a function of energy density in LPBF-fabricated Ti64 alloys, revealing that pores formed under low energy density conditions are predominantly lack-of-fusion defects concentrated in melt track overlap regions, whereas near-spherical gas pores associated with keyhole collapse are more prevalent at high energy densities. King et al.[125] directly visualized periodic oscillation and collapse of the keyhole during LPBF using high-speed in situ imaging, providing compelling evidence that keyhole instability constitutes one of the primary physical origins of gas pore formation. For stainless steels and nickel-based superalloys, multiple studies employing X-ray micro-computed tomography (μCT) have further demonstrated pronounced spatial heterogeneity in pore distribution, with pores preferentially accumulating at interlayer boundaries and scan track intersections, reflecting the influence of local energy input fluctuations on pore formation[126][127].

It is widely recognized that porosity exerts a strongly detrimental effect on the fatigue performance of LPBF components. Even at relatively low overall porosity levels, isolated pores can act as crack initiation sites and significantly reduce fatigue life. By contrast, static tensile properties are generally less sensitive to porosity, rendering fatigue behavior the primary metric for assessing the structural severity of pores in LPBF-fabricated materials[128].

2.2.2.2 Directed energy deposition (DED)

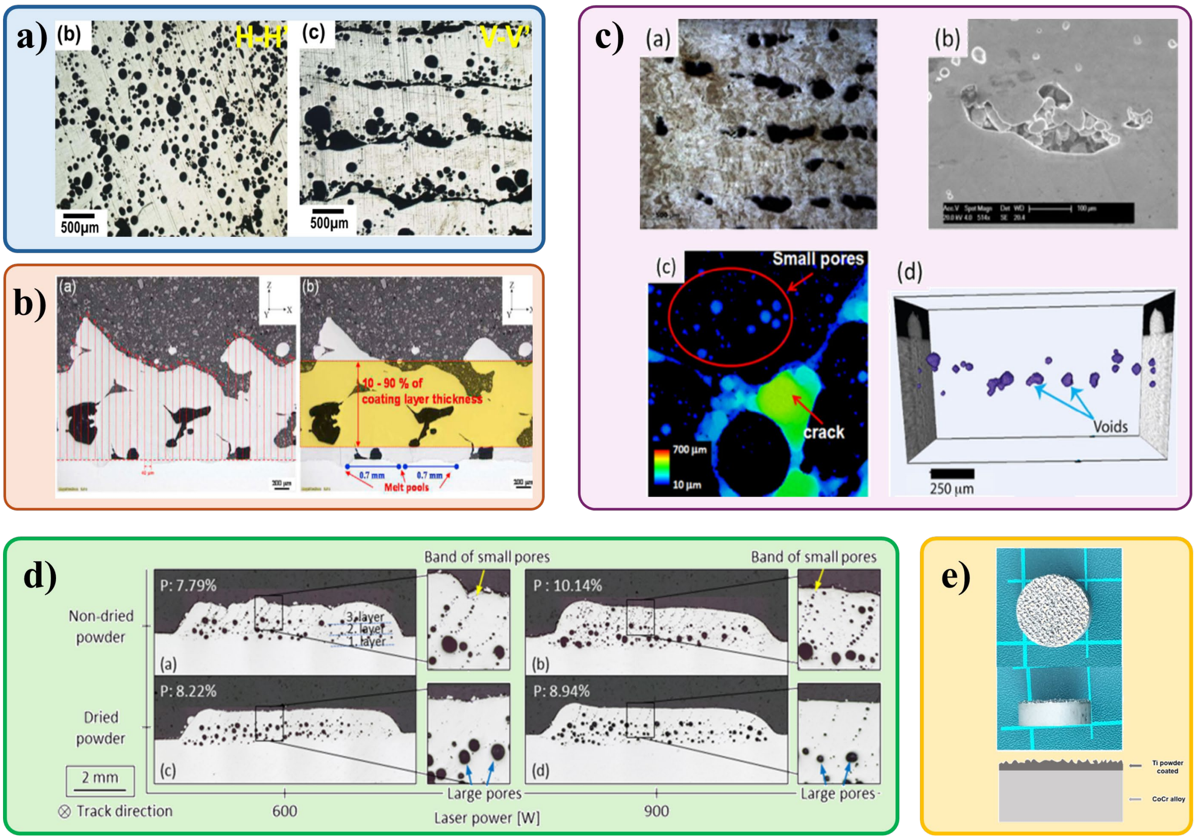

Figure. 22 Fabrication of diverse porous structures using DED [129][130][131][132][133]

Directed energy deposition (DED) is likewise a fusion-based additive manufacturing process, but is characterized by a larger melt pool, continuous material feeding, and more pronounced fluctuations in thermal input. Previous studies have shown that porosity in DED components is closely related to melt pool stability, consistency of powder (or wire) delivery, and interlayer metallurgical continuity. Fig. 22 shows some closed porous structures formed during the DED process. When material supply and energy input are mismatched, local underfilling or gas entrapment may occur within the melt pool, leading to pore formation upon solidification. As a result, porosity is generally regarded as a critical defect that must be carefully controlled in DED processes.

Kamath et al.[134][135] investigated the matching relationship between powder feed rate and laser power in laser-based DED of stainless steels and nickel-based alloys, demonstrating that unstable powder delivery directly leads to the formation of irregular pores within the deposited layers. From a thermo-fluid dynamic perspective, DebRoy et al.[130] analyzed gas escape behavior in the DED melt pool and identified melt pool flow instability as a key driver of gas pore formation. In studies on DED-fabricated titanium alloys, Kelly and Kampe observed that insufficient interlayer thermal input can introduce large-scale pores at interlayer interfaces, which are difficult to eliminate during subsequent deposition[136].

Overall, existing research indicates that porosity has a pronounced influence on the fatigue and fracture behavior of DED components, while its effect on static strength is comparatively limited. In recent years, auxiliary techniques such as interlayer rolling or hammer peening have been explored to reduce porosity levels and thereby improve fatigue performance[137][138].

2.2.2.3 Porosity in cold spray

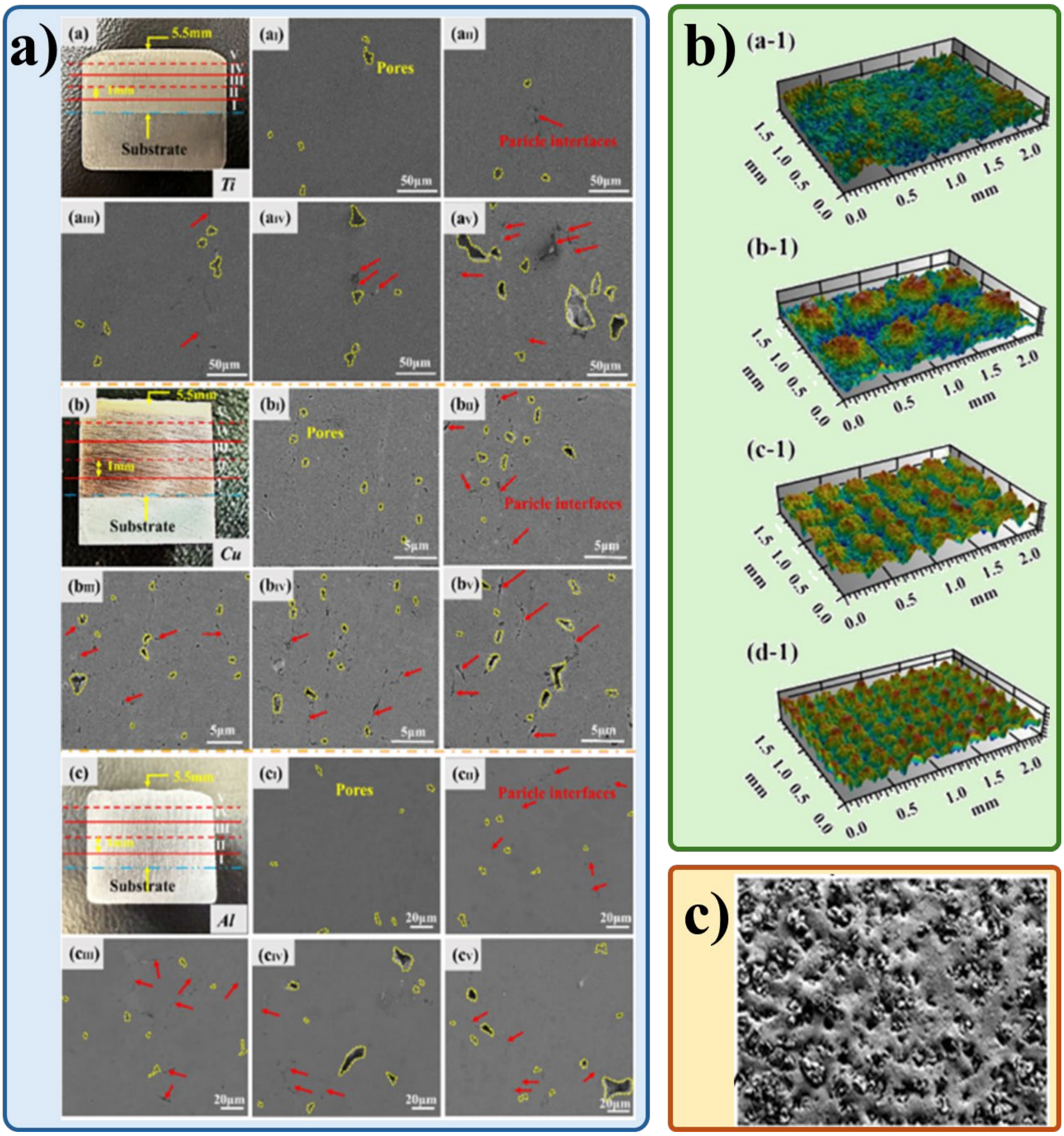

Figure. 23 Fabrication of diverse porous structures using CS [139][140][141]

In cold spray (CS) deposition, although materials remain entirely in the solid state, gas-related porosity is frequently observed and constitutes one of the key microstructural features influencing coating densification and performance. Unlike gas pores in fusion-based additive manufacturing, which arise directly from gas entrapment or solidification shrinkage, gas pores in cold spray are not associated with melting phenomena. Instead, they are more closely linked to high-velocity gas-driven conditions, particle impact dynamics, and interfacial sealing behavior. Consequently, gas porosity in cold spray exhibits distinct formation pathways and evolutionary characteristics, and has attracted increasing research attention in recent years.

Wenya Li et al.[142] systematically investigated gas entrapment behavior at particle–particle and particle–substrate interfaces during cold spray deposition, demonstrating that even under high deposition efficiency conditions, a fraction of gas may be trapped at the interface during the impact event, leading to the formation of microscale gas pores within the deposited layer. This study emphasized that gas pore formation in cold spray does not rely on material melting, but instead originates from competition between instantaneous interfacial sealing and gas escape during high-velocity impact, particularly in regions where particle flattening is insufficient or interfacial conformity is incomplete.

From a mechanistic perspective, Assadi et al.[67] highlighted the decisive role of critical velocity and particle plastic deformation in porosity formation. They proposed that when particle impact velocity is only slightly above the critical deposition velocity, adhesion can be achieved, yet interfacial plastic flow remains limited, preventing complete expulsion of entrapped gas and resulting in residual gas pores. This work provided an important explanation for the frequently observed phenomenon of "successful deposition with persistent porosity."

Champagne and co-workers[90] systematically compared cold spray deposition under different process gas conditions, such as helium and nitrogen, and demonstrated that both gas type and pressure level exert a significant influence on gas pore content. Their results showed that higher sound speed and stronger particle acceleration promote more extensive particle flattening and tighter interfacial contact, thereby reducing the likelihood of gas entrapment, whereas under lower kinetic energy conditions, gas pores are more readily retained at splat boundaries. This finding underscores the critical role of process gas selection in gas porosity control.

Jenkins et al.[143] combined microstructural characterization with mechanical testing to investigate porosity in cold-sprayed aluminum and aluminum alloy coatings. They reported that gas pores are strongly correlated with splat boundaries and insufficiently deformed regions, and exhibit pronounced spatial non-uniformity. Their results further indicated that gas porosity not only reduces the effective load-bearing area of the coating, but may also weaken inter-splat bonding, thereby adversely affecting mechanical performance.

In another series of cold spray studies, Li et al.[144] demonstrated that increasing the fraction of fine particles in the powder feedstock helps to fill inter-particle gaps and reduce gas porosity. This work highlighted that gas pore formation is not governed solely by process gas conditions, but is also closely related to particle size distribution, geometric packing, and deposition efficiency, offering a powder engineering perspective for porosity control.

In addition, Kumar et al.[145] employed three-dimensional characterization techniques to quantitatively analyze porosity in cold-sprayed coatings, revealing pronounced spatial heterogeneity in gas pore distribution. Pores were predominantly on the micrometer scale and preferentially located in regions formed during early deposition stages. Their study suggested that although repeated impacts from subsequent particles can partially compact existing pores, gas-related porosity formed at early stages is difficult to eliminate completely.

Taken together, these studies indicate that gas porosity in cold spray is governed by a combination of factors, including process gas conditions, particle impact velocity, plastic deformation extent, interfacial conformity, and powder characteristics. Unlike the "gas entrapment–solidification locking" mechanism characteristic of fusion-based additive manufacturing, gas pores in cold spray are more appropriately understood as residual structural features arising from competition between impact dynamics and interfacial sealing. While such pores are typically regarded as undesirable microstructural features in load-bearing applications, their distribution and morphology may also influence interfacial behavior and performance in certain functional coating applications.

2.2.2.4 Mixed and hybrid additive manufacturing (MHAM)

Mixed and hybrid additive manufacturing (MHAM) generally refers to manufacturing strategies that integrate additive manufacturing with additional energy fields or mechanical shaping methods, with the primary objective of improving build quality and suppressing internal defects such as porosity[146]. Existing studies indicate that MHAM does not seek to fundamentally alter the physical mechanisms governing material accumulation and pore formation. Instead, it introduces densification and reshaping mechanisms during or after deposition to suppress or repair pores that have already formed or are likely to form. Consequently, porosity related research in MHAM is predominantly concerned with how to treat pores rather than why pores form.

In fusion based additive manufacturing, the introduction of auxiliary approaches such as interlayer rolling, hammer peening, laser shock peening, or ultrasonic vibration can induce localized plastic deformation and interlayer densification, thereby significantly reducing porosity and improving metallurgical continuity between layers. Previous studies have shown that these mechanical or energy assisted methods enable secondary regulation of pore structures without modifying the original deposition parameters. In laser powder bed fusion systems, laser remelting or surface mechanical treatments can effectively close surface and near surface pores, although their influence on deep internal pores remains limited, demonstrating pronounced spatial selectivity. Ultrasonic assisted additive manufacturing has also been explored for porosity control by enhancing material flow and gas escape within the melt pool or deposited layers, but its engineering robustness has yet to be fully established[147].

Overall, MHAM enhances fatigue and fracture performance by introducing external densification mechanisms, but this is achieved at the expense of increased system complexity and cost, and such approaches are therefore more often regarded as supplementary strategies for high performance components. More importantly, current additive manufacturing research is largely centered on the paradigm of bulk porosity suppression, while insufficient attention has been paid to the formation mechanisms and controllability of surface connected porous structures[148]. In this context, the present work focuses on solid state additive manufacturing, particularly cold spray deposition, to investigate the formation and regulation of surface connected pore structures and to explore their engineering potential beyond the conventional defect control perspective.

Table. 1 Summary of Pore Material Preparation via different Additive Manufacturing

Material	**AM method**	**Pore Size/**	**Porosity/%**	**Application**	**Ref.**

		μm			
polycaprolactone (PCL)	SLM	10-610	15.1	Biomedical	[149]
FeCrMnNi	SLM	0-5um	0.20%	Pipeline-transportation, aerospace	[127]
316 steel	LMD	0-100um	7.25~15%	Lightweight materials	[150]
Ti6Al4V	3D printing	750um	65%	Biomedical	[151]
Ti alloys	DED	0-300um	0.5-2.2%	aerospace industry	[152]
316 STEEL	SLM	0-100UM	1.1-5%	Pore Optimization	[153]
Ti6Al4V	Laser Rapid Manufacturing	434um	76%	Biomedical	[154]
Inconel 718	SLM	/	3.03-23.7%	Gas turbine	[155]
AlSi7Mg	LAM	24.0um	4.22%	Structural materials	[156]
W-TiC-Y2O3	LPBF	88.6-296.6um	16.57-26.92%	Materials for Extreme	[157]

				Environment	
Fe-Ni alloy	SLM	45.05um	49%	Heat transfer	[158]
TiB2/Al	SLM	/	0.22-2.21%	Pore Optimization	[159]
Al-Si 4043	wire arc additive manufacturing	55-90um	0.95%	Automotive, aerospace	[160]
Al-Mg-Sc-Zr	wire arc additive manufacturing	17.38um	0.43%	aerospace, shipbuilding, nuclear fields	[161]
Ti6Al4V	LPBF	/	0.05-7.83%	Biomedical	[162]
Ti6Al4V	Cold Spray	>10um	1-34%	Pore Optimization	[163]
Ti-based alloy	Cold Spray	/	0-60%	Electrocatalytic Materials	[164]
Ta	Thermal spray	/	0.9-1.7%	Pore Optimization	[165]
Ti Alloy	Cold Spray	150um	/	Biomedical	[141]
Ti Alloy	Cold Spray	0-350um	5%	Biomedical	[166]

Al	Cold Spray	/	1.1-7.8%	Pore Optimization	[167]

2.3 Boiling heat transfer

2.3.1 Introduction of the boiling heat transfer

Boiling is a physical phenomenon that has long been known and used in human activities and is closely related to people's daily lives. Occurs in the solid-liquid interface on the evaporation is called boiling, that is, in the liquid in the form of producing bubbles in the form of intense vapourization phenomenon. Boiling is widely used in traditional industrial fields such as petroleum, chemical, power, machinery, metallurgy and refrigeration because of its high heat transfer coefficient[168][169][170].

Since the second half of the last century, the fields of electronic information, aerospace, biomedicine and new energy have been developing rapidly, and heat and mass transfer at micro-nano scale, microgravity and ultra-high energy flow density has become a hot research field of heat transfer[171][172]. In the field of aerospace science, with the continuous improvement of the functions of launch vehicles, space shuttles, satellite spacecraft and space stations, the number of electronic devices in the limited space of the aircraft and the rapid increase in energy flow density, the urgent need for more efficient energy and mass transfer technology[173]. In the field of electronic information science, electrical and electronic integration of precision continues to improve, high integration circuit version of the heat flow density increases dramatically, how to solve the problem of ultra-high-power heating electronic device thermal barrier has become the forefront of engineering thermophysics subjects, whether to achieve high efficiency cooling is the key to the stable and effective operation of the electronic system[174]. In the field of biomedicine, the study of the fine structure of living organisms and the law of energy transfer in various types of new bio-biochips will contribute to the development of biological and medical engineering technology[175][176]. Due to the extensive demand for energy in various frontier fields, new types of energy such as fuel cells, photovoltaic cells and heat pumps have received widespread attention, in which the heat and mass transfer process will have a great impact on the effectiveness of the energy supply and the performance of the system. In the case of electronic devices, for example, reducing the size of individual chips, further improving chip integration and increasing the clock frequency is an inevitable trend in chip research and development[177]. In the past decade, although the increase in computer processing needs, CPU chip thermal design power consumption gradually increased, the single CPU size is getting smaller and smaller, thus leading to a sharp increase in the heat flow density of electronic chips. Excessive chip heating power causes the chip temperature to rise rapidly, which poses a great challenge to the chip's work stability, reliability, and working life. Therefore, how to develop efficient electronic chip heat dissipation technology, chip operation control in a reasonable temperature range, to ensure that the CPU efficient and stable work will be the focus of future research in the field of thermal design of electronic devices, but also the research hot spots and difficulties[178][179]. Wide application space and demand for large space and microchannel boiling heat transfer applications to vigorously promote the research, and at the same time stimulate the majority of researchers to explore the boiling mechanism of great interest. In view of the boiling phenomenon in the smaller heat transfer temperature difference can achieve a very high density of heat flow and heat transfer coefficient, boiling heat transfer has become one of the most active branches of science in the field of international heat and mass transfer science[180][181].

Bi Jingliang et al[182][183] analysed the resistance of the main heat transfer methods in the heat dissipation process of electronic devices. It can be seen that the thermal resistance of boiling heat transfer is very small compared to traditional heat transfer methods such as natural convection of air or forced convection of single-phase fluids. And for the industry widely used in the nuclear state boiling can be achieved in high heat flow density, temperature stability (saturation temperature), the need for cooling fluid volume is small, and the operation of the device is simple, low-cost, no power components, do not need large and complex power equipment drive, is one of the effective ways to solve the problem of high heat flow density heat dissipation.

In summary, boiling heat transfer has the following main advantages[184][185][186]:

1. high heat flow density can be achieved with small temperature and pressure;

2. simple structure, no power parts, do not need large power equipment drive;

3. the temperature of the main fluid zone does not increase significantly during the boiling process;

4. Compared with single-phase fluid cooling technology, the required cooling medium is

small.

Boiling can occur under a variety of different conditions. For example, in pool boiling the fluid is stationary and its activity near the surface is induced by natural convection as well as mixing due to bubble growth and detachment[187][188]. In contrast, in forced convective boiling the fluid's motion is induced by external means as well as by natural convection and bubble-induced mixing. In subcooled boiling, the liquid temperature is below the saturation temperature, so bubbles formed at the surface can condense in the liquid. Conversely, in saturation boiling the temperature of the liquid is slightly above the saturation temperature, so bubbles formed on the surface are driven by buoyancy forces through the liquid and eventually escape from the free surface. Boiling phenomena can be categorised on the basis of the flow pattern of the fluid, the temperature of the fluid and the state of boiling[187][189][190][191].

1) According to the boiling heat transfer surface around the fluid is static or forced flow form, boiling can be divided into pool boiling or flow boiling. If the boiling occurs in a large space such as a kettle or pot, it is called pool boiling, also known as natural convection boiling.

2) According to the boiling heat transfer surface around the fluid whether to reach the system pressure corresponding to the saturation temperature, boiling can be divided into saturated boiling or supercooled boiling. Liquid temperature reaches the corresponding saturation temperature is called saturated boiling, below the saturation temperature is called subcooled boiling. For saturated boiling, bubbles in the heat transfer surface, growth, detachment and even rise to the surface of the liquid, while for the subcooled boiling, its bubbles in the heat transfer surface is produced in the vicinity of the condensation disappeared, the phenomenon of boiling occurs only on the surface of the boiling, so subcooled boiling is also known as the surface of the boiling.

3) According to the bubble state in the boiling process, boiling can be divided into nuclear state boiling, membrane state boiling and transition boiling. Bubbles in the boiling heat surface of tiny grooves, scratches, etc., periodic nucleation, growth, detachment, the phenomenon corresponds to the nuclear state of boiling. When the heat transfer surface is completely covered by the vapour film, the liquid evaporates through the vapour film,

which is called membrane boiling.

2.3.2 Heat transfer curves

Boiling heat transfer can be represented by the boiling curve Fig. 24, Nukiyama[192] was the first to measure the boiling curve of a large space cell in 1934 by controlling the heat flux density by electrically heating a platinum wire - the relationship between the heat flux density, q, and the degree of superheat, ΔT.

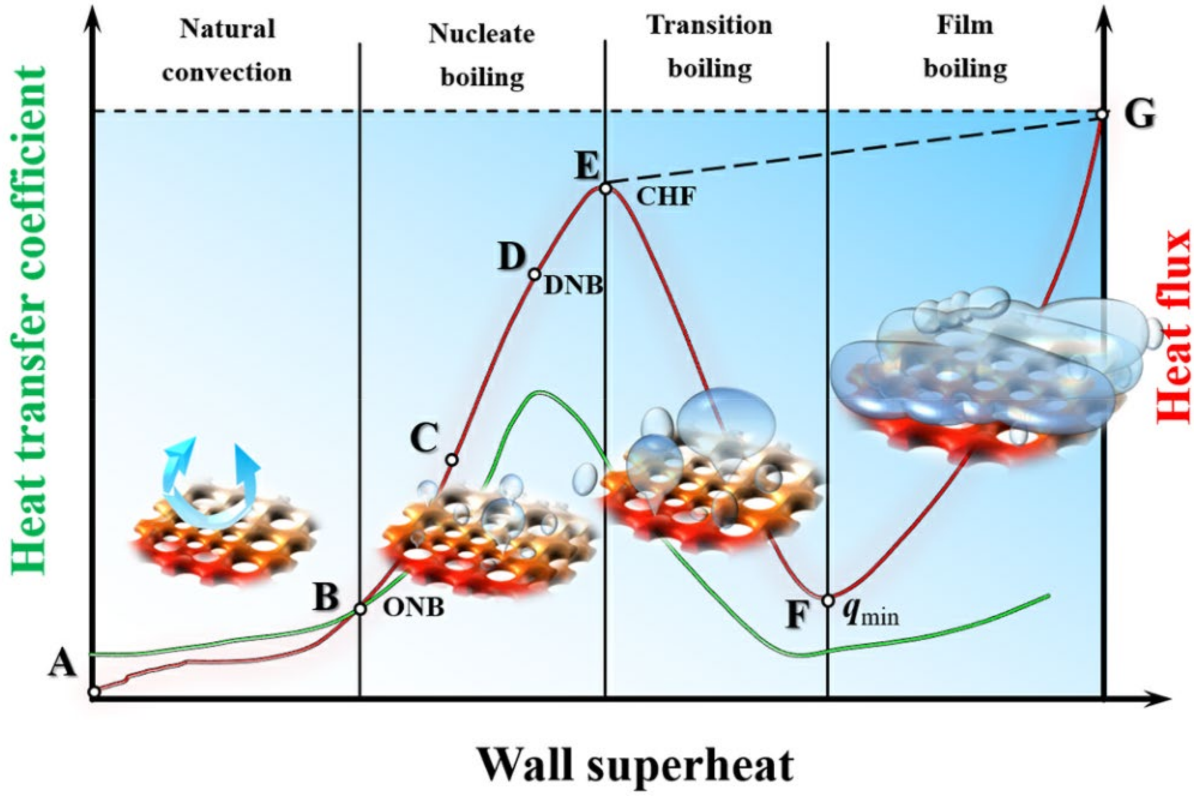

Figure. 24 Effect of boiling heat transfer at different stages[187]

Natural convection zone: wall superheat is low, the temperature of the liquid near the heated wall is heated up, gradually higher than the temperature of most of the other liquids, the temperature gradient so that the formation of natural convection between the hot and cold liquids, i.e., the AB section of the figure.

Nuclear boiling zone: the BE section in the figure for the nuclear boiling zone, B point for the boiling start. Nucleate boiling can be further divided into three segments, BC, CD and DE. BC segment is near the boiling initiation point, in this zone, bubbles will nucleate in the boiling heat transfer surface pits, slits or cracks on the core of the vapour, etc. In the CD zone, the density of the heat flow is relatively small, the degree of superheat is low, and the bubbles are generated to encourage the growth of the bubble until detachment. After a period of waiting, the next bubble cycle begins, so the CD zone is also called the isolated bubble zone. the DE zone has a higher superheat, the number of vapor cores increases significantly, the bubble nucleation and growth processes interfere with each other, and bubbles generated at adjacent vapor cores may even merge after detachment to form a column of vapor.

Critical heat flow (CHF): when the temperature of the heating surface continues to rise, the surface more right bubbles merge to form a layer of gas film, thus blocking the efficient transfer of heat between the wall and the liquid mass, so that the surface heat transfer deterioration, the boiling curve began to decline. Since at this heat flow density, the surface temperature increases dramatically, which in practice can lead to equipment burnout. Therefore, this heat flow density is the maximum heat flow density for the safe operation of the equipment, which has significant warning significance in engineering applications.

Transitional boiling zone: heat flow density exceeds the CHF after the EF section in the figure, with the increase of wall superheat, the heat flow density will be reduced, this process is called transitional boiling zone.

Membrane boiling: that is, the FG section of the figure, the heat flow density of the further increase in the surface of the vapour film will be periodically released neatly, so that the vapour is regularly detached. At this time, the heat flow density and began to increase with the wall superheat increases.

As can be seen from the figure, the intensity of heat transfer in the nuclear boiling zone is greater, and a better heat transfer effect can be achieved in the state of low wall superheat, so the heat dissipation of high heat flow density equipment in general industry is designed in this zone, the so-called enhanced heat transfer generally refers to the enhancement of the heat transfer in the nuclear boiling stage or to extend the existence of the time of the nuclear boiling.

In addition to CHF, there are two other important parameters for heat transfer in nuclear state boiling, which are critical heat transfer coefficient (HTC) and onset of boiling (ONB). The HTC is the ratio of heat flow density and wall superheat, which indicates the strength of the heat exchange capacity of the heat exchange surface, and the ONB is the point at which the boiling state starts to enter the nuclear boiling zone, i.e., the point corresponding to the surface when bubbles start to be generated. the lower the wall superheat corresponding to the ONB is, the easier it is for the surface to enter the nuclear boiling state by boiling, and the better the heat exchange performance of the surface, the more favourable it is for industrial applications. Therefore, what is generally referred to as enhanced nuclear state boiling heat transfer is mainly to increase the CHF and HTC of the heating surface and reduce the wall superheat required for ONB.

Zuber[193] proposed a theory of hydraulic instability for CHF and applied it to derive the CHF formula $(2.3.2-1)$ for a smooth surface approximated to infinity, which is 110.8 W*cm^-2 at atmospheric pressure with water as the liquid mass.Lienhard et al., on the other hand, proposed a CHF expression $(2.3.2-2)$ for a different constant of proportionality by modifying the Helmholtz wavelengths applied by Zuber, which is 126.9 $W\cdot cm^{-2}$ for the CHF obtained in actual boiling experiments with water as the liquid mass. CHF expression $(2.3.2-2)$, which is 126.9$W\cdot cm^{-2}$ at atmospheric pressure with water as the work material.Most of the CHFs in the smooth planes obtained in actual boiling experiments with water as the work material also lie in the 100-160$W\cdot cm^{-2}$ interval. This heat flow density is far from meeting the heat dissipation requirements of high power density electronic devices (usually hundreds to thousands of $W\cdot cm^{-2}$). Therefore, the method to effectively strengthen the surface boiling heat transfer performance is very necessary in engineering applications.

$$q''_{CHF} = 0.131\sqrt{\rho_v}h_{lv}[\sigma g(\rho_l - \rho_v)]^{\frac{1}{4}} \qquad (2.3.2-1)$$

$$q''_{CHF} = 0.149\sqrt{\rho_v}h_{lv}[\sigma g(\rho_l - \rho_v)]^{\frac{1}{4}} \qquad (2.3.2-2)$$

Where ρ_v and ρ_l are the density of the gas and liquid respectively (kg/m^3), σ is the surface tension (N/m),g is the acceleration of gravity (m^2/s), and h_{lv} is the latent heat of vaporisation of the work material.

As the working principle of boiling heat transfer is to heat the surface to transfer heat to the liquid mass, the liquid mass absorbs a large amount of latent heat phase change (i.e., produce bubbles) so that the heat will be taken away. Therefore, the influencing factors of the performance of boiling heat transfer can be divided into three categories: the performance of heat transfer surface, the liquid mass and the applied vector field.

2.3.4 Influence of heat transfer surface properties

2.3.4.1 Material of the heat transfer surface

The first is the influence of the material of the heat transfer surface. Typically, heat transfer surfaces of different materials have different thermal conductivity[194][195]. Compared with common organic compounds, such as polyethyleneimine (PEI), the thermal conductivity of metals and metal compounds will be more than one order of magnitude higher, and the high thermal conductivity is conducive to the transfer of heat from the surface, so that the surface can be boiled at a much lower degree of superheat, resulting in a better performance of boiling heat transfer. In addition, the wall surface of different materials has different adsorption force of the liquid medium, i.e., there is a difference in the wettability of the surface, so that the surface's ability to replenish the liquid during the boiling process is also different. The ability to replenish the liquid affects the dry state of the surface, which in turn affects the heat transfer performance.

Secondly, it is the effect of the morphology of the heat transfer surface[196][197][198][199]. ince the surface boiling heat transfer performance mainly depends on the growth, growth and detachment of bubbles, and the performance morphology seriously affects the growth process of bubbles, so the surface morphology has a great influence on the boiling heat transfer performance. The irregular cracks, pits, bumps and other micro/nano-scale structures on the heat transfer surface not only affect the nucleation and growth process of bubbles, but also affect the number and distribution of wall vaporisation cores, thus directly affecting the surface boiling heat transfer performance[200][201].

2.3.4.2 Influence of the liquid medium.

There are significant differences in the latent heat of vaporisation, thermal conductivity, surface tension, etc. of different liquid substances[202][203]. Therefore, in the boiling process, the liquid mass phase change is the heat absorption capacity and heat transfer rate are also different. Surface tension mainly affects the bubble growth and detachment process, if the boiling liquid mass to add surfactant, the surface tension of the liquid mass will be significantly reduced, so that the energy required for bubble growth is reduced. Therefore, when the heating heat flow is certain, the heat transfer surface is easy to produce more bubbles, and the bubble detachment frequency will increase, thus strengthening the boiling heat transfer effect. In addition, the addition of nanoparticles with good thermal conductivity in the liquid mass is also a common and effective method to strengthen the boiling heat transfer[204][205].

2.3.4.3 Influence of applied vector fields.

By applying electric field and magnetic field to the boiling heat exchange system, the flow state of the liquid medium and the growth and detachment process of the bubbles can be adjusted, so as to regulate the boiling heat exchange[206][207].

Since the external vector field requires additional equipment and power energy consumption, it is limited by the conditions and places of use in practice. Moreover, this method has higher requirements on the liquid medium, such as when the electric field enhances the heat transfer, it is necessary to make use of the difference in the conductive properties of the two substances that make up the phase interface to regulate the motion performance of the liquid medium or the bubbles. Therefore, the enhancement of boiling heat transfer effect through an applied vector field is not significant for industrial applications[208][209].

Based on the above mentioned factors affecting boiling heat transfer, the main focus of current researchers is to enhance boiling heat transfer by changing the liquid boiling mass and modifying the boiling surface.

2.4 Summary for research gap

In summary, substantial progress has been achieved over the past decade in exploiting porous structures for the enhancement of boiling heat transfer. Whether realized through sintered particles, electrochemical deposition, anodic oxidation, fusion-based additive manufacturing, or metallic foam architectures, a broad body of literature has consistently demonstrated that porous surfaces can significantly improve critical heat flux (CHF) and heat transfer coefficient (HTC) by increasing nucleation site density, enhancing capillary-driven liquid replenishment, and suppressing vapor film formation. Nevertheless, when viewed collectively, existing studies on porous heat-transfer surfaces still exhibit several structural limitations, most notably a misalignment between pore structure type, fabrication strategy, and engineering applicability.

First, in terms of research focus, most existing studies predominantly concentrate on bulk porosity. In fusion-based additive manufacturing processes such as LPBF and DED, bulk pores are generally regarded as detrimental defects that degrade mechanical performance, and research efforts are therefore directed toward their elimination through process optimization or post-processing treatments. In solid-state or chemically derived porous surfaces, although porosity is intentionally introduced for heat-transfer enhancement, the investigated structures are still largely bulk pore networks within deposited layers or substrates, with evaluation metrics centered on porosity level, average pore size, or coating thickness. By contrast, surface-connected pore structures that directly interact with the external environment and actively participate in liquid supply and vapor removal remain insufficiently explored in a systematic manner. As a result, many reported enhancements in CHF or HTC rely on the averaged effect of an overall porous layer, rather than on precise control of the specific surface pore features that dominantly govern boiling heat-transfer processes.

Second, from a fabrication perspective, the mainstream routes for producing porous heat-transfer surfaces suffer from clear limitations in engineering applicability. For example, sintered particle coatings and electrochemical deposition can generate rich micro- and nanoscale porosity, but typically require high-temperature treatments, complex chemical environments, or multistep processing routes. These constraints limit fabrication scale, compromise structural uniformity, and often result in insufficient mechanical robustness, making such structures prone to collapse or performance degradation under high heat fluxes or prolonged boiling conditions. Anodic oxidation and chemical etching offer advantages in producing ordered micro- or nanostructures, yet their applicability is restricted to a narrow range of material systems, limiting their transferability to high-strength alloys commonly used in engineering applications. Metallic foams and fully open cellular structures provide excellent three-dimensional connectivity, but their relatively large pore sizes make it difficult to simultaneously optimize vapor evacuation and liquid replenishment, and under high heat fluxes they may even induce heat-transfer deterioration.

Furthermore, fusion-based additive manufacturing exhibits intrinsic contradictions when applied to the fabrication of boiling heat-transfer surfaces. Although techniques such as LPBF offer exceptional geometric design freedom, their fundamental objectives are densification and structural integrity. As a result, porous structures are typically realized through predesigned geometries, with pore size and connectivity strictly constrained by process resolution and melt pool stability. Moreover, the inevitable melting–solidification cycles introduce residual stresses, surface oxidation, and variability in material properties, which may compromise interfacial reliability under high-frequency boiling conditions. Consequently, fusion-based additive manufacturing is more suitable for load-bearing or flow-channel-oriented structures, rather than for applications such as boiling heat transfer that are highly sensitive to surface microstructure and interfacial phenomena.

Against this background, cold spray, as a solid-state additive manufacturing technique, offers a distinctive and largely underexplored pathway for the development of advanced porous heat-transfer surfaces. Because cold spray does not involve material melting or solidification, deposited layers retain intrinsic material characteristics while avoiding oxidation, phase transformation, and residual stress associated with high-temperature processing. This makes cold spray particularly attractive for heat-transfer applications requiring high interfacial stability and long-term reliability. More importantly, cold spray inherently features non-uniform initial deposition, deposition–erosion competition, and the cooperative evolution of multiscale pore structures, enabling the spontaneous formation of surface-connected pores and hierarchical porous networks without reliance on predesigned pore architectures.

A limited number of recent studies have begun to demonstrate that, by tailoring particle impact dynamics, spray stability, and material system characteristics in cold spray, stable surface-connected pore structures can be induced on deposited layers. Unlike conventional bulk pores, these surface-connected pores can directly participate in liquid replenishment, bubble growth, and vapor evacuation during boiling, offering higher functional efficiency and more direct contributions to heat transfer. However, compared with the extensive literature on cold-spray densification, mechanical performance, and bulk porosity control, systematic investigations into the formation mechanisms, evolutionary behavior, and heat-transfer enhancement roles of surface-connected pores remain scarce. Correspondingly, clear structure–process–performance relationships for such pores have yet to be established, and their underlying heat-transfer mechanisms remain insufficiently elucidated.

Therefore, from the combined perspectives of research gaps and engineering demand, there is a compelling need to shift the research paradigm from "how to eliminate porosity" toward "how to exploit and control surface-connected porosity," with solid-state additive manufacturing techniques such as cold spray serving as a central research focus. Such a shift not only addresses the long-standing underrepresentation of surface open pores in porous heat-transfer surface research, but also opens a promising avenue toward the development of heat-transfer surfaces that simultaneously offer structural controllability, process scalability, and practical engineering applicability.

Chapter 3 Formation mechanism and microstructural evolution of porous Ti64 structures via cold spray

This chapter first conducts a comparative deposition study of three representative metallic powders, namely Al, Cu, and Ti64, under identical cold spray processing parameters in order to establish the structural basis for material selection. The experimental results indicate that, under the same spraying conditions, both Al and Cu tend to form continuous and relatively dense deposits. Their surfaces are mainly characterized by rough morphologies produced by particle accumulation, while a stable interconnected open pore network structure does not form spontaneously. In contrast, the Ti64 deposit exhibits distinctly different surface morphological characteristics. A honeycomb like open pore structure is formed on the surface, with pore sizes reaching several hundred micrometers. This structure is accompanied by wall like skeletons growing along the deposition direction, thereby forming a highly interconnected three dimensional porous network. It is noteworthy that this structure is not obtained through template assistance or post processing regulation, but instead forms spontaneously during the deposition process, demonstrating a pronounced material dominated characteristic.

Based on the above comparative results, and considering that the objective of this study is to enhance boiling heat transfer performance, Ti64 was selected as the core material system for the subsequent mechanistic investigation and functional verification. Compared with Al and Cu, Ti64 more readily forms surface open pore structures during the cold spray process. The fundamental reason lies in the coupling effect between the intrinsic material properties and the deposition dynamics of cold spray. Ti64 possesses a relatively high critical deposition velocity. Under identical gas process parameters, the actual flight velocities of particles exhibit a certain degree of dispersion. During the initial stage of deposition, some particles tend to rebound or fracture upon impact, which leads to the formation of spatially selective bonding regions in the early stage of deposition. As the number of deposited layers increases, the deposition non-uniformity formed during the initial stage is continuously inherited and progressively amplified throughout the multilayer deposition process. Regions with relatively high deposition efficiency gradually evolve into load bearing skeleton structures, while regions with lower deposition efficiency progressively develop into interconnected open pore channels, eventually forming a stable honeycomb like surface open pore network. Therefore, the formation of the Ti64 surface open pore structure is not a random defect phenomenon. Instead, it represents an inevitable outcome jointly driven by the characteristics of high strength materials, the dispersion of particle velocities, and selective deposition behavior. This material dominated porous structure formation mechanism provides the foundation for the subsequent systematic clarification of the relationship between structural evolution and functional performance.

Based on the above research background, the main objectives of this chapter are as follows.

- To systematically compare the deposition behavior and surface morphological characteristics of Al, Cu, and Ti64 under identical cold spray processing conditions, thereby clarifying the differences in deposition structure evolution among different materials.
- To focus on the analysis of the formation characteristics and spatial morphological features of the surface open pore honeycomb structure formed during the cold spray deposition of Ti64.
- To elucidate the physical mechanism responsible for the formation of the Ti64 surface open pore structure from the perspective of the coupling between particle deposition dynamics and intrinsic material properties.
- To provide the structural and mechanistic basis for the boiling heat transfer performance investigation and functional validation of this porous structure presented in the subsequent chapters.

3.1 Material and methodology

3.1.1 Feedstock powder and cold spray process

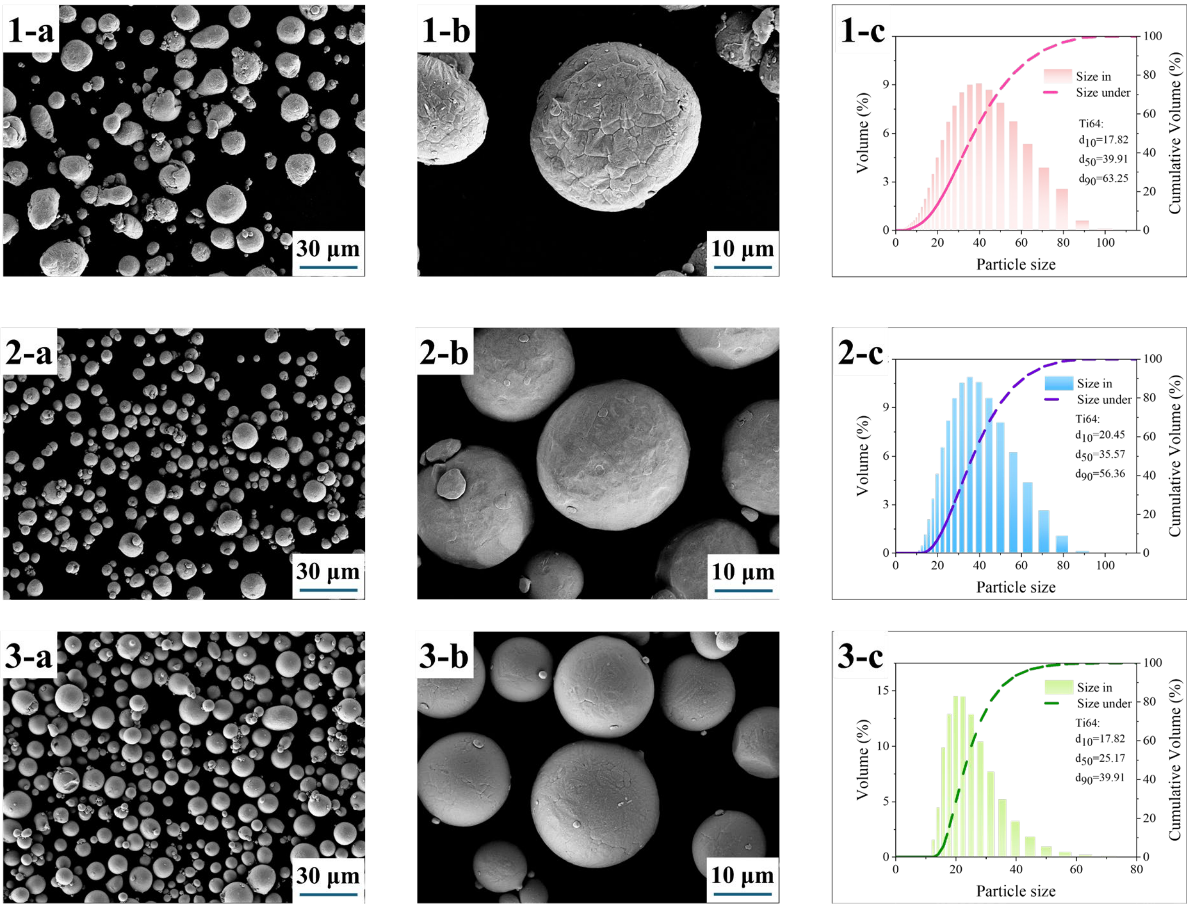

Figure. 25 1-a), 2-a), 3-a) Low magnification SEM characterization of the gas atomized Al, Cu and Ti64 amorphous powder for cold spray process. 1-b), 2-b), 3-b) High magnification SEM characterization of the gas atomized Al, Cu and Ti64 amorphous powder for cold spray process. 1-c), 2-c), 3-c) Particle size distribution of the Al, Cu and Ti64 powder.

The starting material used in this study was aerosolised Al, Cu and Ti64 powder, which was purchased from Powder Range, U.S.A. Fig.25-1-a), 2-a), 3-a) shows the Al, Cu and Ti64 powder after atomisation as observed by scanning electron microscopy (SEM, Carl Zeiss ULTRA Plus, Germany). Most of the feedstock particles are highly spherical with smooth surfaces. Some microsatellite powder particles were attached to larger powders due to different condensation rates. The size distribution of the powder was obtained by a laser diffraction particle analyzer (Mastersizer 2000, Malvern Instruments, UK), and is shown in Fig. 25-1-c), 2-c), 3-c).

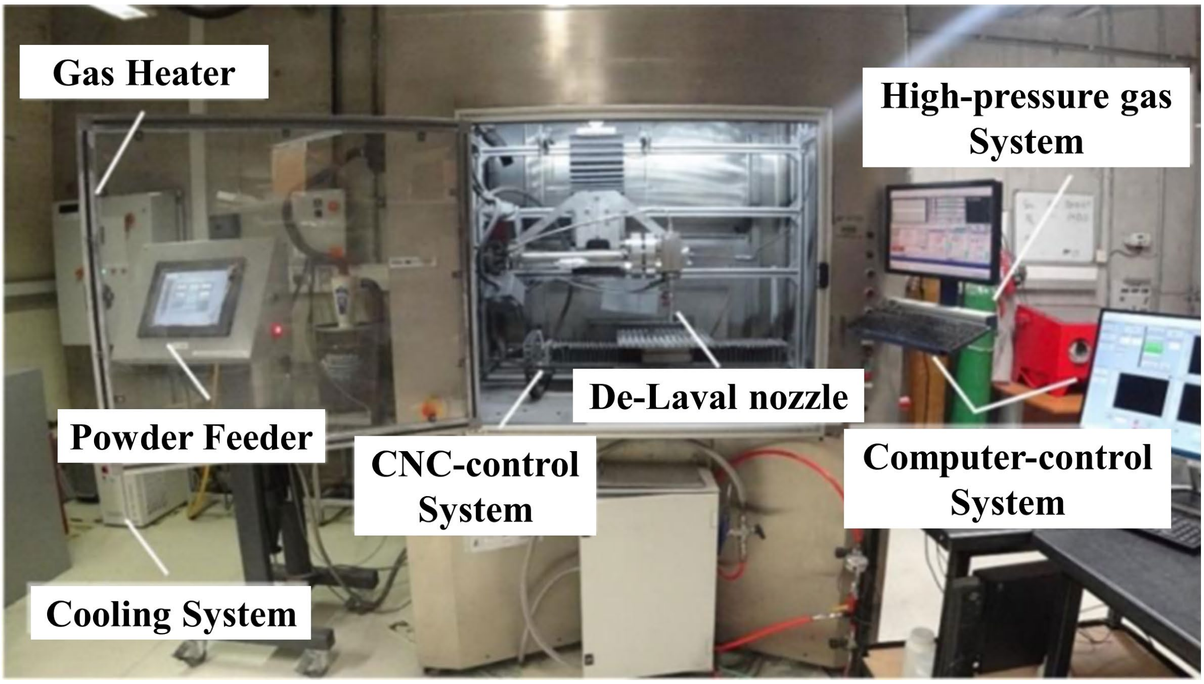

Figure. 26 In-house cold spray system in Trinity College Dublin[210]

The Ti64 powder was deposited on an Al6082 substrate by means of an in-house cold spray machine in the STAM laboratory of Trinity College Dublin, shows in Fig. 26. The system consists of a CNC-controlled working platform, De-Laval nozzle, gas heater, powder feeder, high pressure gas cylinder and a computer control module. The De-Laval nozzle has a circular cross-section, a converging length of 30 mm, a diverging length of 180 mm, an inlet diameter of 10 mm, a throat diameter of 2 mm, and an outlet diameter of 6 mm.

With reference to the processing parameters reported in previous studies and considering the maximum capacity of the laboratory cold spray system, a porous surface was created on an aluminium substrate by using the parameter as follow: the Travelling Speed (TS): 2000mm/min, the Powder Feeder Rate (PFR): 0.27g/s, and the number of layers: 4 layers.

Table. 2 Cold Spray Parameters for Different Powders

No.	Material	Temperature	Gas	Pressure	TS	PFR
1	Cu	250 °C	N_2	30 bar	1000 mm/min	0.27g/min
2	Cu	300 °C	N_2	30 bar	1000 mm/min	0.27g/min
3	Cu	350 °C	N_2	30 bar	1000 mm/min	0.27g/min
4	Al	250 °C	N_2	30 bar	50 mm/min	0.27g/min
5	Al	300 °C	N_2	30 bar	50 mm/min	0.27g/min
6	Al	350 °C	N_2	30 bar	50 mm/min	0.27g/min
7	Ti64	600 °C	N_2	30 bar	2000 mm/min	0.27g/min

3.1.2 Microstructure characterization

Scanning electron microscopy (SEM, Zeiss Ultra) was used to analyse the morphology of the pristine powders as well as the boiling heat exchanger surfaces prepared by cold spraying. 3D model reconstruction of the surface deposits was facilitated by a Nikon XTH225 ST X-ray CT (Computed Tomography) system.

3.1.3 Mechanical properties

The microhardness of Ti64 deposits produced by cold spraying was tested at room temperature using a Vickers hardness tester (ZHV30-M, ZwickRoell, UK), applying a load of 500g with a dwell time of 10 seconds. Indentation morphology was characterised via scanning electron microscopy. To ensure data accuracy, indentation tests were conducted on randomly selected areas of the polished interface.

3.1.4 Uncertainty analysis

To ensure the reliability of the experimental results presented in this chapter, an uncertainty analysis was conducted for the primary measurements involved in the mechanical and microstructural characterization. The uncertainties mainly originate from the measurement accuracy of the testing instruments, specimen preparation, and experimental repeatability.

For the nanoindentation measurements, multiple indentations were performed within each selected region to minimise the influence of local microstructural heterogeneity. The reported hardness values correspond to the arithmetic mean of all valid measurements, while the standard deviation was used to evaluate the repeatability of the results.

Tensile properties were evaluated using three independently prepared specimens under identical testing conditions. The dimensions of each tensile specimen were measured prior to testing using calibrated measuring equipment, and all tests were performed using the same loading configuration and crosshead speed. The reported ultimate tensile strength, yield strength and elongation represent the average values of the repeated measurements, whereas the corresponding standard deviations are presented to quantify the experimental variability.

For dimensional measurements, including coating thickness and specimen geometry, calibrated optical microscopy and image analysis software were employed. Instrument calibration was performed prior to testing according to the manufacturer's recommendations. The uncertainties associated with these measurements were considerably smaller than the observed differences between experimental groups and therefore do not influence the conclusions drawn in this chapter.

Overall, the uncertainty associated with the primary measured quantities was minimised through equipment calibration, repeated measurements and consistent testing procedures, ensuring the reliability and reproducibility of the reported mechanical and microstructural characterisation results.

3.2 Microstructural and pore distribution characteristics

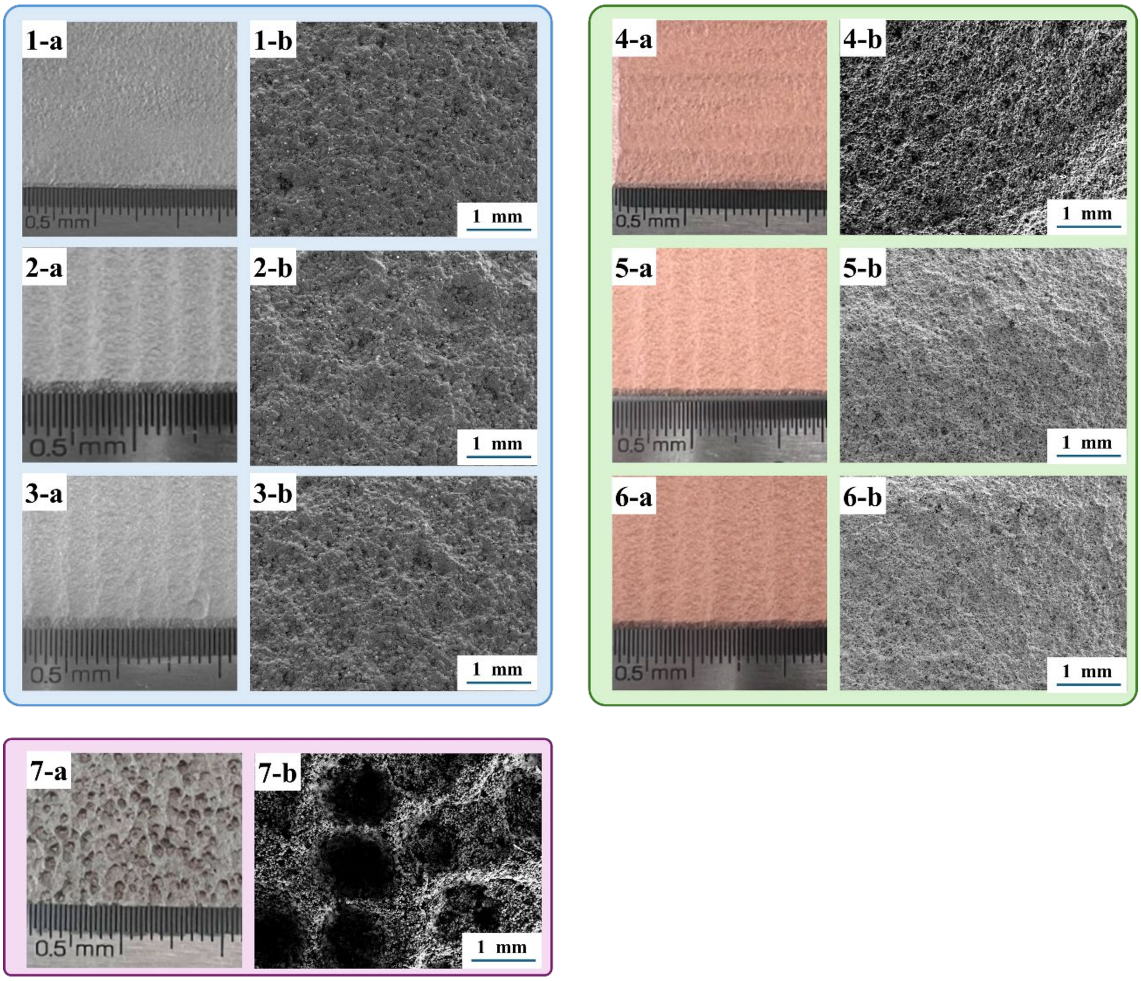

Figure. 27 Deposition Behavior of Cold Spraying for Different Materials

The Fig.27 presents a comparative analysis of the surface morphologies obtained for three different materials under identical cold spray processing conditions. Images 1 to images 3 correspond to cold sprayed Al coatings, 4 to 5 to cold sprayed Cu coatings, and images 7 to cold sprayed Ti64 coatings. From the macroscopic views in a series, it is evident that the three materials exhibit markedly different surface characteristics after deposition. Both cold sprayed Al and Cu form relatively smooth and continuous coating surfaces. At the macroscopic scale, no pronounced through pores or large-scale undulations are observed. The deposited layers appear as uniformly distributed, dense coatings covering the substrate, with surface textures dominated by fine particle accumulation that produces a homogeneous rough appearance while maintaining overall planarity.

In contrast, the cold sprayed Ti64 coating displays a fundamentally different macroscopic morphology. As shown in image 3-a, the surface is not continuous and flat but instead contains numerous open pore structures ranging from several hundred micrometers to millimeter scale. These pores are interconnected by wall like structures, forming a honeycomb like distribution. The large scale surface undulations result in pronounced spatial heterogeneity at the macroscopic level, clearly distinguishing the Ti64 coating from the comparatively flat Al and Cu coatings.

Further examination of the high magnification SEM images in the b series enables detailed analysis of the microstructural features. Although both Al and Cu coatings exhibit typical cold spray particle accumulation characteristics, with surfaces composed of plastically deformed particles and particle interfaces, and containing localized micropores and roughness at the micron scale, the overall height variation remains limited. The surface topography is dominated by micrometer scale roughness variations. While small depressions exist between particles, no extensive interconnected cavity networks are formed, and the coatings remain predominantly dense.

The Ti64 coating, however, exhibits a distinct dual scale structural characteristic. On one hand, its surface contains the typical microscale roughness resulting from plastically deformed cold spray particles. On the other hand, this microscale texture is superimposed on a macroscopic honeycomb like undulating structure at the hundred micrometer to millimeter scale. The SEM images clearly reveal deep cavity regions and elevated wall structures, with some pores showing a tendency toward through thickness connectivity. This composite architecture, characterized by large scale undulations combined with fine scale roughness, endows the Ti64 coating with both macroscopic structural modulation capability and microscopic rough interfacial features, forming a hierarchical structure.

From the perspective of heat transfer mechanisms, such structural characteristics offer potential advantages for boiling heat transfer. The microscale rough surface increases the effective nucleation site density, facilitating bubble formation and stable growth at lower wall superheat. Meanwhile, the spatial separation created by the wall structures between pores can partially suppress rapid lateral bubble coalescence, thereby reducing the likelihood of large scale vapor blanket formation and delaying the onset of film boiling. Consequently, the hierarchical honeycomb porous structure observed in the Ti64 coating provides a synergistic enhancement effect in both bubble generation and bubble behavior regulation.

Given that the objective of this work is to systematically investigate the application potential of porous coatings for boiling heat transfer enhancement, the comparative results indicate that among the three materials, the Ti64 coating exhibits the most advantageous structural characteristics due to its honeycomb like multiscale architecture. Therefore, the present chapter and the subsequent chapter focus primarily on Ti64 honeycomb porous coatings, with detailed investigation of their formation mechanisms, structural evolution, and boiling heat transfer performance under pool boiling conditions, in order to establish the intrinsic relationship between structure and performance.

3.2.1 Cell–wall porous structure formation during cold spray

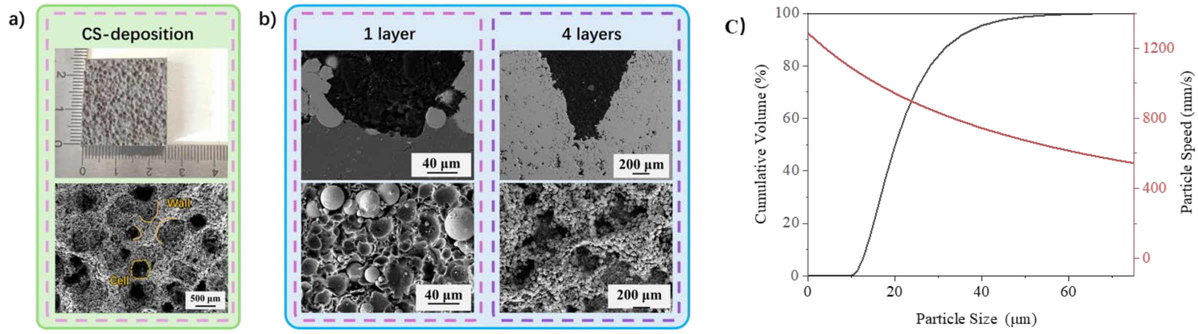

Figure. 28 a) Macroscopic and local magnification (30x) of the surface of the openings prepared by cold spray. b) Cross-section and top view of the cold sprayed one- and four-layer deposited samples. c) The relationship between Ti64 particle size and particle velocity

Fig. 28-a shows the macroscopic morphology of the porous surface layer fabricated by the cold spray process. Overall, the deposited surface is not continuous or fully dense but consists of numerous surface openings of various sizes that are randomly distributed. These openings show no periodic or regular arrangement, and both their size and spacing display significant statistical variation. This indicates that the porous structure was not formed through any pre-designed template or external regulation but rather evolved naturally through the complex coupling of multiple factors during the cold spray deposition process. Further morphological analysis reveals that these surface pores can be clearly divided into two basic structural units: cells, which correspond to recessed cavity regions, and walls, which are ridge-like structures formed by the continuous accumulation of particles.

Quantitative analysis shows that the equivalent size of the cells ranges from 250 μm to 700 μm, with an average value of about 430 μm, which falls within the typical meso-scale pore size range. In contrast, the walls exhibit stronger geometric anisotropy, with thicknesses between 50 μm and 260 μm, and extend vertically to depths of about 590 μm. This demonstrates that the walls are not confined to the surface but penetrate deep into the deposited layer, forming a three-dimensional cellular framework. As a result, the deposited surface presents a highly rough and interconnected open-cell morphology on the macroscopic scale.

Fig. 28-b compares the cross-sectional morphologies obtained after single-layer and four-layer depositions to reveal the formation process and evolution of the cell–wall structure. When only a single layer of Ti64 is deposited, the particles do not achieve uniform or continuous coverage on the Al6082 substrate. Instead, effective bonding occurs only in certain local regions, while other areas show very low or even negligible deposition efficiency. This demonstrates that the deposition process at the initial stage is strongly non-uniform across the surface.

In the regions where deposition occurs, Ti64 particles undergo localized plastic deformation upon high-velocity impact and bond with the substrate. In contrast, in areas where deposition fails, the relatively hard Ti64 particles retain their spherical morphology and rebound after impact without remaining on the surface. Meanwhile, the softer Al6082 substrate undergoes significant plastic deformation during particle impact and rebound, leaving circular or near-circular craters whose diameters are comparable to the particle size. The random spatial distribution of these craters creates the initial surface irregularity that governs the subsequent deposition process.

As the number of deposited layers increases, regions that achieved initial bonding exhibit higher deposition efficiency during subsequent spraying. On one hand, these areas already contain a roughened surface that provides favorable impact angles for further adhesion. On the other hand, the cratered regions, due to their recessed geometry and repeated erosion, remain low-efficiency areas where stable accumulation is difficult. As a result, particles preferentially accumulate on the initially deposited regions, causing these areas to thicken and grow upward, forming localized wall-like structures.

At the same time, the surrounding regions with lower deposition efficiency gradually evolve into relatively recessed cell areas. When the number of layers reaches approximately four, this non-uniform growth pattern becomes increasingly pronounced, leading to the formation of a honeycomb-like structure where the cells are enclosed by the walls. It should be noted that this structure is not produced by post-deposition etching or delamination but rather forms spontaneously during deposition and becomes more evident as the layer number increases.

However, this honeycomb-like porous structure exists only within a limited deposition range. When the number of layers exceeds about four, the continued growth of the walls gradually fills the cell regions, smoothing the surface and eventually resulting in a dense, continuous deposit. This indicates that the honeycomb morphology is a transient structure, which originates from the non-uniformity of the early-stage deposition and can be maintained only within a certain number of layers.

Although similar surface porous structures have been reported in earlier studies using pulsed cold spray or spray modulation techniques, their characteristic sizes are usually smaller and their stability is weaker, as they tend to collapse or be covered by subsequent layers. In contrast, the cell–wall honeycomb structure observed in this study exhibits larger feature sizes, higher stability, and a clearer evolutionary process. It therefore provides solid experimental evidence for the intrinsic relationship between the early-stage non-uniform deposition behavior in cold spray and the formation of porous surface architectures.

To provide a quantitative estimation of particle in-flight velocity, the theoretical method reported by Champagne et al.[211] was adopted. In their study, the modelling of particle velocity in cold spray was carried out in two steps. First, the gas velocity and temperature in the nozzle were calculated using one-dimensional isentropic gas-dynamic principles. Second, the interaction between the gas and particles was introduced through a drag coefficient, and the particle velocity was iteratively calculated through the nozzle using the known gas velocity.

The gas flow was first estimated using the relationship between nozzle area and Mach number:

$$\frac{A_1}{A_2} = \frac{M_2}{M_1}\left\{\frac{1+\left[\frac{\gamma-1}{2}\right]M_1^2}{1+\left[\frac{\gamma-1}{2}\right]M_2^2}\right\}^{\frac{(\gamma+1)}{2(\gamma-1)}} \tag{3.2.1.1}$$

where A_1 and A_2 are the nozzle cross-sectional areas at two different positions along the nozzle axis, M_1 and M_2 are the corresponding Mach numbers at these two positions, and γ is the ratio of gas specific heat. In this one-dimensional calculation, the Mach number is iteratively increased from an initial subsonic value at the nozzle entrance to sonic conditions at the throat and then to supersonic conditions in the diverging section. Therefore, the subscripts 1 and 2 indicate two successive calculation points along the nozzle, rather than fixed inlet and outlet positions.

Once the local Mach number distribution was obtained from Eq. (3.2.1.1), the corresponding gas-flow properties along the nozzle were determined using one-dimensional isentropic gas-dynamic relationships. According to Dykhuizen and Smith[4] and later studies on cold spray gas dynamics, the gas temperature decreases continuously during expansion through the converging–diverging nozzle and is related to the local Mach number by:

$$\frac{T_0}{T_g} = 1 + \frac{\gamma - 1}{2} M^2 \qquad (3.2.1.2)$$

where T_0 is the stagnation temperature, T_g is the local gas temperature, and M is the local Mach number. Rearranging gives:

$$T_g = \frac{T_0}{1 + \frac{\gamma - 1}{2} M^2} \qquad (3.2.1.3)$$

$$\frac{P_0}{P_g} = \left(1 + \frac{\gamma - 1}{2} M^2\right)^{\frac{\gamma}{\gamma - 1}} \qquad (3.2.1.4)$$

where P_0 is the stagnation pressure and P_g is the local gas pressure.

The local gas velocity can then be calculated from the definition of Mach number:

$$V_g = Ma \qquad (3.2.1.5)$$

where a is the local speed of sound. For an ideal gas, the speed of sound is given by:

$$a = \sqrt{\gamma R T_g} \qquad (3.2.1.6)$$

Substituting the above expression into the Mach number definition yields:

$$V_g = M\sqrt{\gamma R T_g} \qquad (3.2.1.7)$$

where R is the specific gas constant of the process gas. In addition, the local gas density was determined using the ideal-gas relationship:

$$\rho_g = \frac{P_g}{RT_g} \quad (3.2.1.8)$$

Therefore, the Mach number distribution obtained from the area–Mach number relationship was converted into the corresponding distributions of gas temperature, gas velocity and gas density along the nozzle axis.

These gas-flow properties were then introduced into the particle acceleration model. Since particle acceleration in cold spray is primarily governed by aerodynamic drag, the relative velocity between the gas and the particle provides the driving force for momentum transfer. Consequently, the local gas velocity V_g and gas density ρ_g obtained from the isentropic flow calculation serve as the input parameters for the drag-based particle momentum equation:

$$m\frac{dV_p}{dt} = C_D\frac{\pi}{8}\rho_g d^2(V_g - V_p)^2 \quad (3.2.1.9)$$

where V_p and V_g are the particle and gas velocities, respectively, m is the particle mass, ρ_g is the gas density, d is the particle diameter, and C_D is the drag coefficient. According to Champagne et al., this drag-based equation can be used to iteratively calculate the particle velocity through the nozzle when the gas velocity is known.

In the present thesis, this method was used to estimate the velocity of Ti64 particles with different particle diameters. For each particle diameter, the same gas-flow calculation was first performed based on the nozzle geometry and operating conditions. The particle velocity was then iteratively calculated along the nozzle using the drag relationship above. Since particle diameter appears explicitly in the drag term and also affects particle inertia through the particle mass, particles with different diameters are accelerated to different velocities under the same gas-flow conditions. Smaller particles are generally accelerated more efficiently by the gas flow, whereas larger particles have greater inertia and therefore reach lower velocities.

Therefore, the relationship between particle velocity and particle diameter was not treated as a single closed-form equation. Instead, following Champagne et al., the particle velocity was obtained by repeating the same iterative calculation for different Ti64 particle diameters. This provides an approximate analytical estimation of the particle velocity distribution as a function of particle size. It should be noted that the calculated values are theoretical estimations rather than direct experimental measurements, and the actual particle velocity may also be influenced by particle morphology, particle size distribution, injection position, boundary-layer effects, shock structures and gas–particle interaction.

Based on the estimated relationship between Ti64 particle diameter and in-flight velocity, the fraction of particles whose calculated velocity exceeds the critical deposition velocity of Ti64 was further evaluated using the measured particle size distribution. According to Ref. [5], the critical deposition velocity of Ti64 is approximately 1000 m/s under typical cold spray conditions. As shown in Fig. 28(c), only approximately 9% of the Ti64 powder, in terms of volume fraction, is predicted to achieve a velocity higher than this critical threshold under the present spraying conditions [5]. This relatively low proportion of effectively depositable particles is consistent with the experimentally observed low deposition efficiency during the initial deposition stage. It also supports the proposed selective deposition mechanism, in which only a limited fraction of particles can successfully bond to the substrate, while the remaining particles either rebound, erode the surface, or contribute to the formation of non-uniform open porous structures. Therefore, although the particle velocity calculation is a theoretical estimation rather than a direct experimental measurement, it provides quantitative support for the interpretation that the low initial deposition efficiency of Ti64 is closely associated with its relatively high critical deposition velocity (approximately 1000 m/s) and the particle-size-dependent acceleration behaviour.

3.2.3 Micro-CT analysis of the internal architecture

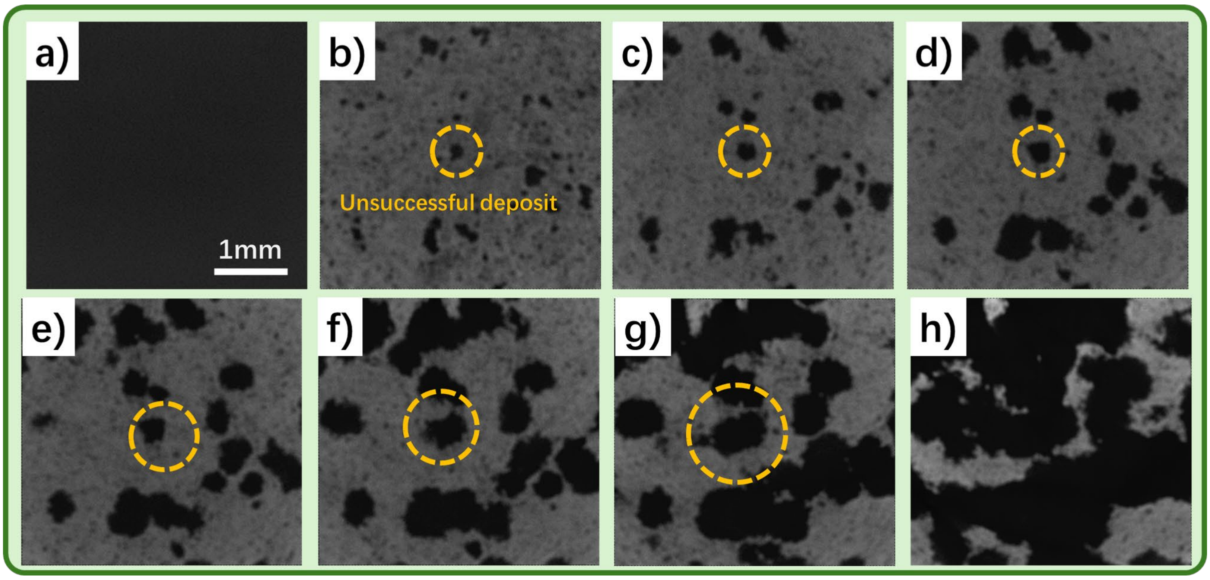

Figure. 29 Eight cross sections of the cellular structure from interface toward the top of the deposit

To further elucidate the internal architecture and evolutionary characteristics of the honeycomb like porous structure formed within the cold sprayed deposit, representative samples were examined using micro computed tomography and three dimensional morphological reconstruction. Fig. 29 presents successive tomographic cross sections from the substrate surface to the top of the deposited layer, with a height interval of 0.15 mm between adjacent images. By tracking these consecutive sections, the generation, evolution, and eventual stabilization of the porous structure can be directly visualized.

As shown in Fig. 29-a, the cross section corresponds to the substrate surface, where no apparent deposition has occurred and the material remains a dense metallic base. Fig. 29-b to Fig. 29-h illustrate the layer by layer evolution during deposition. In these images, the light gray regions represent successfully deposited Ti64 particles, whereas the black regions correspond to open pores where effective deposition did not occur. During the initial deposition stage shown in Fig. 29-b, Ti64 particles adhered only to localized areas of the substrate, while most regions remained uncovered or exhibited only sparse and random particle accumulation. This behavior highlights the pronounced spatial non-uniformity during the early stage of cold spray deposition. Owing to variations in particle velocity, impact angle, and local substrate geometry, only a fraction of particles underwent sufficient plastic deformation to bond with the substrate, whereas others rebounded upon impact and failed to form stable deposits.

The yellow circled region in Fig. 29-b clearly indicates an unsuccessful deposition zone. In this region, the absence of effective bonding resulted in the formation of a cavity with dimensions comparable to the particle diameter. As the deposit thickness increased, these regions were not filled or covered by subsequent layers but instead remained open, indicating that deposition defects formed during the early stage were inherited throughout subsequent deposition and ultimately evolved into through thickness pores.

From the evolution shown in Fig. 29-b to Fig. 29-h, the light gray deposited regions gradually increased and extended upward, demonstrating that previously deposited areas continuously captured incoming particles and grew outward. These regions served as the origins of the subsequent wall like structures. In contrast, the non-deposited regions maintained relatively fixed spatial positions and developed into vertically continuous pores extending from the substrate to the deposit surface. This observation suggests that once effective bonding fails to occur during the initial stage, subsequent particles are unable to accumulate in the same location due to unfavorable impact angles, geometric depressions, or local gas flow disturbances, resulting in persistently low deposition efficiency at those sites.

In addition, the morphology of the wall structures exhibited pronounced evolution with increasing deposit thickness. The walls were relatively wide near the substrate and gradually narrowed toward the top, forming a characteristic tapered geometry. This phenomenon can be attributed to the conical effect in cold spray deposition. As local height differences increase, the distribution of particle impact angles becomes more dispersed, leading to reduced deposition efficiency at protruding regions while redeposition in recessed regions becomes increasingly difficult. Consequently, the wall cross sectional width decreases with height.

This trend is clearly reflected in Fig. 29-b to Fig. 29-h, where the area fraction of the light gray regions progressively decreases, indicating increasingly non uniform growth with additional deposition layers. In particular, Fig. 29-b to Fig. 29-h show that the wall tops approach partial closure, while the non deposited regions evolve into slender through pores. These observations demonstrate that the honeycomb structure formed during cold spray deposition is not a static geometry but a dynamically evolving system driven by early stage deposition non-uniformity.

Longitudinal tracking of the pores further reveals that the black regions maintain nearly identical positions across different height sections, indicating continuous three dimensional connectivity. Once a region fails to form a dense deposit at the initial stage, it remains open along the deposition direction and ultimately penetrates the entire thickness. This feature is further confirmed by three dimensional reconstruction, which shows continuous pore channels interwoven with adjacent wall structures to form a network like honeycomb morphology.

From a macroscopic perspective, the resulting dense cellular hybrid structure exhibits potential functional advantages. The dense wall regions provide mechanical support and bonding strength, while the open cell channels enable subsequent functionalization such as infiltration, surface modification, or fluid transport for heat transfer. However, the formation process remains largely stochastic, with limited control over pore size, position, and connectivity.

Overall, the tomographic results in Fig. 29 clearly reveal the formation mechanism of the honeycomb like porous structure during cold spray deposition. Early stage non uniform deposition determines the spatial distribution of pores, while increasing deposition layers amplify this effect, ultimately producing a multiscale honeycomb structure composed of cells and walls. With further process optimization and multiscale characterization, such structures show promise for applications in heat exchange, filtration, sensing, and lightweight structural components, providing new insights into the controllable fabrication of porous materials via solid state additive manufacturing.

3.3 Analysis of single-particle velocity dispersion and Its mechanism

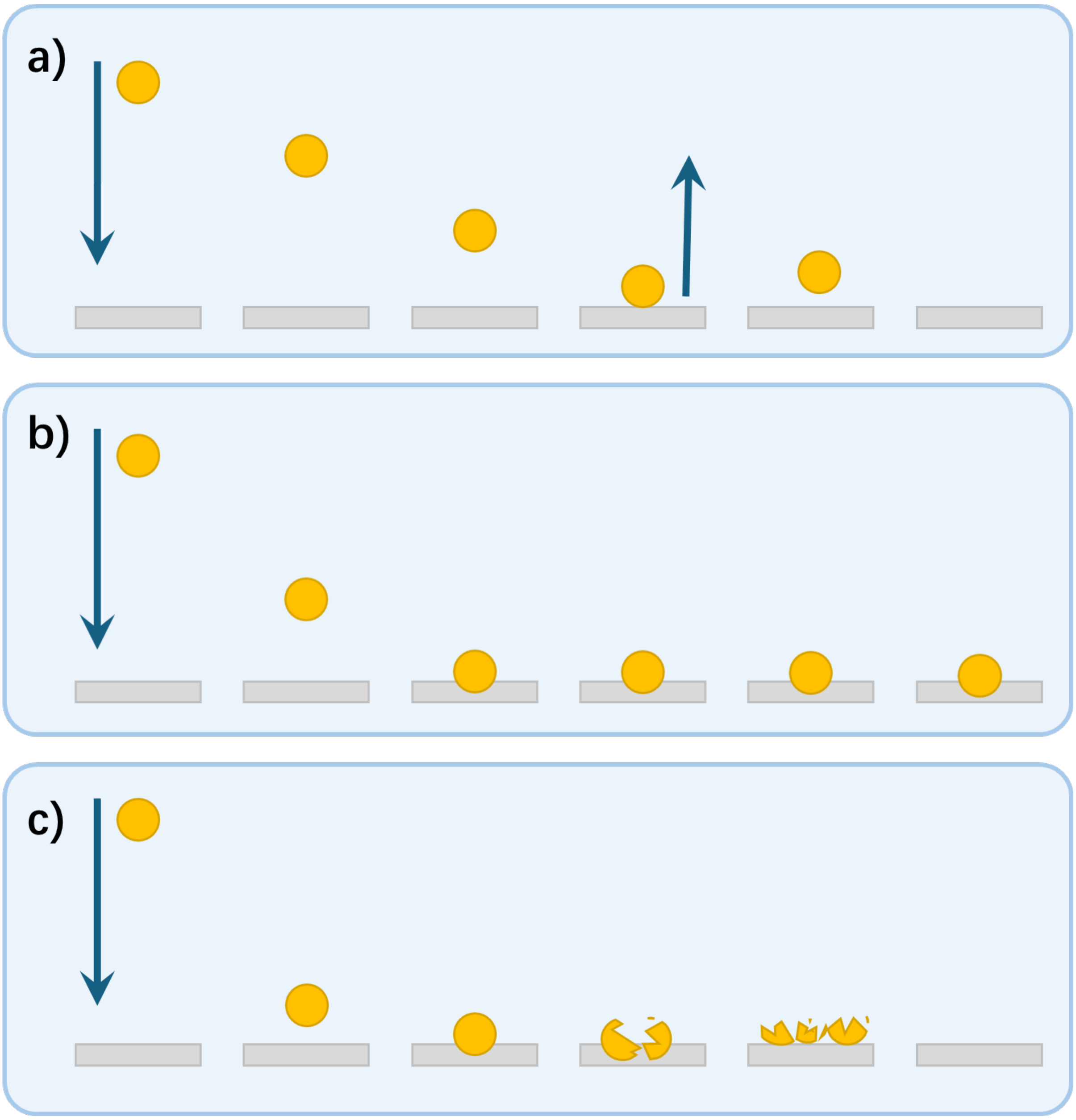

Figure. 30 Schematically illustrates the typical single particle responses of Ti 6Al 4V particles impacting an Al6082 substrate at different impact velocities during the cold spray process.

As shown in Fig. 30, the yellow circles represent Ti64 particles and the gray rectangles denote the Al6082 substrate. The three sub-figures illustrate particle–substrate interactions occurring at low (below critical), medium (near critical), and high (above critical) impact velocities. These regimes do not correspond to different spraying conditions. Instead, they arise naturally within a single cold spray process due to the statistical dispersion of particle velocities generated by gas–solid two-phase flow dynamics.

Although macroscopic spray parameters such as gas pressure, temperature, and nozzle geometry remain constant, the exit velocity of individual particles is not unique but follows a broad distribution. Variations in particle size, morphology, density, and surface condition lead to different acceleration responses under the same gas flow. In addition, strong radial and axial gradients exist within the de Laval nozzle, resulting in higher velocities in the core region and lower velocities near the nozzle wall. Differences in particle inertia further prevent some particles from fully following gas acceleration. Consequently, particles reach the substrate with velocities spanning from below the critical velocity to well above it, giving rise to the three interaction regimes illustrated in the figure.

When the particle velocity is below the critical velocity, the kinetic energy of Ti64 particles is insufficient to trigger significant interfacial plastic deformation. The contact time is extremely short, and the normal and shear stresses generated at the interface are inadequate to rupture the surface oxide or nitride layer or to induce substantial plastic flow in the Al6082 substrate. Most of the impact energy is therefore dissipated through elastic recovery and limited local plastic deformation, preventing the formation of intimate metal–metal contact. As a result, particles rebound from the surface. This regime reduces deposition efficiency and contributes to initial deposition non-uniformity.

As the impact velocity approaches and slightly exceeds the critical velocity, the particle–substrate system enters the effective deposition window. Both the Ti64 particle and the Al6082 substrate undergo high strain-rate plastic deformation in the interfacial region. The relatively softer substrate experiences localized plastic flow, which promotes interfacial conformity and mechanical interlocking. Simultaneously, severe plastic deformation of the particle leads to fracture or delamination of the brittle surface oxide or nitride layer, exposing fresh metallic surfaces. Intimate metal–metal contact is therefore established within an extremely short timescale, resulting in stable solid-state bonding. This velocity range represents the optimal deposition regime in cold spray.

When the impact velocity significantly exceeds the optimal deposition range, the interaction transitions from deformation-dominated bonding to damage-dominated behavior. Ti64 exhibits limited plastic deformability at room temperature and is prone to strain localization under ultra-high strain-rate loading. Moreover, the use of nitrogen as the propellant gas may lead to surface nitrogen enrichment or the presence of a TiN-rich brittle shell on the particle surface. Under the extreme stress gradients generated during high-velocity impact, this brittle surface layer readily cracks, and the cracks can rapidly propagate into the particle interior. The particle consequently undergoes fragmentation or pulverization, as illustrated in the figure. Although such impacts may generate high local contact pressures, the fragmented material cannot form a continuous and stable bonding interface and may instead produce debris, cause secondary erosion, and degrade coating integrity.

Overall, the three behaviors shown in Fig. 30 represent the natural manifestation of particle velocity dispersion relative to the critical velocity during cold spray deposition. Rebounding particles below the critical velocity, effectively bonded particles near the critical velocity, and fragmented particles above the optimal velocity range coexist within a single spraying process. Their relative proportions collectively determine deposition efficiency, coating density, and microstructural non-uniformity, indicating the existence of a distinct and relatively narrow optimal deposition velocity window for the Ti64/Al6082 system.

3.4 Mechanical properties

3.4.1 Nanoindentation characterization of regional mechanical properties

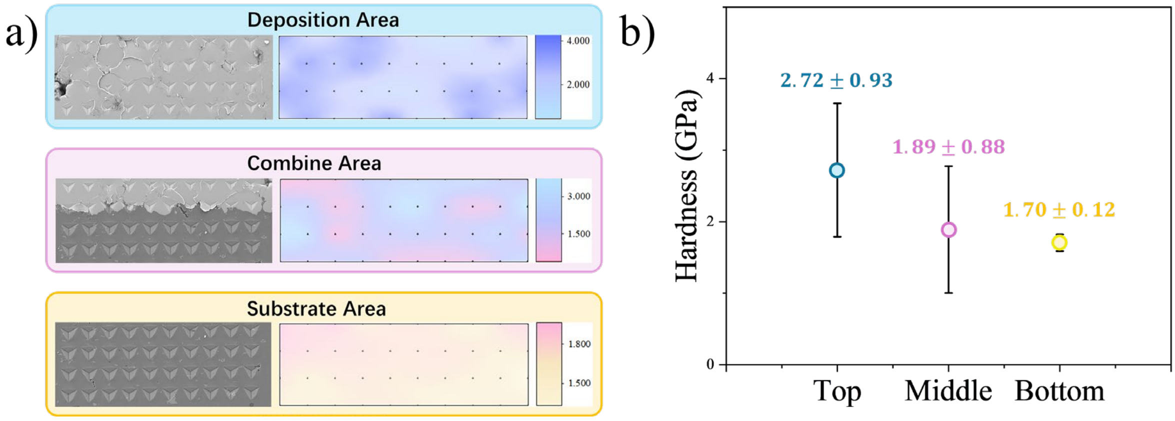

Figure. 31 a) Nanoindentation SEM Images and Hardness Distribution Maps, b) Average hardness values across different regions

Fig. 31-a presents the scanning electron microscopy images of nanoindentation arrays and the corresponding hardness contour maps obtained from nanoindentation testing performed on a cold sprayed Ti 6Al 4V porous coating at three representative locations. These locations correspond to the coating deposition region, the coating substrate bonding region, and the substrate region unaffected by spraying, representing typical areas that experienced different mechanical loading histories and microstructural evolution during the cold spray process. By arranging regular indentation arrays within each region and spatially mapping the measured hardness values, the distribution characteristics and degree of mechanical non-uniformity at different locations can be directly visualized.

The statistical results shown in Fig. 31-b indicate pronounced differences in the average nanoindentation hardness among the three regions. The coating deposition region exhibits the highest average hardness of 2.72 GPa, followed by the coating substrate bonding region with an average hardness of 1.89 GPa, while the substrate region shows the lowest average hardness of 1.70 GPa. These results demonstrate that the cold spray deposition process not only introduces significant mechanical strengthening within the coating itself but also induces a measurable mechanical response in the substrate material adjacent to the bonding interface.

To evaluate the repeatability of the experimental results, each sample shown in Fig. 32-b was tested six times under the same experimental conditions. The data presented in Fig. 32-b are expressed as the mean values of the six repeated measurements, and the error bars represent the corresponding standard deviation. The observed scatter mainly arises from the inherent spatial non-uniformity of the cold-sprayed porous surfaces, as well as minor variations during sample preparation and measurement. Despite these variations, the repeated measurements show consistent trends, indicating that the experimental results are repeatable and that the conclusions drawn from Fig. 32-b are reliable.

Further examination of the hardness contour maps on the right side of Fig. 31-a reveals evident nanoscale mechanical heterogeneity in both the coating deposition region and the coating substrate bonding region. This heterogeneity is manifested by continuous color variations and localized high and low hardness zones, indicating that even within the same region, different microdomains experienced distinct degrees of plastic deformation and microstructural modification. In contrast, the substrate region exhibits a highly uniform hardness distribution, with minimal color variation in the contour map, suggesting that its mechanical properties largely retain the intrinsic characteristics of the original material.

For the coating deposition region, the observed hardness heterogeneity primarily arises from two factors. First, the porous cold sprayed deposit inherently contains structural defects such as particle boundaries, partially closed micropores, and localized microcracks. In the vicinity of these defects, the effective load bearing area is reduced and stress concentration is intensified, facilitating localized plastic deformation during indentation and resulting in relatively lower measured hardness. These low hardness regions typically appear as scattered low value zones in the contour maps and correspond well with pores or interfacial features observed in the SEM images.

Second, the original Ti 6Al 4V powder particles undergo extreme plastic deformation during high velocity cold spray impact. Upon collision with the substrate or previously deposited layers, the particles experience very high strain, strain rate, and transient temperature rise, leading to the formation of pronounced heterogeneous microstructures within the particles. Variations in deformation degree and dynamic recovery behavior both among different particles and within individual particles introduce microscale hardness fluctuations. As a result, localized hardness variations can also occur in regions distant from visible porosity.

In comparison, the coating substrate bonding region exhibits the most pronounced hardness non-uniformity among the three regions. This region corresponds to the initial stage of cold spray deposition, where particles first undergo high velocity impact and interaction with the substrate. During this process, Ti 6Al 4V particles experience severe plastic deformation and mechanical interlocking with the substrate surface, forming a stable bonding interface. Simultaneously, the high velocity impacts introduce significant work hardening in the near surface region of the substrate, resulting in hardness values markedly higher than those of the unaffected substrate. However, due to spatial variations in particle impact energy, the degree of work hardening differs substantially at the microscale, leading to a highly complex and dispersed hardness distribution within the bonding region.

As the depth below the substrate surface increases, the plastic deformation and work hardening effects induced by particle impact gradually diminish. Upon entering the substrate region, the material is essentially unaffected by direct high velocity particle impact, and its microstructure and mechanical properties remain characteristic of the original Al 6082 substrate. Consequently, the substrate region exhibits not only the lowest average hardness but also the most uniform hardness distribution, with negligible spatial variation.

In summary, the nanoindentation results presented in Fig. 31 clearly reveal the spatial gradient and heterogeneity of mechanical properties within the cold sprayed Ti 6Al 4V porous coating system. Both the deposition region and the bonding region exhibit pronounced nanoscale hardness fluctuations due to intense and non uniform plastic deformation, whereas the substrate region largely preserves a uniform mechanical response. This through thickness evolution of mechanical properties provides important experimental evidence for understanding the formation mechanisms and service performance of cold sprayed porous structures.

3.4.2 Tension test

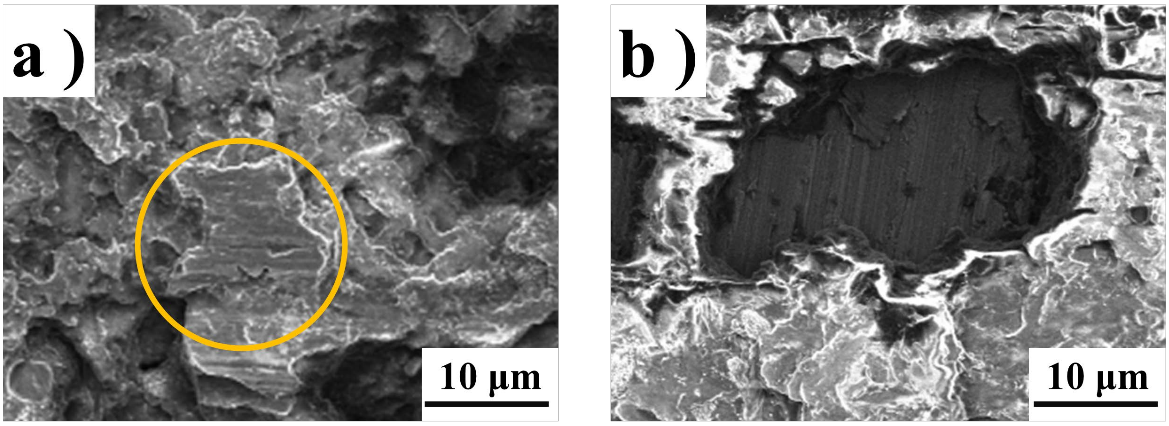

Figure. 32 SEM image of Ti64 coating fracture surface

The tensile fracture surface of the cold sprayed Ti64 coating exhibits pronounced particle scale heterogeneity. The fracture surface is globally rough and undulated, consisting of clearly discernible platelet like units assembled together, rather than the uniform dimple morphology typically observed in dense wrought materials. This particle block dominated fracture morphology indicates that failure is not governed by continuous plastic deformation of a homogeneous matrix, but is jointly controlled by the deposited particle structure and interfacial characteristics. Such behavior represents a typical heterogeneous fracture mode of cold sprayed deposits.

As shown in Fig. 32-a, a distinct flat fracture platform is observed, whose fracture normal is nearly parallel to the tensile loading direction. This platform is clearly circled in the image and exhibits local step like markings and tear ridges. The geometric orientation of this flat region indicates that crack propagation in this area occurred approximately perpendicular to the loading axis, producing a fracture plane parallel to the applied tensile direction. These features are not associated with particle pull out pits, but instead correspond to characteristic quasi cleavage facets. The presence of such a well developed fracture platform suggests that crack propagation locally transitioned from interfacial separation to rapid transgranular propagation within the particle interior. Therefore, tensile failure was not dominated by a single interfacial debonding mechanism, but involved a clear transition from interfacial failure to brittle fracture inside the particles, reflecting a distinctly brittle dominated failure mode in the later stage of crack growth.

Dark voids and smooth edged depressions are still present on other regions of the fracture surface, exhibiting morphologies consistent with particle pull out features. These features provide direct evidence of particle particle interfacial debonding and confirm that deposition interfaces remain preferred crack initiation sites. Moreover, as shown in Fig. 32-b, a large cavity corresponding to coating substrate separation can be observed. The exposed substrate surface inside the cavity appears relatively smooth and exhibits limited plastic deformation traces, indicating weak metallurgical bonding at the coating substrate interface. This feature further confirms that the coating substrate interface acts as a structural weak zone under tensile loading.

The tensile test results indicate that the bonding strength of the coating is only 10.19 MPa, which is significantly lower than the intrinsic tensile strength of dense wrought Ti64. This low macroscopic strength directly reflects limited interfacial bonding capability and is consistent with the extensive interfacial debonding features observed on the fracture surface, particularly the coating substrate separation shown in Fig. 32-b. However, unlike a purely interfacial separation fracture, the presence of large quasi cleavage facets in Fig. 32-a demonstrates that cracks penetrated the particle interior during the later stages of crack propagation.

In addition, as shown in Fig. 32-b localized pore clusters and incompletely filled cavities are observed on the fracture surface. These regions represent structural weak zones formed during deposition and act as sites of significant stress concentration under tensile loading, thereby serving as preferential crack initiation locations. Cracks initially nucleate at interfaces adjacent to pores and propagate along interfacial paths. Once the crack length and stress intensity reach critical values, the crack path deflects into the particle interior. Under conditions of severe work hardening and limited plastic deformation capacity, quasi cleavage dominated rapid crack propagation is triggered, leading to the formation of large scale flat fracture platforms such as that shown in Fig. 32-b.

Although the overall fracture behavior is quasi brittle in nature, fine shear steps and layered flow traces can still be identified on portions of the particle surfaces, indicating that the particles experienced intense plastic deformation during deposition. However, the high dislocation density and pronounced work hardening induced by this pre deformation substantially reduce the capacity for plastic energy dissipation during subsequent tensile loading, resulting in low macroscopic ductility. Previous studies have shown that cold sprayed Ti64 deposits often exhibit high microhardness but limited elongation, with fracture controlled by the combined action of interfacial failure and transgranular brittle fracture, which is consistent with the behavior observed in the present study.

The formation of weak interfacial bonding is closely related to the processing environment. When nitrogen is used as the propellant gas, nitrogen rich or oxide enriched layers may form on the surface of Ti64 particles during flight, reducing effective plastic flow and limiting the formation of true metallurgical contact at the interface. Furthermore, the extremely short timescale of cold spray deposition restricts interfacial diffusion and recrystallization processes, causing the deposition interface, including the coating substrate interface observed in Fig. 32-b, to act as a crack initiation source. Meanwhile, severe work hardening and potential metastable microstructures within the particle interior provide favorable conditions for subsequent quasi cleavage propagation.

In summary, the fracture surface reflects a characteristic tensile failure mode of as deposited cold sprayed Ti64 coatings. Cracks initiate at pores and weakly bonded interfaces, including the coating substrate interface, propagate along interfacial paths, and subsequently deflect into the particle interior under stress concentration and limited plastic reserve, where rapid quasi cleavage dominated propagation occurs, forming flat fracture platforms parallel to the loading direction as shown in Fig. 21-a. Only limited shear deformation takes place within the particles, ultimately resulting in a quasi brittle fracture governed by the coupled effects of interfacial failure and transgranular brittle fracture. This mechanism provides a consistent explanation for the observed combination of low bonding strength (10.19 MPa) and severely limited ductility at the macroscopic scale.

3.4 Summary

This chapter systematically investigates the formation mechanism, evolutionary behavior, and structure property relationships of honeycomb like porous Ti 6Al 4V structures fabricated by cold spray deposition. The main conclusions are summarized as follows.

(1) Even under constant macroscopic spraying parameters, the deposition process exhibits pronounced spatial non-uniformity. This non-uniformity originates from the interaction

between gas solid two-phase flow characteristics and the high strain rate plastic response of particles. It represents the intrinsic physical basis for porous structure formation rather than being caused by process fluctuations.

(2) The cold sprayed deposit exhibits a typical open honeycomb morphology composed of cellular pores on the order of several hundred micrometers and wall like skeletons growing along the deposition direction, forming a highly interconnected three dimensional porous network. This structure is not generated through templating or post processing but evolves spontaneously during the deposition process.

(3) Cross sectional analysis and micro computed tomography three dimensional reconstruction demonstrate that effective bonding occurs only in localized regions during the initial deposition stage. Undeposited regions are continuously inherited and amplified during subsequent deposition, ultimately evolving into open channels penetrating the entire deposit thickness, reflecting a pronounced inheritance effect of the initial deposition state. The wall structures gradually taper from the substrate toward the top of the deposit, exhibiting a conical geometry, which indicates that the honeycomb architecture represents a thickness limited and dynamically evolving non steady state system.

(4) Single particle dynamic analysis reveals that particle velocity dispersion is the key factor governing deposition non-uniformity. Under identical process conditions, particle rebound, effective deposition, and high velocity particle damage coexist. The combined effect of these behaviors determines deposition efficiency and pore formation pathways, constituting the fundamental kinetic mechanism underlying porous structure evolution.

(5) Mechanical property evaluation shows that the hardness of both the deposition region and the bonding region is significantly higher than that of the substrate, while pronounced nanoscale heterogeneity exists within the system. During tensile fracture, cracks preferentially initiate at pores and weak interfaces and propagate in a quasi brittle mode dominated by quasi cleavage, indicating that the pore structure plays a governing role in the macroscopic mechanical response.

In summary, this chapter establishes the intrinsic relationship among deposition non-uniformity, pore structure evolution, and mechanical response, providing systematic experimental evidence and theoretical support for mechanistic understanding and controllable design of porous structures in cold spray solid state additive manufacturing.

Chapter 4 Study on boiling heat transfer performance of porous Ti64 surfaces produced by cold spray

In the previous chapter, the formation mechanism and microstructural evolution of the surface open pore structure in cold sprayed Ti64 were systematically elucidated. Building upon this foundation, the present chapter further considers this structure as a functional surface system and introduces pool boiling heat transfer as the platform for performance evaluation. If the previous chapter primarily addressed the question of how the structure forms, the present chapter focuses on whether the structure is effective and how it functions. By establishing a stable and reproducible pool boiling experimental system, this chapter aims to construct the relationship between structural characteristics and functional performance of the cold sprayed porous structure, and to provide experimental evidence for its potential engineering applications.

Boiling heat transfer is an interfacial heat transfer process that is highly sensitive to surface microstructures. Its enhancement mechanisms are closely related to bubble nucleation, growth, departure, and the evolution of the critical heat flux, abbreviated as CHF. Previous studies have shown that surface pore structures and roughness features can significantly reduce the nucleation superheat, increase the density of nucleation sites, and delay surface dryout and heat transfer instability through regulation of gas liquid interfacial behavior. However, variations in pore size, connectivity, and the thermal conductivity of the material can strongly influence the actual heat transfer performance. Therefore, it is necessary to systematically verify the heat transfer response of the cold sprayed Ti64 surface open pore structure under realistic boiling conditions.

To achieve these objectives, a standardized pool boiling experimental apparatus was first constructed. Under saturated boiling conditions, the boiling curves, heat transfer coefficients, and critical heat flux of the cold sprayed Ti64 surfaces were measured and compared with those of a smooth substrate surface. Subsequently, three dimensional surface morphology reconstruction, surface roughness characterization, and wettability measurements were performed to analyze the structural origins of the observed heat transfer enhancement. In addition, high speed imaging techniques were employed to conduct in situ observation of bubble behavior under different heat flux conditions. This approach enables the identification of the roles played by the pore structure in stabilizing bubble nucleation, suppressing lateral bubble coalescence, and promoting the formation of liquid replenishment pathways.

Overall, this chapter systematically evaluates the functional performance of the cold sprayed Ti64 surface open pore structure in pool boiling heat transfer through an integrated research framework that combines experimental verification, structural characterization, bubble dynamics analysis, and heat transfer mechanism discussion. The results provide both experimental foundations and mechanistic insights for subsequent structural optimization and for the extension of this approach to other material systems.

Based on the above research background, the main objectives of this chapter are as follows.

- To establish a stable and reliable pool boiling experimental platform for the systematic evaluation of the boiling heat transfer performance of the cold sprayed Ti64 surface open pore structure.
- To assess the heat transfer enhancement effect of the porous structure by comparing boiling curves, heat transfer coefficients, and critical heat flux with those of a smooth substrate surface.
- To establish correlations between surface structural characteristics and heat transfer performance through three dimensional morphology reconstruction, surface roughness characterization, and wettability measurements.
- To analyze bubble nucleation, growth, and departure behavior using high speed imaging techniques, and to elucidate the role of the porous structure in regulating bubble dynamics.

4.1 Experimental setup and testing methods

4.1.1 Raw material and cold spray process

The experimental material employed in this section is also Ti64 powder, consistent with the material used in Section 2.1. The cold spraying equipment utilized in the experiments is likewise identical.

With reference to the processing parameters reported in previous studies and considering the maximum capacity of the laboratory cold spray system, a porous surface was created on an aluminium substrate by adjusting three main parameters: TS, PFR and the number of layers. The specific experimental parameters are listed in Table 3.

Table. 3 Experimental parameters in cold spray process.

No.	Label	TS (mm/min)	PFR (g/s)	Number of Layers
1	2000-27-4	2000	0.27	4
2	2000-27-8	2000	0.27	8
3	2800-51-2	2800	0.51	2
4	2800-51-3	2800	0.51	3

5	2800-51-4	2800	0.51	4

4.1.2 Microstructure characterization

Scanning electron microscopy (SEM, Zeiss Ultra) was used to analyse the morphology of the boiling heat exchanger surfaces prepared by cold spraying. 3D model reconstruction of the surface deposits was facilitated by a Nikon XTH225 ST X-ray CT (Computed Tomography) system and the surface roughness was measured using a Filmetrics Profilm3D optical profilometer. The working fluid interaction with the test surfaces was characterized with a Theta Flow Optical Tensiometer (Biolin Scientific).

4.1.3 Pool boiling test facility and experimental procedures

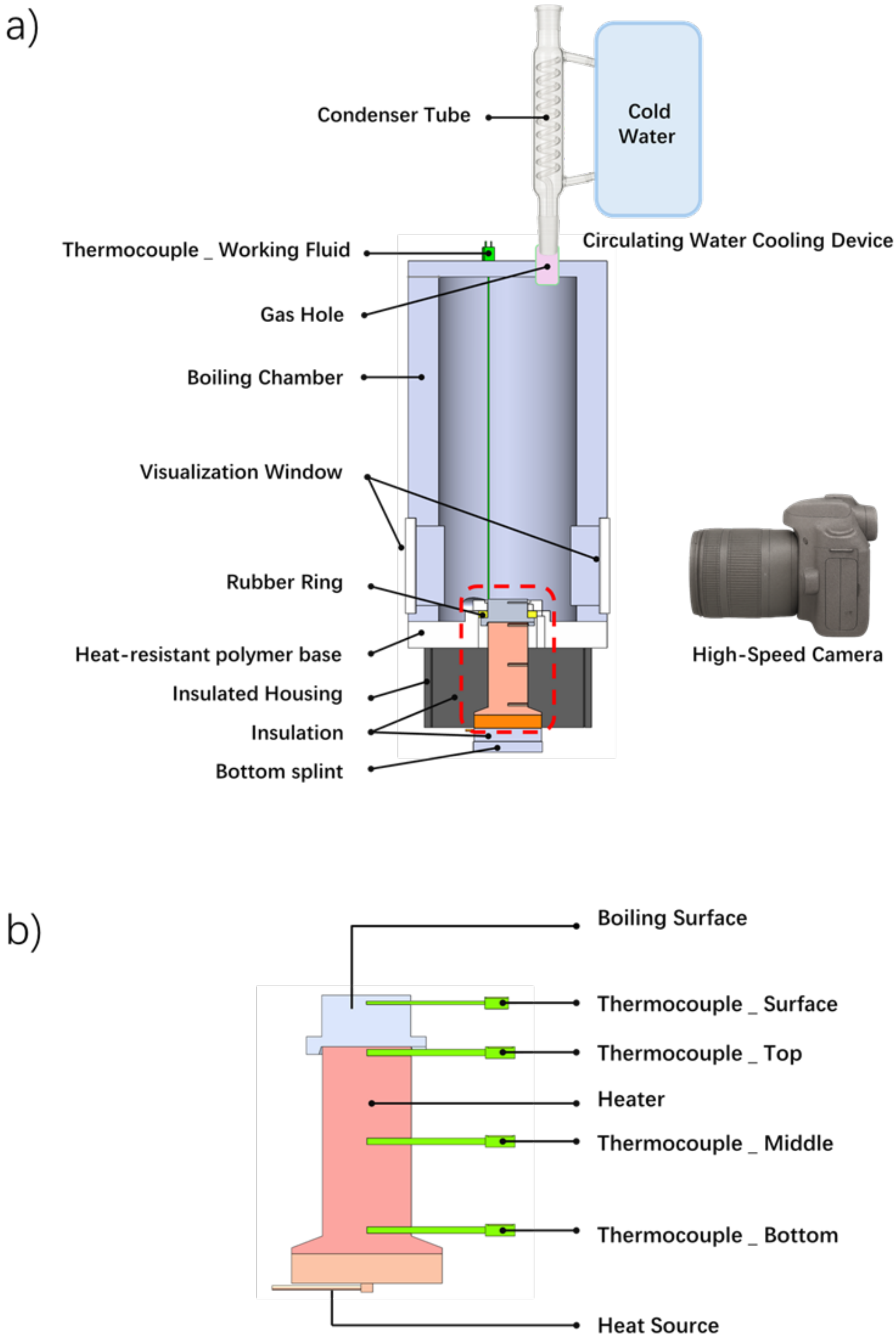

Figure. 33 a) Cross-sectional schematic of the pool boiling apparatus and b) Enlarged view of the heater assembly

Fig. 33-a shows a cross-sectional schematic of the pool boiling apparatus. It consists of boiling chamber, filled with ethanol as the working fluid, with a high-temperature-resistant PEEK mounting fixed at the bottom using M4 screws. The chamber is a

cylindrical container with an inner diameter of 5 cm and a height of 12 cm. A gas outlet at the top connects the chamber to the water-cooled re-flux condenser. During testing, the evaporated working fluid escapes through this outlet into the condenser, where it gets liquefied and returned to the chamber, thereby minimizing liquid loss during the boiling experiments. It also maintains the atmospheric pressure throughout the test duration. Two cartridge heaters (120W each) were inserted horizontally at the base of the boiling chamber to heat up and maintain the bulk liquid at its saturation temperature. Power to these heaters was controlled through a PID controller. A T-type sheathed thermocouple inserted from the top of the chamber was used to monitor the bulk liquid temperature adjacent to the boiling surface during boiling. This thermocouple signal was fed to the PID controller to automatically regulate the bulk liquid heating, maintaining its constant temperature. Four transparent glass windows (2.5 cm × 3 cm) were attached on opposite sides of the chamber near to its base to provide optical access of the boiling phenomenon. The boiling dynamics were captured using videographic camera system, which included high speed camera (HotShot: HS1700CC), zoom lens (SIGMA 105 mm F2.8 DG DN Macro), and a diffused white light source. Two light sources were employed during recording to facilitate more light into the boiling chamber, enabling better quality of the recorded images.

Fig. 33-b presents an enlarged schematic of the heating section. It comprised of assembly of the boiling substrate, copper block, and heater. The boiling surface, with dimensions of 1.5 × 1.5 cm^2, prepared with test coatings as required was mounted on the copper block of the same cross-sectional dimension. High thermal conductive paste was applied between the copper block and the boiling substrate to minimize thermal contact resistance. At the bottom of the block, square ceramic heater (500W) was fixed using high-temperature thermal pad. A T-type sheathed (0.5 mm dia.) thermocouple was inserted 1 mm beneath the boiling surface at the depth of 7.5 mm to approximately measure the surface temperature. To measure the heat flux through the heating section, three T-type sheathed (1 mm dia.) thermocouples were inserted into three equally spaced (15 mm) holes along the heated bar length. The holes were drilled at the depth of 7.5 mm i.e., till the central axis of the block. To reduce heat losses from the heating section, the copper block and the heater was insulated on all sides using insulating pads contained in the 3D printed box. This entire heating section was clamped to the base PEEK mounting that

securely held this assembly. The sufficient clamping pressure was ensured to minimize overall thermal contact resistance. The base mounting was designed in such a way that the boiling substrate would slightly protrude above the top surface of the mounting. In addition, shoulder cut was provided in the base mounting around the boiling substrate area to fill the leakproof silicon epoxy, ensuring test fluid does not leak during testing.

4.1.4 Pool boiling test procedures

The pool boiling experiments were performed on bare and cold-sprayed surfaces with ethanol as the working fluid under atmospheric pressure. For each test, the fluid was poured into the boiling chamber and degassed for one hour by turning on the bulk heater and ceramic heater. During this time, the test fluid was maintained at its saturation temperature (78°C) and rigorous boiling was allowed on the surface. Subsequently, the ceramic heater was turned off so that bubble nucleation ceases on the boiling surface. Now, the heater power to the ceramic heater was increased gradually in finite steps and for each heater power, temperatures from all the thermocouples and bubble dynamics were recorded at 5 samples/s and 4000 fps respectively. Sufficient time was allowed to ensure steady-state conditions, before data recording commenced. The test was terminated at the heat power when a transition to film boiling was observed, indicating the occurrence of boiling crisis, i.e., CHF, identified through the rapid and monotonous rise in the surface temperature. In this study, all measurements were repeated three times for each sample to ensure reproducibility of the results.

4.2 Surface characteristic analysis

4.2.1 Surface properties

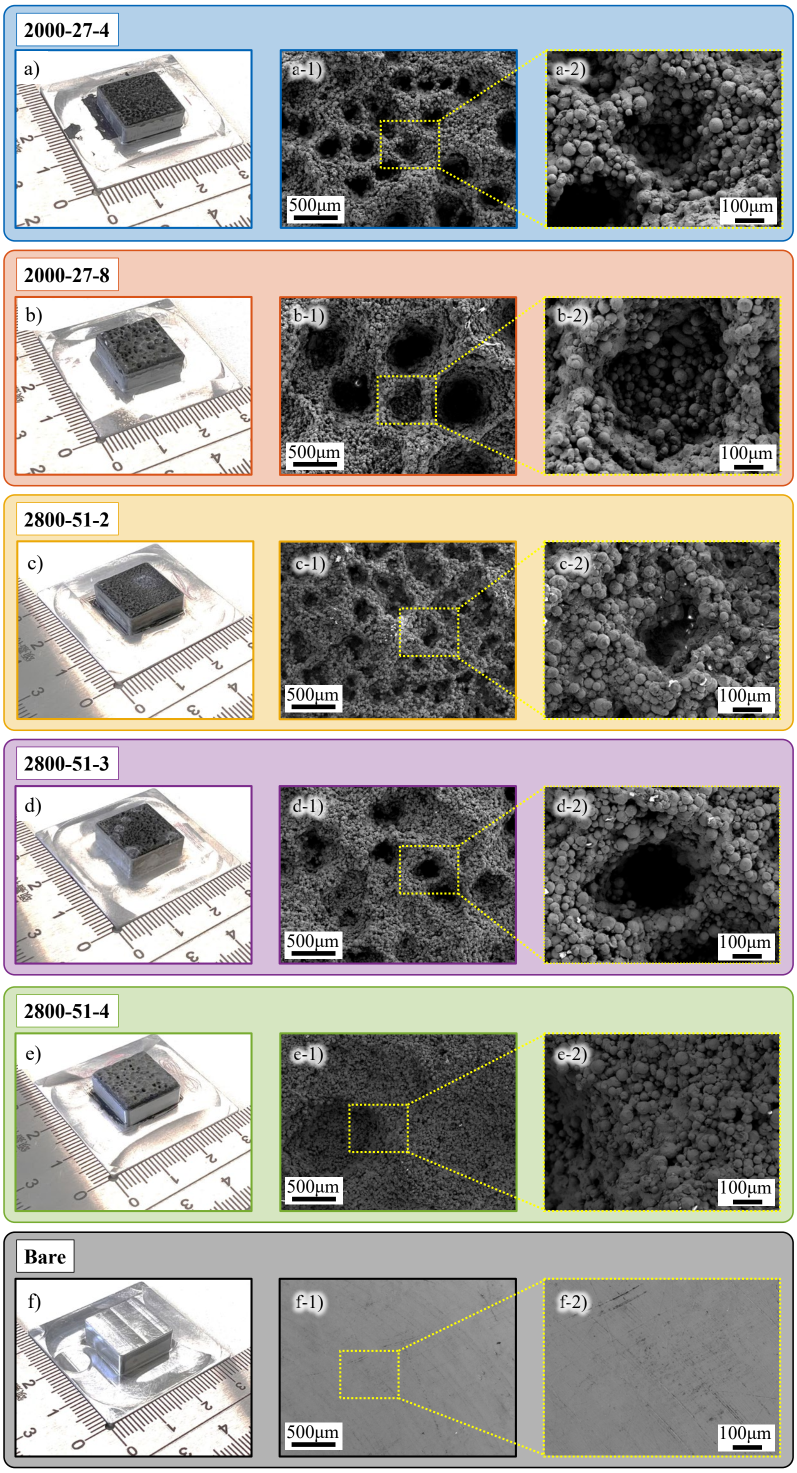

Figure. 34 Images of the surface morphology of boiling samples fabricated via cold spraying for this study. Photographs of the boiling samples (a,b,c,d,e,f). Scanning

electron microscopy (SEM) images of the sample surfaces (a-1,b-1,c-1,d-1,e-1,f-1). Magnified view of the region highlighted by yellow dashed lines in panel (a-2,b-2,c-2,d-2,e-2,f-2).

Figures from 34-a to 34-f shows macro-photographs of the boiling surface prepared by cold spraying and the bare boiling surface. Additionally, scanning electron microscope images are provided to illustrate the effect of different spraying parameters on the pore characteristics of the coatings (Figures from 34-a-1 to 34-f-1 and from 34-a-2 to 34-f-2). As a reference, the bare surface (Figures 34-f-1 and 34-f-2) is almost flat with only a few minor scratches, which were produced during the machining process. In contrast, the boiling surfaces prepared by cold spraying showed a pronounced 200 μm – 500 μm wide cavity type structure, in which the size and distribution of the pits were significantly influenced by the fabrication parameters. Comparing Sample 2000-27-4 and Sample 2800-51-4, it is clear that decreasing the powder feed rate leads to a significant increase in the number of cavities on the surface. This suggests that a higher powder feed rate results in more titanium powder being deposited, with less cavities being formed on the coating surface. Comparing Samples 2800-51-2, 2800-51-3, and 2800-51-4 indicates that as the number of layers deposited increases, the cavities on the surface of the samples become progressively larger (see Table 4). Such a pattern can also be found by comparing Samples 2000-27-4 and 2000-27-8. The phenomenon of increasing cavity size with the number of deposited layers is suspected to be due to the formation of thicker coatings by multilayer deposition, which makes the lip regions of the cavities protrude more from the surface.

Table. 4 Measured properties of the samples.

Sample	2000-27-4	2000-27-8	2800-51-2	2800-51-3	2800-51-4	Bare
Thickness (mm)	1.59	2.50	0.55	0.61	1.38	-
Roughness (μm)	41.3	30.0	45.7	62.44	36.9	0.18

Average cavity size (μm)	312	577	207	388	1117	-

From the point of view of boiling heat transfer, this textured surface coating prepared by cold spraying is very beneficial. Firstly, the strong mechanical bonding of the coating and the substrate ensures the longevity and low thermal contact resistance of this boiling surface. Secondly, the small cavity-shaped surface features are ideal locations for nucleation of vapour bubbles, and the more nucleation centres the better. Furthermore, bubbles which nucleate in neighbouring cavities have a separating medium between them, which should mitigate lateral bubble coalescence.

4.2.2 Roughness

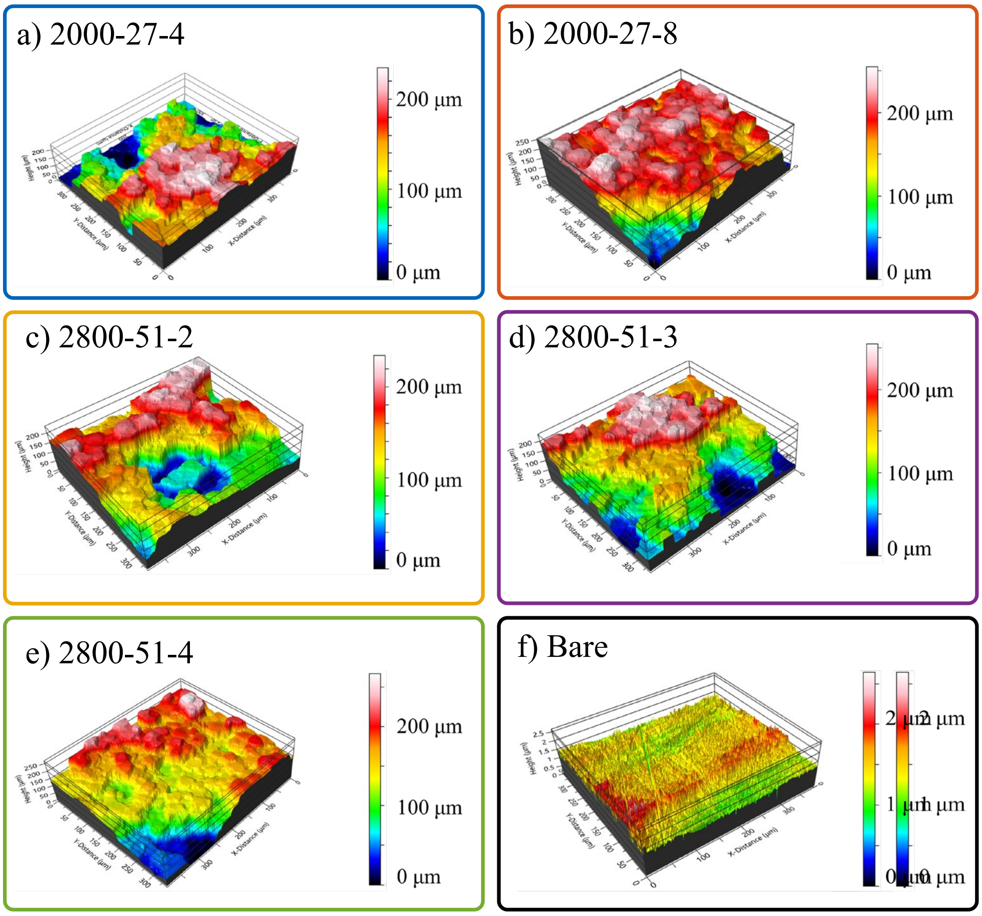

Figure. 35 White Light Interferometry images of tested boiling surfaces

Fig. 35 also shows the roughness (Ra) of the prepared porous surfaces with different cold spraying parameters. The roughness of the cold sprayed surfaces is generally two orders of magnitude higher than that of the bare surface, which is 0.18 μm, and reaches up to 62.44 μm (2800-51-3). This result is corroborated by the white light interferometer (WHI) 3D morphology in Fig. 35 : the bare surface is generally smooth with small scratches with a maximum undulation range of 0–2.5 μm. Conversely, the peaks and valleys of the surface prepared by cold spraying can reach hundreds of micrometres, showing wave-like undulation surface morphology.

Specifically, as shown in Fig. 35, the number of layers has a significant effect on the surface morphology. For example, comparing Sample 2000-27-8 (Ra = 30.0 μm) with 8 layers and Sample 2800-51-2 (Ra = 45.7 μm) with only 2 layers, it can be seen that the latter sample has more peaks and valleys on the surface, resulting in a higher roughness. Similarly, Sample 2800-51-3 (multi-layer spraying) reaches a maximum Ra value of 62.44 μm, which indicates that the localised build-up is more pronounced during the multi-layer spraying process, ultimately leading to a significant increase in the difference in surface height distribution.

Overall, the cold spraying process generates a large number of irregular bumpy structures on the substrate surface, which significantly increases the surface roughness and the effective heat transfer area; in contrast, the bare surface is relatively smooth. Combining the roughness data in Table.4 with the 3D morphology in Fig. 35, the effect of the cold spraying preparation process on the surface topography can be more intuitively understood.

In addition to the increase in surface roughness, the cold spraying process also produces a complex surface morphology consisting of partially bonded particles, open pores and cavity-like surface features. Although the average roughness parameter provides a useful quantitative description of the overall surface profile, it does not fully capture the influence of these microstructural features on boiling heat transfer behaviour. The cavity-like structures formed during deposition may serve as stable vapour entrapment sites and provide a high density of potential nucleation sites during boiling. Furthermore, the irregular peaks, valleys and porous regions generated by the deposition process increase the actual liquid–solid contact area beyond that represented by the roughness value alone.

These structural features may also affect bubble dynamics during boiling. The presence of cavities and porous regions can influence bubble growth, coalescence and departure behaviour, while the interconnected pore network may facilitate liquid replenishment through capillary-driven transport. Such liquid transport pathways can promote rewetting of the heated surface following bubble departure and help maintain a larger number of active nucleation sites. Therefore, although the substantially increased roughness is an important characteristic of the cold sprayed surfaces, the enhanced boiling performance observed in this study is more likely to result from the combined effects of increased roughness, enlarged effective surface area, cavity-assisted nucleation and improved liquid transport within the porous structure.

4.2.3 Tomographic reconstruction

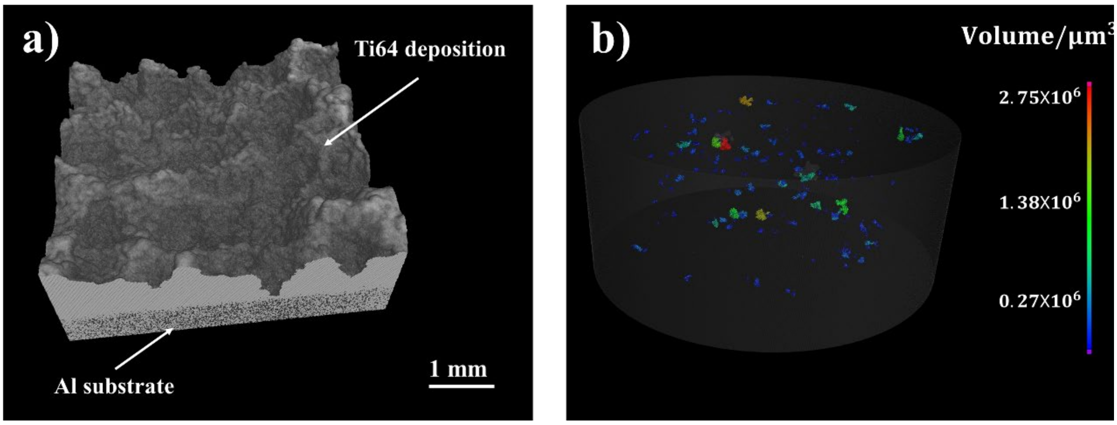

Figure. 36 a) Micro-CT reconstruction of the coating for Sample 2800-51-4. b) Localized magnification showing internal voids

Figure 36-a shows the 3D reconstructed Micro-CT image of the Ti64 coating (Sample 2800-51-4), while Fig. 36-b provides a locally magnified view. The 3D reconstruction reveals a coating layer with a distinctly undulating structure and an uneven surface. However, the interior of the coating is nearly solid. This observation is further clarified in the magnified view, where the semi-transparent areas represent the coating, and the coloured regions indicate internal voids within the coating. These pores are isolated and enclosed. Additionally, the scan results indicate that the internal porosity is only 0.18%. Thus, a third benefit of the coating is the increased wetted area of the exposed surface, with near solid metallic layer between the aluminium substrate and exposed boiling surface. However, the thickness of the solid underlayer of deposited material will offer

some additional conduction resistance to the heat transfer and will depend on the layer thickness. The thicknesses of the coatings are listed in Table 4.

4.2.4 Wettability

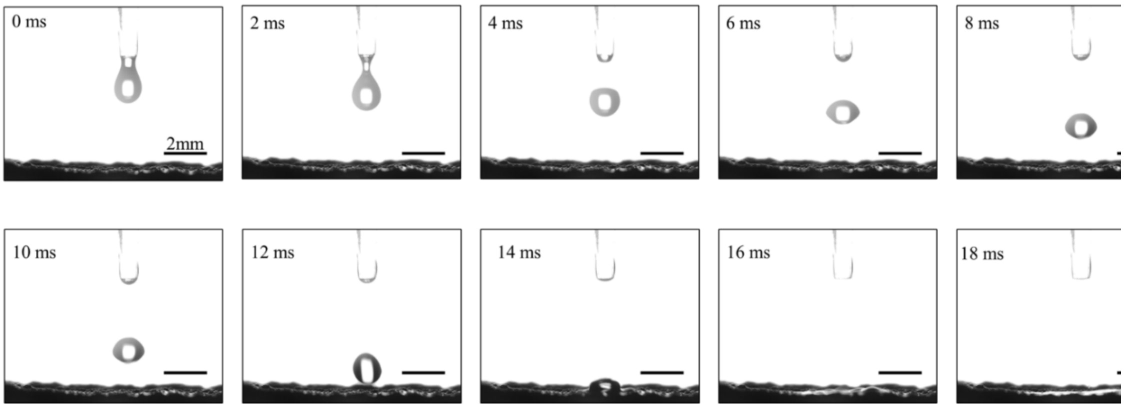

Figure. 37 Snapshot of FC-72 droplet impinging on the surface of Sample 2800-51-4

To evaluate the liquid spreading behaviour on the cold sprayed porous surface, Fig. 37 shows a sequence of images capturing an FC-72 droplet falling from a height of 5.4 mm and impinging on Sample 2800-51-4. The time interval between successive images is 2 ms.

As shown in Fig. 37, the droplet spreads rapidly upon contacting the surface and subsequently penetrates into the porous structure. This behaviour indicates strong liquid affinity and efficient liquid transport on the cold sprayed porous surface. The rapid spreading process increases the contact area between the liquid and the surface, while the interconnected pores facilitate liquid redistribution through capillary-driven flow.

Such spreading and liquid transport characteristics are beneficial for boiling heat transfer. During boiling, the departure of vapor bubbles creates temporarily dry regions on the heating surface. Rapid liquid spreading and replenishment can accelerate the rewetting of these regions, thereby maintaining effective liquid-solid contact and promoting continuous heat transfer. Furthermore, the granular morphology and interconnected pore structure observed on the cold sprayed surface are expected to enhance capillary-assisted liquid transport, which further contributes to the improved boiling performance discussed in the following sections.

Therefore, Fig. 37 is presented as qualitative evidence of the liquid spreading and replenishment capability of the porous cold sprayed surface, which is considered one of the mechanisms contributing to boiling heat transfer enhancement.

4.3 Pool boiling heat transfer

For each sample, the boiling curve under saturation conditions were generated by incrementally increasing the heat flux, giving sufficient time at each setting to ensure that steady-state conditions were reached before recording data. Tests were considered complete if a transition to film boiling occurred, indicating the occurrence of the boiling crisis (CHF), or if a maximum superheat of ~100 K was reached. At least three repetitions were performed for each sample to verify the repeatability of the measurements.

4.3.1 Validation of experimental apparatus

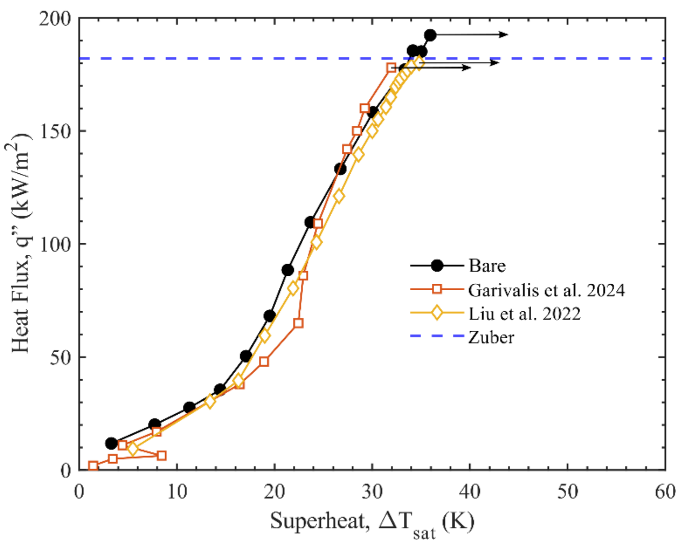

Figure. 38 Boiling curves of the bare sample in saturated FC-72 compared with published data and the Zuber correlation

Before testing the coated samples, the repeatability of the boiling apparatus was tested with the bare sample. Fig. 38 shows a comparison of the boiling curve of the bare sample of this study together with FC-72 boiling curves at saturation available in the literature. In addition, the measured CHF (indicated with arrows) was compared with the Zuber correlation for finite size heaters. From Fig. 38 we can assume that the measurement and testing procedures are adequate and can be used to characterise the coated samples. The slight differences between the curves (in terms of superheat and CHF) are partially a result of the different substrates tested and partially due to the inherent scatter in boiling heat transfer experimentation. For future reference, it is noted that boiling incipience, as indicated by the clear change in slope of the boiling curve, occurred at a heat flux of q''~50 kW/m^2 and wall superheat of ΔT_{sat}~20K. This is attributed to the transition from a single-phase buoyant natural convection heat transfer regime to the nucleate boiling regime subsequent to activation of nucleation sites on surface.

To further evaluate the reliability of the boiling measurements, an uncertainty analysis was carried out for both the directly measured quantities and the derived thermal parameters. The primary measured quantities include temperature, electrical power, thermocouple locations and geometric dimensions of the copper heating block. All T-type thermocouples used in this study were calibrated prior to testing, with a measurement accuracy of ±0.3 K. The electrical power supplied to the heaters was determined from the measured voltage and current using calibrated instruments.

Unlike the primary quantities, the heat flux was not measured directly but calculated from the temperature gradient inside the copper heating block using Fourier's law of heat conduction. The temperature gradient was obtained through linear regression of the temperatures measured by the three embedded thermocouples positioned along the heating direction. Consequently, the uncertainty in the calculated heat flux arises from the combined uncertainties associated with thermocouple accuracy, thermocouple positioning, copper thermal conductivity and the linear fitting procedure.

The heat transfer coefficient was subsequently calculated from the measured heat flux and the wall superheat. Therefore, its uncertainty represents the propagation of the uncertainties associated with both heat flux and surface temperature measurements. Uncertainty propagation was evaluated using the standard root-sum-square method, assuming the individual measurement uncertainties were statistically independent.

To assess the repeatability of the boiling experiments, each surface was first subjected to an initial conditioning test to eliminate residual gas trapped inside the porous structures and to stabilise the surface condition. Subsequently, three independent boiling experiments were performed under identical operating conditions. The average values are reported throughout this thesis, while the error bars correspond to one standard deviation of the repeated measurements.

Based on the uncertainty propagation analysis, the overall uncertainty of the calculated heat flux was estimated to be approximately 3.8%, which is comparable to the uncertainty levels commonly reported in pool boiling experiments. The relatively small uncertainty, together with the good repeatability obtained from repeated measurements, demonstrates that the experimental apparatus and data reduction procedure provide reliable measurements for evaluating the boiling heat transfer performance of the investigated surfaces.

4.3.2. Pool boiling heat transfer performance

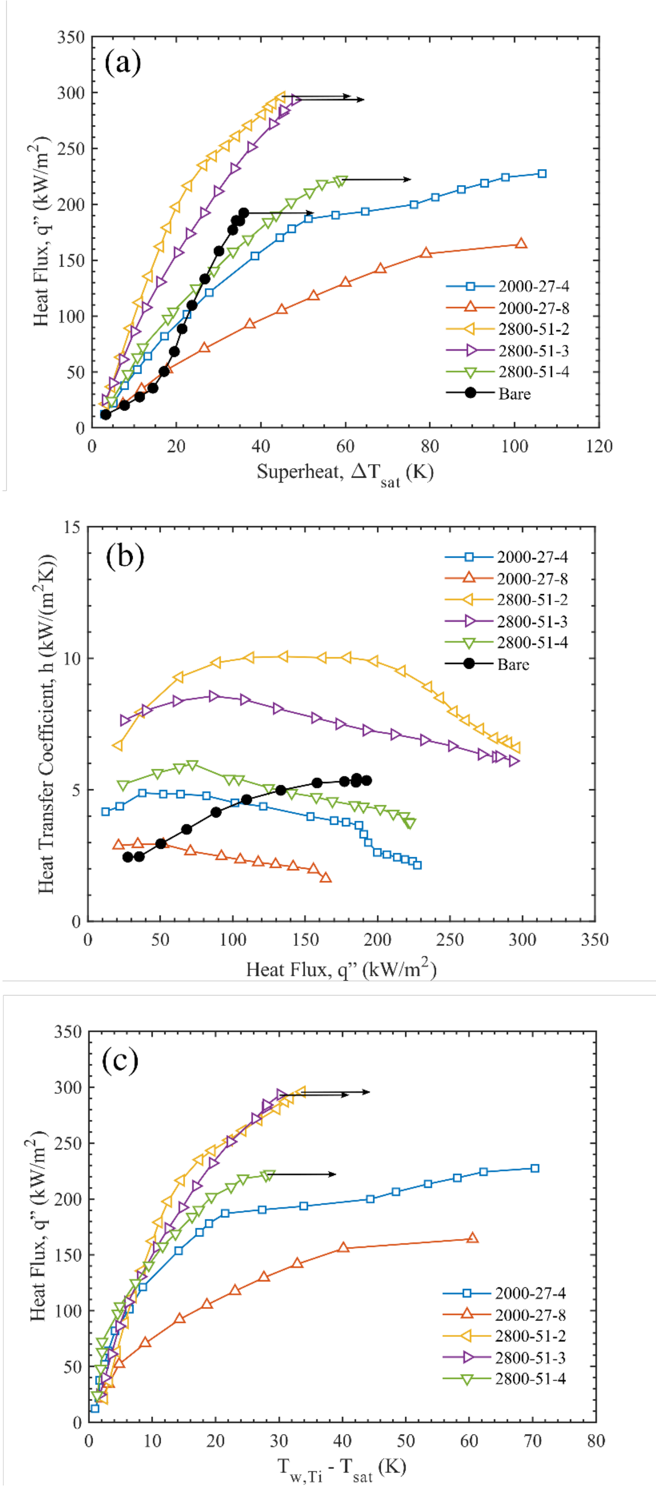

Figure. 39 a) Boiling curves of all tested surfaces. (b) Effective boiling heat transfer coefficient versus heat flux. (c) Boiling curves adjusted for coating

thickness. The CHF is indicated with arrow.

The boiling curves and the associated boiling heat transfer coefficients for each tested surface are plotted in Fig. 39. It can be observed from Fig. 39-a that the CHF of the tested cold spray samples with fewer layers (Samples 2800-51-2 and 2800-51-3, with 2 and 3 layers respectively) increased by about 60% compared to the bare surface, and the boiling heat transfer coefficients increased by an impressive factor of about 3X at lower heat fluxes, reducing to a factor of about 2X at higher heat fluxes. For the sample with a higher number of layers (Sample 2800-51-4, with 4 layers), the CHF moderately increases by only 13% and the heat transfer coefficients at higher heat fluxes are comparable to the bare surface, although there is still significant enhancement at the lower heat flux range (<100 kW/m²). Similar enhancement of the heat transfer at lower heat fluxes with like deterioration is observed for the thickest samples (Samples 2000-27-4 and 2000-27-8), though these did not experience a sharp CHF, and were able to sustain steady-type boiling up to the selected cut-off superheat of ~ 100K.

It should be reiterated that the wall temperature (T_{wall}) considered here in the calculation of the superheat is relative to the top surface of the aluminium insert (beneath the coating). The titanium alloy has a relatively low thermal conductivity (~10 W/m K) and the coating thicknesses of the samples range between 0.5 and 2.5 mm (Table 4). As a result, the thermal resistance of the intermediate cold sprayed layer between the aluminium inserts and the exposed surfaces becomes non-negligible as the thickness of the coating increases, and this is captured in the calculated heat transfer coefficients plotted in Fig. 39-b, which as mentioned, are more appropriately regarded as effective heat transfer coefficients referenced to the top of the aluminium insert. From an application point of view, this effective heat transfer coefficient is of practical significance as it relates to the overall effectiveness of cooling, with the aluminium surface being considered as the heat source. When the thermal resistance of the interlayer is significant, the temperature drop between the aluminium wall and the boiling interface increases with higher heat flux. This results in a larger difference between the apparent and actual superheat. This is depicted in Fig. 39-c, where a simple adjustment has been made to gain a first approximation of the boiling surface temperature by including the appropriate conduction resistance across the intermediate cold spray layers,

$$T_{w,Ti} = T_{wall} - \text{q"} \left(\frac{S_{Ti}}{k_{Ti}} \right) \quad (7)$$

where $T_{w,Ti}$ is the approximated temperature of the exposed boiling surface, S_{Ti} is the thickness of the deposited layer (Table. 4), and k_{Ti} is the thermal conductivity of the titanium alloy. As Fig. 39-c shows, this simple approximation of the exposed surface superheat collapses most boiling curve data up to ~150 kW/m^2, indicating that the differences observed in Fig. 39-a are due to the layer thickness, not necessarily the boiling dynamics. For higher heat fluxes, which corresponds to higher vapour production rates, the surface morphology is influential, and as discussed earlier is related to the number of deposited layers. Further detail about the surface morphology will be reported below, noting that it is not possible here to isolate individual influences, though each topology and roughness as well as wettability are well known to influence the boiling heat transfer.

4.4 Bubble behavior during the boiling process

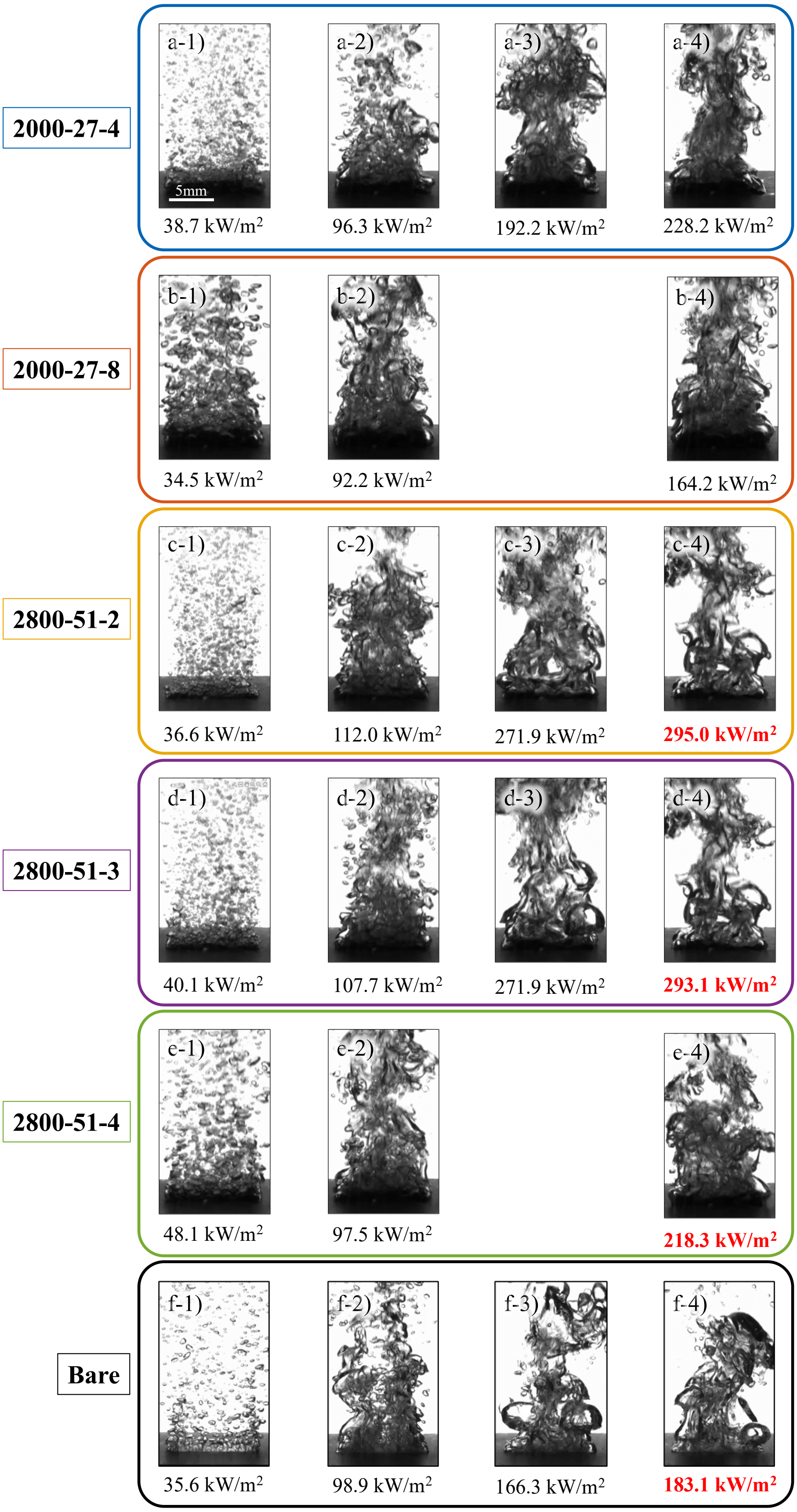

Figure. 40 Behaviour of bubbles on the boiling surfaces at different heat fluxes

In order to gain a qualitative understanding of the mechanism of enhanced boiling heat transfer, the dynamic behaviour of bubbles during boiling were recorded and visualised in this study by a high-speed camera. The results given in Fig. 40 show that the boiling phenomenon for each surface show some similarities. Movies are available in the Supplementary Material. In particular, with increasing heat flux the boiling dynamics sequentially reach boiling incipience and subsequently go through an isolated bubble stage, a vapour column stage, and finally a mushroom-shaped vapour cloud is formed on the heated surface when CHF is approached.

Figures 40-a-1, 40-b-1, 40-c-1, 40-d-1, 40-e-1, and 40-f-1 illustrate that subsequent to incipience, boiling occurs in the isolated bubble boiling regimes for each test surface. According to the different behaviours of the bubbles, they can be divided into three stages: bubble nucleation, bubble growth and bubble detachment. When the small cavity-type features on the heat transfer surface satisfy the minimum radius required for bubble nucleation, bubbles are generated at these nucleation sites. As heating continues, the bubbles grow until their buoyancy is sufficient to overcome the surface adhesion and they detach from the surface. In the isolated bubble regime, the generated bubbles do not significantly interfere with each other and detach from the surface independently. As the heat load increases, so does the vapour production rate. This is accommodated by a substantial increase both the bubble frequency and the number of active nucleation sites on the heat transfer surface. Indeed, the bubble frequency and nucleation site density increase to a point that successive and neighbouring bubbles interact with each other, merging and coalescing to form vapour blocks and vapour columns, as shown in Figures 40-a-2, 40-b-2, 40-c-2, 40-d-2, 40-e-2 and 40-f-2 and Figures 40-a-3, 40-c-3, 40-d-3, and 40-f-3. Escalating the heat flux further continues to increase the vapour production rate to the point that vapour clusters and columns in the proximity of the surface merge to form a mushroom-shaped vapour cloud (Figures 40-a-4, 40-b-4, 40-c-4, 40-d-4, 40-e-4, and 40-f-4). Here the vapour production rate is so high that the heat transfer surface struggles to rewet and vapour contact impedes effective heat transfer. For all sample surfaces barring Sample 2000-27-4 and 2000-27-8 , the CHF is eventually reached where rewetting is impeded to the point that the wall temperature rises sharply. As mentioned, Samples 2000-27-4 and 2000-27-8 manage to sustain steady yet deteriorated boiling type behaviour without a clear CHF, though to unsafe superheat levels for the present test facility.

By comparing the dynamic behaviour of bubbles on the different test surfaces at different heat fluxes, the following key observations are of note. First it is first clear from Fig. 40-a and Fig. 40-c that the cold sprayed surfaces reach boiling incipience almost immediately, compared with the bare surface that experiences a buoyant natural convection stage up to an incipience heat flux of ~50 kW/m^2. This is unsurprising considering the clear differences in surface microstructures pictured in Fig. 34 and Fig. 35, with the textured surfaces being more granular with a wider range of potential nucleation sites. Corresponding to the boiling test results, the higher the roughness, the higher the CHF. Notably, cold sprayed Samples 2800-51-2 and 2800-27-3 have the highest roughness as well as the highest CHF enhancements, of ~60%. Additionally, as Fig. 35-c indicates, these surfaces with the highest roughness have the highest level of boiling heat transfer enhancement at higher (>150 kW/m^2) heat fluxes. Secondly, at lower heat flux levels, isolated bubbles are mainly generated on the surface. For the baseline bare surface, the nucleation site density is notably lower than the textured surfaces (Fig. 35) and further analysis of the video footage determined that the bubbles were smaller and the detachment frequency lower. In contrast, on the cold sprayed surfaces, the nucleation site densities are visibly higher (Figures 40-a-1, 40-b-1, 40-c-1, 40-d-1, 40-e-1, and 40-f-1) and analysis of the video footage determine that the bubbles grow and detach more rapidly. Owing to the higher density of rapidly detaching bubbles, likely in combination with the additional overall heat transfer surface area, the heat transfer coefficient is substantially higher than the baseline surface (Fig. 35-b). Only the thickest Sample 2000-27-8, with the high conductive thermal resistance, performs worse than the baseline bare surface.

At moderate heat fluxes, the isolated bubbles gradually merge and coalesce to form vapour clusters, followed by further merging into vapour columns. As can be seen from Fig. 40, continuous vapour clusters and vapour columns have already been formed on the bare surface at $q'' \sim 100$ kW/m^2, whereas a large number of isolated bubbles are still present on the enhanced surfaces at similar heat flux levels. In other words, the bubbles on the bare surface are more likely to merge into vapour columns and clusters, whereas this is not the case for the cold sprayed porous surface. It is hypothesized that this is a key mechanism that explains both the higher intensity of boiling heat transfer and increased CHF.

When the bubbles on the surface merge into vapour columns and clusters at the surface, local hotspots tend to appear on the surface owing to exposure to vapour. Indeed, once these hotspots extend over the entirety of the surface it leads to the rapid emergence of CHF. Considering the thinnest Sample 2800-51-2 , the enhanced cold sprayed surface topology is that of numerous dispersed cavities, of approximate width of 200 μm – 500 μm and 300 μm depth (Fig. 34 and Fig. 35). Bubbles which form within these cavities are likely to be inhibited from spreading laterally and coalescing with neighbouring bubbles. This likely mitigates the emergence of vapour clusters at the surface and sustains both high boiling heat transfer intensity and delays the onset of CHF.

4.5 Comparison with other additive enhancement techniques

4.6 Summary

The main motivation for the present research is to develop industrially scalable manufacturing techniques for boiling heat transfer enhancement. To this end, this present study successfully demonstrated the potential of cold spray technology to enhance boiling heat transfer of a highly wetting fluid (FC-72) on aluminium substrates by creating textured Ti64 surfaces. The experiments revealed that significant improvements in both boiling heat transfer intensity and Critical Heat Flux (CHF) are achievable, though depended on the manufacturing process parameters of the cold spray deposition of the surface coatings.

The main findings of the study are as follows:

1. The unique cold spray process developed can create granular type surfaces with dispersed cavity-type indents. Compared with the baseline bare surface, these textured surfaces show two order of magnitude higher roughness and highly wetting properties with the working fluid.

2. Measurements have determined that, compared with the baseline flat surface, a two-to-three-fold enhancement in the overall heat transfer coefficient is attainable with certain cold sprayed coatings. Importantly, this level of heat transfer enhancement occurred in tandem with ~60% increase in CHF.
3. For all textured surfaces, boiling incipience occurred at the lowest heat flux setting, whereas boiling did not initiate on the baseline bare surface until approximately 50 kW/m^2.
4. Coating thickness plays a crucial role. The results suggest that maintaining a small coating thickness (and thus, a small conductive resistance of the coating) is crucial for optimal performance. The highest heat transfer enhancement was observed at a thickness of approximately 0.5–0.6 mm in the present study. Furthermore, increasing the number of deposited layers during the cold spray deposition process tended to influence the surface morphology. These can lead to deterioration of the overall boiling heat transfer performance.
5. The key mechanism for increasing boiling heat transfer intensity and CHF is related to the formation of bubbles in a large number of cavity-type structures on the surface of the cold spray. First, cavities with rough surfaces make it easier for bubbles to form there. Secondly, these cavities are likely to act as physical barriers between neighbouring bubbles, preventing lateral bubble coalescence.

Overall, this work has demonstrated a new manufacturing technique to produce unique surfaces with the capacity to enhance boiling heat transfer. Importantly, the surfaces are mechanically robust, and the manufacturing technique is industrially scalable. Future work will focus on realizing coatings with the same technique using materials such aluminium, stainless steel, and copper. The material used must have higher thermal conductivity than titanium to minimize the additional thermal resistance of the coating while maintaining good fluid compatibility and durability over multiple boiling cycles.

Chapter 5 Investigation of controlled patterned cold spray coating preparation and heat transfer performance based on surface pretreatment

Previous investigations have demonstrated that Ti64 can spontaneously form a surface open pore structure with honeycomb like characteristics during the cold spray deposition process. This phenomenon originates from the dispersion of particle velocities and the resulting selective bonding behavior. Pool boiling experiments further confirmed that such structures can significantly reduce the bubble nucleation superheat and increase the critical heat flux, thereby exhibiting considerable potential for the enhancement of boiling heat transfer. However, Ti64 itself possesses relatively low thermal conductivity, which may limit the overall heat conduction capability under high heat flux conditions. Therefore, after clarifying the formation mechanism of the porous surface structure in Ti64, it becomes necessary to extend this structural formation principle to metallic systems with superior thermal conductivity. Such an extension would enable the combination of the advantages of porous structures with the favorable thermal transport properties of high conductivity materials.

Based on the mechanism of selective deposition and deposition non-uniformity proposed in Chapter 3, this chapter introduces a geometrical regulation strategy based on substrate surface pretreatment. By machining specific geometric patterns on the aluminum substrate prior to cold spray deposition, local regions with reduced deposition efficiency can be intentionally created during the spraying process. This approach induces a spatially controlled non uniform distribution of the deposited structure, thereby enabling the controllable formation of surface open pore structures. Because aluminum possesses significantly higher thermal conductivity, this method is expected to maintain the advantages of porous structures in enhancing boiling heat transfer while simultaneously improving the overall heat transfer capability. In addition, it enhances the controllability and reproducibility of structural design.

On this basis, a hole array structure is selected as the primary research object in this chapter. The influence of geometric parameters and process parameters on boiling heat transfer performance is systematically analyzed. Particular attention is given to the effects of hole diameter, hole spacing, and coating layer number on the critical heat flux. Through orthogonal experimental design and response surface analysis, the contributions of these parameters to the critical heat flux are quantitatively evaluated. A correlation model is then established to describe the relationship among geometric parameters, structural morphology, and heat transfer performance. In combination with surface morphology characterization, three dimensional structural reconstruction, and bubble dynamics observation, the synergistic enhancement mechanism of the periodic hole array is further clarified. This mechanism includes the stabilization of bubble nucleation, the promotion of liquid replenishment pathways, and the suppression of lateral bubble coalescence.

Based on the above research background, the main objectives of this chapter are as follows.

• This chapter proposes a geometrical regulation strategy based on substrate pretreatment to enable the controllable construction of surface open pore structures produced by cold spray.

• The influence of different geometric pretreatment patterns, including hole arrays and line arrays, on the spatial distribution of deposition efficiency is systematically examined.

• Particular attention is given to the effects of hole array geometric parameters, including hole diameter and hole spacing, together with coating layer number, on boiling heat transfer performance.

• By employing orthogonal experimental design and response surface analysis, a quantitative correlation model between geometric parameters, structural morphology, and critical heat flux is established.

• Bubble dynamics observation combined with structural characterization is conducted to elucidate the synergistic mechanism by which periodic hole arrays enhance boiling heat transfer.

5.1 Material and methodology

5.1.1 Feedstock powder and cold spray process

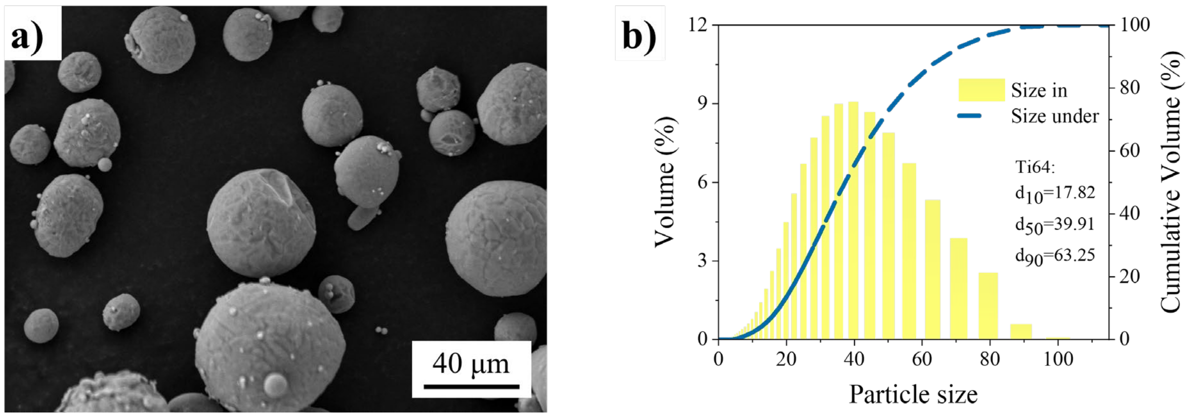

Figure. 41 a) SEM characterization of the gas atomized pure Al amorphous powder for cold spray process. b) Particle size distribution of the pure Al powder

Gas-atomized pure aluminum powder, purchased from Powder Range Inc. (USA), was used as the starting material in this study. Fig. 41-a shows the scanning electron microscopy (SEM, Carl Zeiss ULTRA Plus, Germany) image of the powder. The particles exhibit an approximately spherical morphology with smooth surfaces, while small satellite particles are observed adhering to larger ones due to differences in solidification rates.

The particle size distribution was determined using a laser diffraction particle size analyzer (Mastersizer 2000, Malvern Instruments, UK), as shown in Fig. 41-b. The powders display a size range of 15–80 μm, with median values of D10 = 17.82 μm, D50 = 39.91 μm, and D90 = 63.25 μm.

Prior to cold spraying, four distinct pretreatment patterns were designed and fabricated on the substrate surface, including an array of holes, parallel straight line arrays, curved line arrays, and concentric circular ring arrays. Based on preliminary surface morphology, the hole array structure demonstrated potential advantages in heat transfer performance. Therefore, the systematic investigation in this study primarily focused on the hole array pretreated samples to further explore the relationship between their surface structural features and heat transfer performance.

In the pre-treatment stage of the array-hole pattern, two key parameters were controlled:

hole diameter (0.5 mm, 1.0 mm, and 1.5 mm) and pitch (0.5 mm, 1.0 mm, and 1.5 mm). The coating thickness was subsequently adjusted by varying the number of cold spray deposition passes, corresponding to two conditions: single-layer and double-layer coatings.

To evaluate the relative influence of the three aforementioned factors on boiling heat transfer performance, an orthogonal experimental design was conducted using Minitab software. The parameters were systematically combined and arranged, with the critical heat flux (CHF) selected as the key evaluation metric to analyze the significance and influence trends of each factor. The detailed experimental parameter settings are summarized in Table 5.

Table. 5 Orthogonal design matrix for Diameter (D), Pitch (P), and Number of Layers

No.	**Sample name**	**Pitch**	**Diameter**	**Number of layers**
1	P0.5-D0.5-1	0.5	0.5	1
2	P0.5-D0.5-2	0.5	0.5	2
3	P0.5-D1.0-1	0.5	1.0	1
4	P0.5-D1.0-2	0.5	1.0	2
5	P0.5-D1.5-1	0.5	1.5	1
6	P0.5-D1.5-2	0.5	1.5	2
7	P1.0-D0.5-1	1.0	0.5	1
8	P1.0-D0.5-2	1.0	0.5	2
9	P1.0-D1.0-1	1.0	1.0	1
10	P1.0-D1.0-2	1.0	1.0	2
11	P1.0-D1.5-1	1.0	1.5	1

12	P1.0-D1.5-2	1.0	1.5	2
13	P1.5-D0.5-1	1.5	0.5	1
14	P1.5-D0.5-2	1.5	0.5	2
15	P1.5-D1.0-1	1.5	1.0	1
16	P1.5-D1.0-2	1.5	1.0	2
17	P1.5-D1.5-1	1.5	1.5	1
18	P1.5-D1.5-2	1.5	1.5	2
19	Bare surface with holes	1.0	1.0	0
20	Bare surface without holes	0.0	0.0	0

5.1.2 Microstructure characterization

The morphology of the feedstock powder and the cold-sprayed boiling surfaces was examined using scanning electron microscopy (SEM, Zeiss Ultra). The three-dimensional structural features of the deposited coatings were reconstructed with an X-ray computed tomography system (Nikon XTH225 ST). Surface roughness was measured using a 3D laser scanning confocal microscope (VK-X1000, Keyence). During boiling experiments, bubble dynamics were recorded by a high-speed camera (HotShot).

5.2 Comparison of surface-pretreated coatings with different patterns and their heat transfer performance

5.2.1 Surface pretreatment methods and coating construction for different patterns

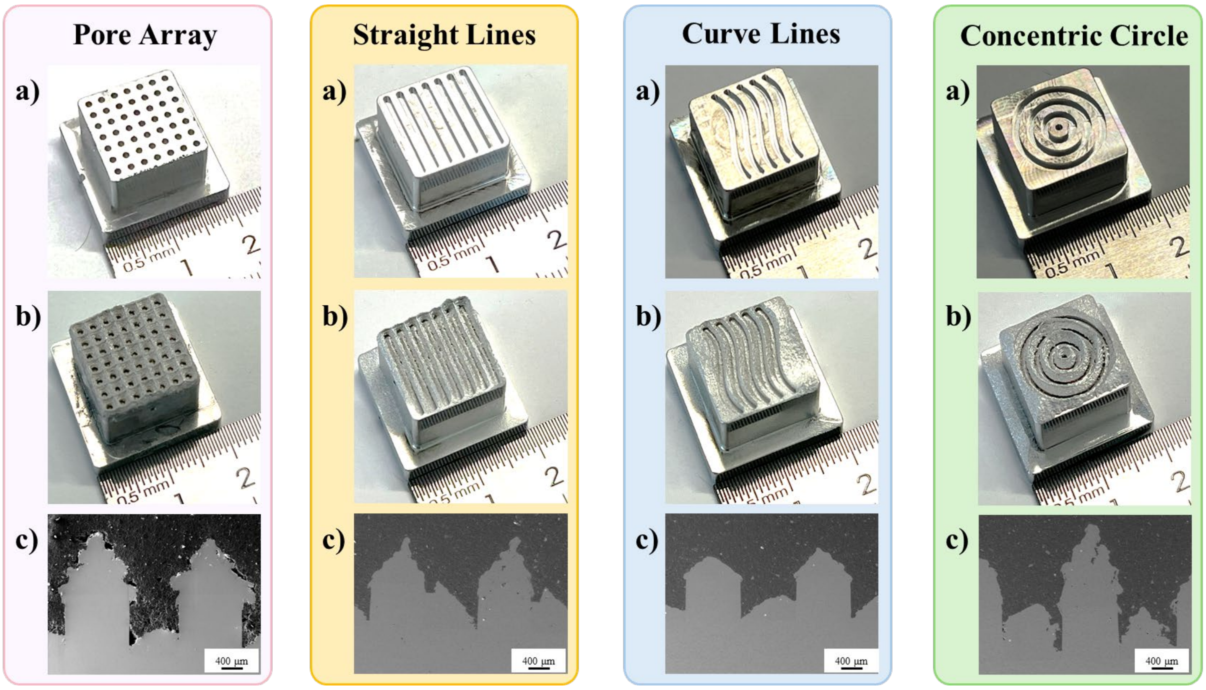

Figure. 42 Surface and cross-sectional morphologies of coatings deposited by cold spray on substrates with different pretreated surface patterns

A clear comparison between pre-spray and post-spray morphologies reveals that all four types of surface patterns were successfully retained after cold spraying (shows in Fig. 42), demonstrating the excellent geometric fidelity of the process. The high-velocity solid-state deposition did not completely flatten or obscure the pre-machined features. Instead, powder particles spread and accumulated following the existing surface contours rather than fully reshaping them, thereby preserving the original surface architecture.

For Pattern 1, the hole-array remains clearly discernible after spraying, with minimal change in spacing and diameter. Slight particle accumulation is observed around the hole edges. Cross-sectional observations indicate that a thin deposited layer forms at the hole bottom, suggesting partial penetration and adhesion of cold-sprayed particles under high impact velocity, while the interior of the holes still retains visible voids. In contrast, Patterns 2–4 (linear, curved, and concentric ring arrays) also preserve their morphological outlines, though the grooves were partially filled during deposition. Their boundaries remain well defined, implying strong geometric stability of these linear-type structures under cold spray conditions.

Cross-sectional analysis further highlights distinct deposition characteristics among the four patterns. The hole array, featuring enclosed sidewalls, alters the local gas flow and particle trajectories, forming turbulence zones near the hole openings and thus reducing local deposition efficiency[117]. Conversely, the linear and curved patterns possess smoother geometries that facilitate particle sliding and accumulation along the surface, resulting in thicker deposits. These differences indicate that when particles encounter confined geometries, their kinetic energy transfer and bonding behavior are locally constrained, leading to heterogeneous deposition distributions.

Overall, this combined surface pretreatment and cold spray strategy provides a promising route for fabricating functional coatings with complex surface morphologies. By selecting different pretreatment geometries, surface structural features can be tailored without modifying spraying parameters, demonstrating superior pattern replication and process flexibility.

5.2.2 Comparison of boiling heat transfer performance for patterned coatings

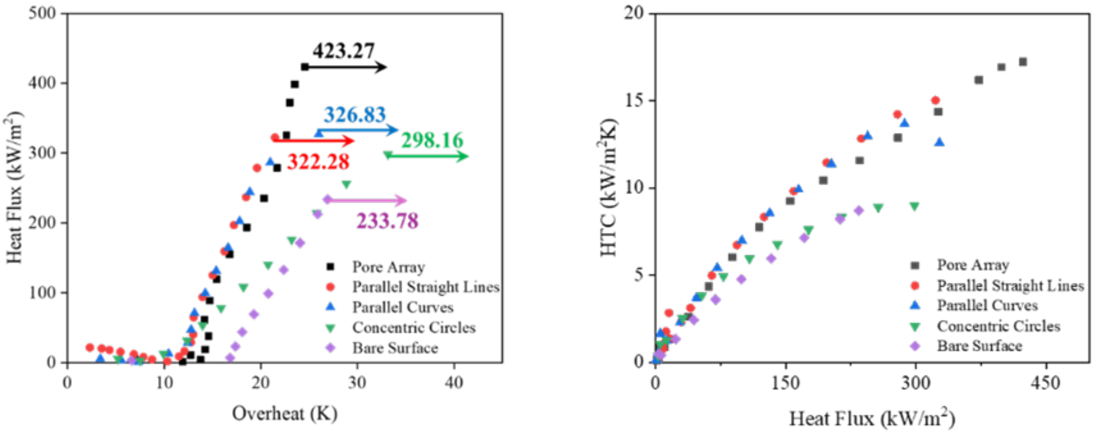

Figure. 43 Boiling curves (left) and heat transfer coefficient (right). CHF location is indicated with an arrow

Fig. 43 illustrates the boiling curves and the corresponding heat transfer coefficient variations as a function of heat flux for all tested surfaces. All cold-sprayed coatings exhibit pronounced boiling enhancement in the low heat flux region, where the surfaces rapidly transition into the nucleate boiling regime with steeply rising curves. This indicates efficient activation of vapor nuclei, enabling frequent bubble nucleation and departure at relatively low superheat.

As the heat flux increases, performance differences among the samples become more evident. Patterned coatings such as the Parallel Straight Lines and Parallel Curves maintain high boiling efficiency over the medium to high heat flux range, achieving critical heat flux (CHF) values above 300 kW/m². CHF is the upper limit point at where heat transfer is no longer possible to the aggressive formation of vapor in the solid-liquid interface. The pore array coating shows the most significant improvement, with a CHF exceeding 400 kW/m², corresponding to an enhancement of up to 181% compared with the uncoated surface. In general, all of the cold sprayed features perform better at moving a heat flow from solid into a liquid against a flat surface, confirming a considerable developmental potential.

The heat transfer coefficient results further confirm that most cold-sprayed surfaces deliver substantial enhancement at low to moderate heat fluxes, reaching peak values well above those of the bare substrate. This improvement is mainly attributed to the rough multiscale surface structures, which provide a high density of active nucleation sites and promote bubble departure. At higher heat fluxes, however, some coatings exhibit a reduction in heat transfer coefficient, suggesting that coating geometry and thermal transport limitations begin to constrain performance. Overall, the boiling enhancement strongly depends on coating thickness, surface morphology, and vapor generation behavior.

Notably, the hole-arrayed Pattern 1 maintains pronounced surface roughness after spraying, which is advantageous for constructing efficient boiling heat-transfer interfaces. Therefore, subsequent research focusing on optimizing spraying parameters and evaluating the heat-transfer performance of hole-patterned substrates is both rational and of practical significance.

5.3 Preparation of porous array coatings and enhancement of heat transfer performance

5.3.1 Surface characteristic analysis

5.3.1.1 Surface morphology

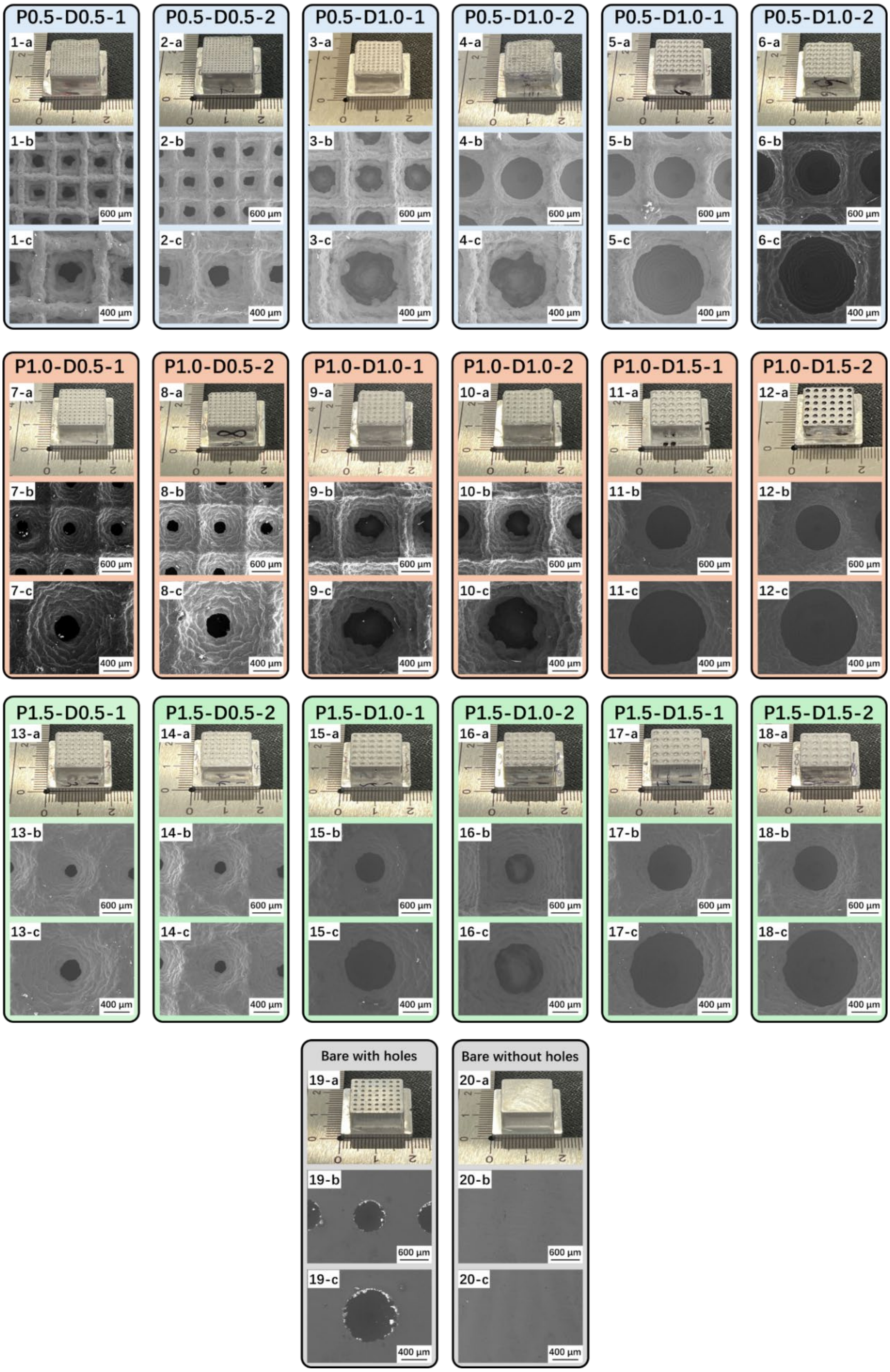

Figure.44 a) Macrophotograph of the boiling surface, b) SEM image of the boiling surface at 30× magnification, c) SEM image of the boiling surface at 60× magnification

Fig. 44 presents the macroscopic photographs (group a), SEM images at 30× magnification (group b), and SEM images at 60× magnification (group c) of the boiling surfaces fabricated with different pitch (P), hole diameter (D), and coating thickness (number of deposition layers). For reference, the bottom panel shows the morphologies of the bare substrates with drilled holes (Bare with holes) and without drilled holes (Bare without holes). The bare surface without holes appears generally smooth, with only minor machining scratches. The drilled substrate exhibits a regular array of circular holes with uniform diameter and spacing, relatively smooth inner walls, and slight burrs remaining at the hole edges due to machining.

Similar to the reference substrates, the cold-sprayed samples exhibit well-defined periodic hole-array structures, however, with multi-scale rough features emerging around the hole periphery and the surrounding surface. In the macroscopic images (group a), the hole arrays appear well arranged under all processing conditions, although clear morphological differences are visible at the hole edges. The 30× SEM images (group b) reveal that the surface of the hole walls and surrounding surfaces are fully covered by deposited particles, forming dense and irregular rough structures. The particle size and stacking morphology vary with both the number of spray passes and the hole diameter. At higher magnification (group c), the hole inner walls are shown to be not completely smooth, but rather accompanied by slight wavy or granular undulations, which provide additional potential nucleation sites for stable bubble formation.

Specifically, when the hole spacing is small (e.g., P = 0.5 mm), the deposition zones between adjacent holes are narrow, leading to more concentrated particle stacking with stronger interaction between neighboring regions. In contrast, at larger hole spacing (e.g., P = 1.5 mm), the inter-hole deposition areas are wider and exhibit more uniform morphologies. With increasing hole diameter (e.g., D = 1.5 mm), the surface of the holes become relatively smoother. Increasing the number of deposition passes further enhances particle accumulation on the hole walls and surfaces, resulting in more pronounced surface undulations and a three-dimensional hole edge profile.

From a boiling heat transfer perspective, the combination of the regular hole-array structures and the rough multi-scale surface features created by cold spraying not only provide abundant nucleation sites at the hole edges and inner walls, thereby increasing nucleation site density, but it also likely to suppress lateral coalescence of adjacent bubbles through the crest-like solid regions between holes. These effects collectively delay the triggering of CHF and significantly enhance boiling heat transfer performance.

5.2.1.2 Tomographic reconstruction

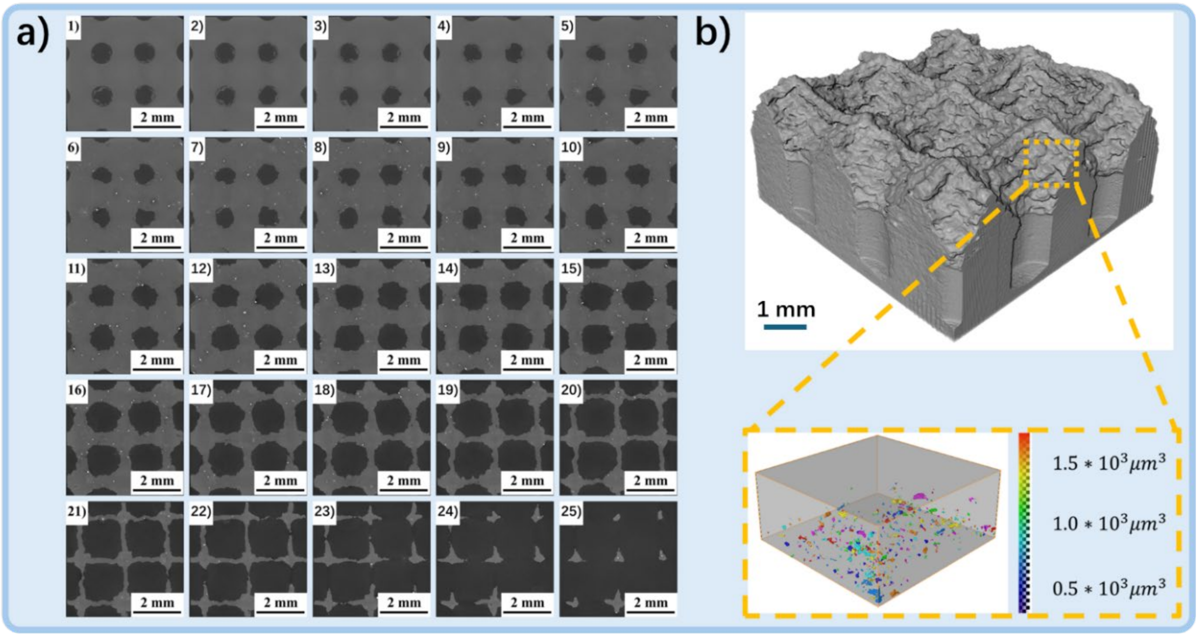

Figure. 45 a) 25 cross-sectional photographs from the substrate to the top of the coating, b) three-dimensional morphology reconstruction photographs and local enlargement images

Fig. 45-a shows representative micro-CT slice images (sample No.10)obtained by sequential scanning from the substrate to the coating, with a slice interval of 0.04 mm. The results indicate that the pre-machined holes in the substrate remained open and continuous after cold spray deposition, without being filled or blocked, suggesting that the deposition process formed stable boundary morphologies around the hole regions. Owing to the characteristic conical effect inherent in the cold spraying process[212], the deposited material gradually tapers from bottom to top as the deposition height increases. This manifests in the hole morphology as a progressive enlargement of hole diameter from the base upwards. Fig. 45-b presents the three-dimensional micro-CT reconstruction of the cold-sprayed hole-array surface, with a magnified view highlighting the structural features of the hole walls. The reconstructed morphology reveals a distinct wavy surface topography, with irregular hole edges accompanied by ripple-like rough features.

The internal structure of the coating appears dense, with an overall porosity of only 0.02%. The hole walls can therefore be regarded as fully solid, except for a few isolated closed holes. These enclosed holes have volumes primarily in the range of $0.5 \times 10^3 – 1.5 \times 10^3$ μm^3 (indicated by colored regions) and do not form interconnected channels. Therefore, the developed structure not only provides a large effective surface area and abundant nucleation sites on/around the hole openings and walls but also ensures a dense internal layer that reduces thermal resistance. As a result, the fabricated surfaces are expected to exhibit superior boiling heat transfer performance.

4.2.1.3 Roughness and specific surface area

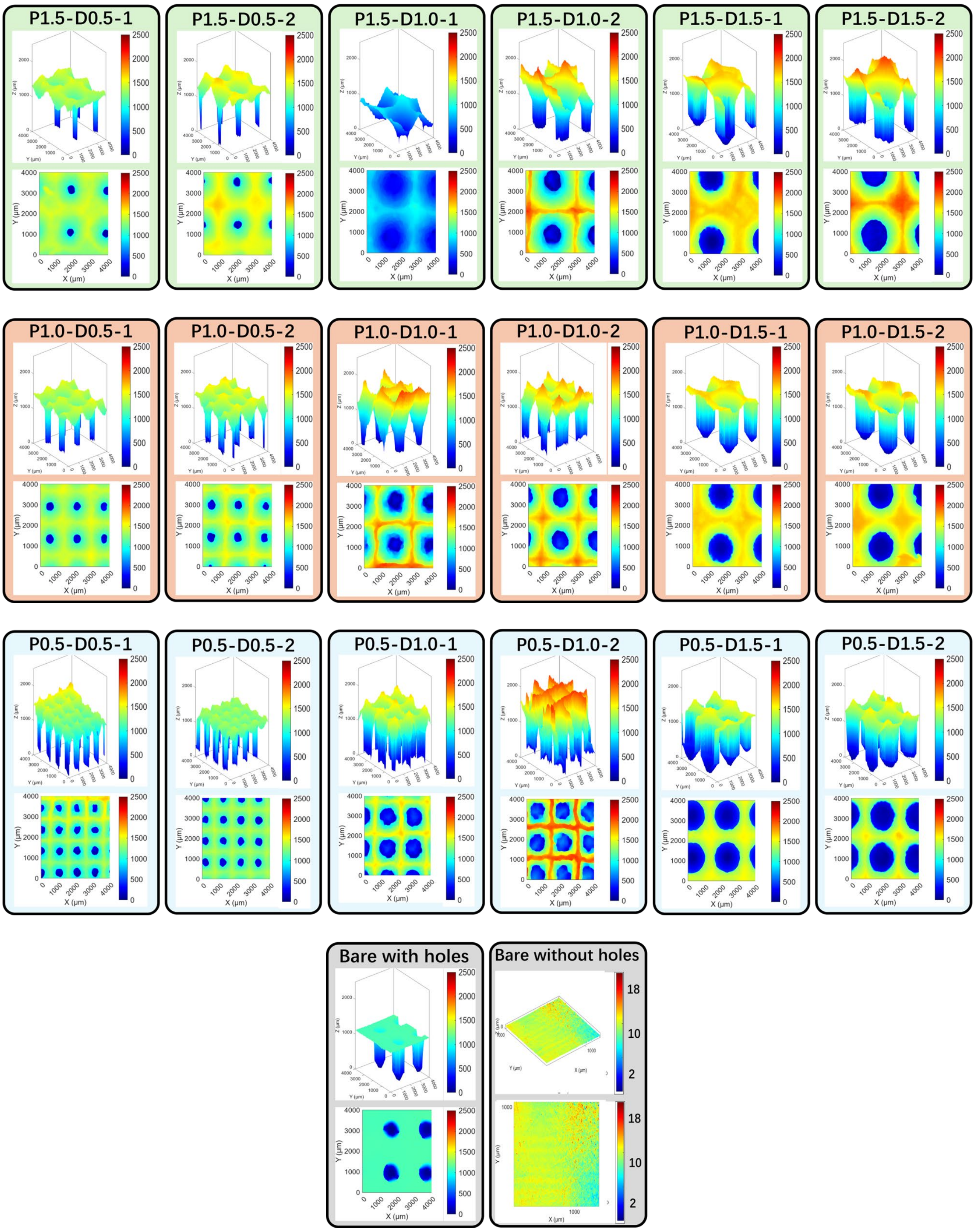

Figure. 46 White Light Interferometry images of tested boiling surfaces

Fig. 46 presents the three-dimensional surface profiles and corresponding height distribution maps of samples characterized by white light interferometry (WLI) under different processing parameters. All cold-sprayed coatings exhibit the characteristic periodic hole-array structures, with the surface height variations closely matching the hole contours. The overall morphology reveals valley-like features centered at the hole openings, while the inter-hole regions are elevated, forming pronounced peak-like roughness. Notably, the maximum surface roughness varies significantly among the different parameter combinations.

Compared with the reference substrates, the roughness of cold-sprayed surfaces increases by one to two orders of magnitude. The bare surface without drilling appears nearly flat, with height variations less than 20 μm and only minor random undulations. In contrast, the drilled but unsprayed substrate displays clear deep valleys at the hole locations, while the hole walls and inter-hole regions remain relatively smooth. For the cold-sprayed samples, however, densely deposited micron-sized particles cover the hole walls, hole edges, and inter-hole regions, leading to an overall elevation in surface height distribution. Sharp protrusions also emerge locally, with maximum peak heights exceeding 2000 μm. The corresponding roughness values for all samples are summarized in Table 2.

Regarding the effect of spraying parameters on surface morphology, increasing the number of deposition passes did not substantially increase the overall coating thickness (Table 2). This is attributed to the fact that the first deposition layer forms an uneven surface with sloped regions. During subsequent spraying, incident particles are more likely to rebound from these slopes rather than adhere, thereby reducing deposition efficiency and limiting further thickness growth. Larger hole diameters yield smoother transitions at hole edges and broader particle accumulation zones, while smaller hole diameters lead to more concentrated deposition along the hole walls, resulting in steeper peak-to-valley transitions. Moreover, when the hole spacing is small, the accumulation zones between adjacent holes become congested, causing significant mutual interference and a more complex overall morphology.

In addition, this study calculated the actual area ratio of the cold-sprayed hole-array structures, defined as the ratio of the total surface area of the hole-array structure to its projected area on the substrate. This parameter was used to quantify the extent to which the hole-array structure increases the overall surface area. The results show that the cold-sprayed coatings significantly increase the actual area ratio, indicating that they can provide a larger effective heat transfer area during boiling, which is expected to further enhance boiling performance. The quantitative roughness parameters of each sample are listed in Table 6.

Table. 6 Surface roughness, coating thickness, and specific surface area of the tested samples

No.	**Sample name**	**Roughness/μm**	**Thickness/ mm**	**Actual area ratio**
1	P0.5-D0.5-1	243.56	0.36	2.73
2	P0.5-D0.5-2	216.47	0.44	3.02
3	P0.5-D1.0-1	382.57	1.83	3.09
4	P0.5-D1.0-2	515.49	2.05	4.25
5	P0.5-D1.5-1	536.59	0.24	2.48
6	P0.5-D1.5-2	516.42	0.50	2.68
7	P1.0-D0.5-1	151.96	0.45	2.49
8	P1.0-D0.5-2	186.20	0.58	1.82
9	P1.0-D1.0-1	366.52	1.26	2.61
10	P1.0-D1.0-2	321.11	1.47	2.73
11	P1.0-D1.5-1	474.77	0.12	2.35
12	P1.0-D1.5-2	490.96	0.49	2.24
13	P1.5-D0.5-1	119.05	0.55	2.00
14	P1.5-D0.5-2	154.00	0.66	2.14
15	P1.5-D1.0-1	164.25	1.22	1.21

16	P1.5-D1.0-2	370.48	1.37	1.95
17	P1.5-D1.5-1	498.59	0.47	1.93
18	P1.5-D1.5-2	493.05	0.92	2.54
19	Bare surface with holes	0.93	0.00	1.69
20	Bare surface without holes	0.02	0.00	1.00

Overall, the cold-sprayed surfaces preserved the periodic geometric architecture while introducing multi-scale rough features, which markedly increased the effective surface/contact area and the number of potential nucleation sites, thereby laying the foundation for enhanced boiling heat transfer performance.

5.3.2 Analysis of boiling heat transfer performance

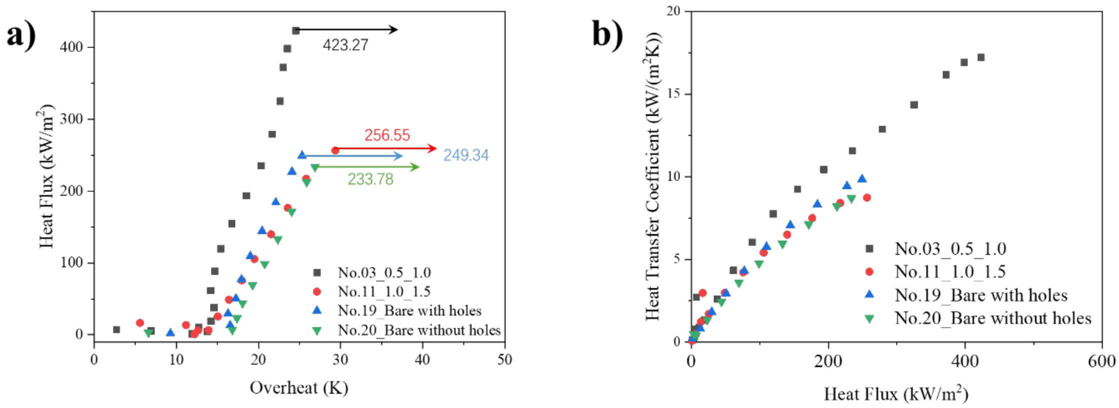

Figure. 47 Pool boiling curves obtained for representative samples

Fig. 47 compares the boiling curves for four representative samples including two coated samples, one bare sample without holes and one bare sample with holes. The complete set of boiling curves is provided in the Supplementary Material. The representative coated samples are chosen such that one sample exhibits best overall performance while other show least overall enhancement among the coated samples. Comparing the performance of smooth samples 19 and 20, it is evident that the drilled holes alone significantly improve boiling heat transfer coefficients throughout the nucleate boiling regime coupled with slight improvement in CHF. The cold-sprayed samples consistently deliver superior boiling performance across the entire heat flux range compared to bare sample without holes (No.20). However, the least performing coated sample (No.11) does show reasonable degradation in terms of heat transfer coefficient at high heat flux levels (>150 kW/m^2), although with slight delay in CHF. The coated sample (No. 3) demonstrates best overall performance compared to all tested surfaces. It shows dramatic improvement in the boiling heat transfer coefficients, compared to smooth surfaces, that is consistently high across the heat flux range. Synergistically, it also demonstrates remarkable 181% and 170% enhancement in CHF respectively compared to smooth surfaces without holes and with holes. At low heat fluxes, bubble nucleation on the cold-sprayed surfaces occurs earlier compared to that of smooth surfaces, which can be attributed to the increased density of possible nucleation sites provided by the multi-scale roughness generated during cold spraying. Table 3 summarizes CHF values obtained for all samples along with their enhancement relative to the smooth surface w/o holes. As seen from the table, all cold-sprayed surfaces outperformed the untreated smooth surface (No. 20, CHF = 233.78 kW/m^2) in terms of CHF, with enhancement ranging from 109.73% to 181.05%. Among them, sample No. 03 (P0.5–D1.0–1) exhibited the highest CHF of 423.27 kW/m^2, corresponding to the most pronounced performance improvement. In contrast, sample No. 11 (P1.0–D1.5–1) yielded the lowest CHF of 256.55 kW/m^2, with an enhancement of 109.73%. It is noteworthy that the smooth sample with holes (No. 19) achieved only ~7% CHF enhancement confirming the dramatic and standalone effect of multiscale coating formed on pre-drilled surfaces via cold spray technique on CHF improvement.

In summary, the hole-array coatings produced by cold spray markedly enhanced pool boiling performance, characterized by earlier onset of nucleate boiling, and higher heat transfer coefficients and CHF., demonstrating their clear advantage for boiling heat transfer enhancement.

5.3.3 Bubble behavior during the boiling process

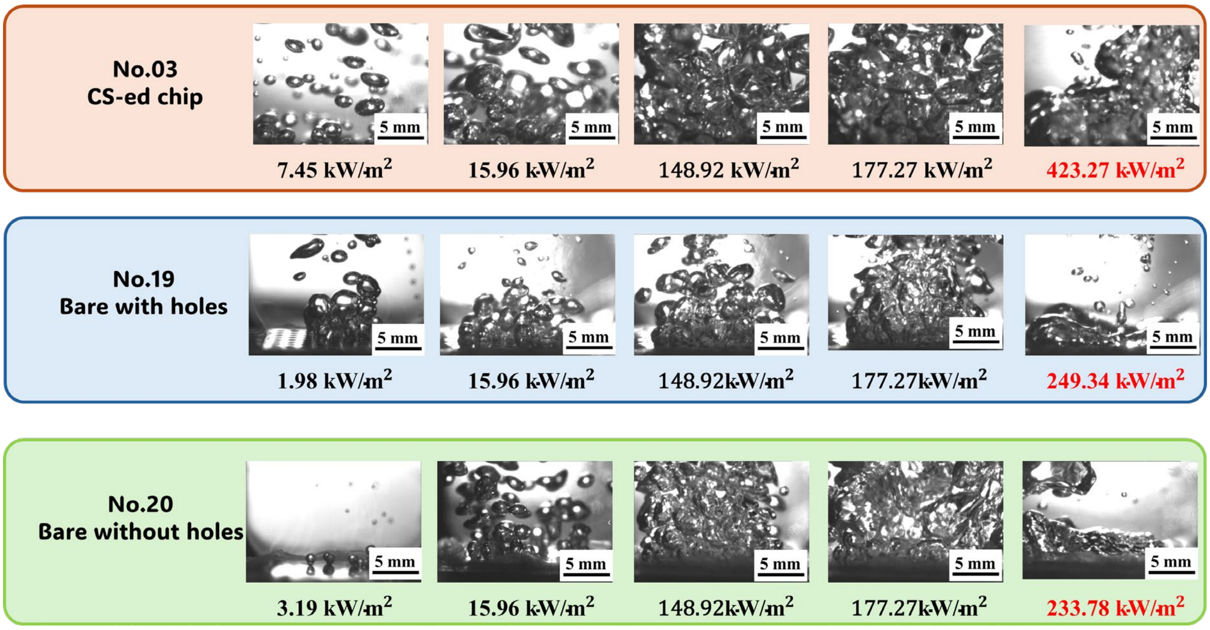

Figure. 48 Bubble behaviour during boiling at different heat flux levels

To gain a more intuitive understanding of the effect of surface morphology on bubble dynamics and boiling heat transfer performance, photographic images of boiling process, recorded via high speed imaging system, are shown in Fig. 48 for three representative samples at different heat flux conditions. These samples include cold-sprayed surface (No. 03), drilled but uncoated reference surface (No. 19), and untreated smooth aluminum substrate (No. 20). For each sample, typical bubble behaviors are observed at low, medium, and high heat flux up to CHF. The overall boiling evolution seems similar across all surfaces, with the dynamics transitioning sequentially through onset of nucleate boiling (ONB), isolated bubble regime, vapor column formation, and finally mushroom-shaped vapor cloud generation near CHF. The corresponding videos are provided in the Supplementary Material.

For the cold-sprayed sample (No. 03)which exhibited the highest CHF in the present study, extensive bubble nucleation, growth, and departure activities are observed at a heat flux as low as 7.45 kW/m^2, indicating a significantly advanced onset of nucleate boiling (ONB). With increasing heat flux, the frequency of bubble generation intensifies, and large, isolated vapor bubbles begin to form and detach from individual holes. Each hole effectively serves as a distinct macroscopic (primary) nucleation site, promoting stable and sustained vapor generation.

As the heat flux increased further, the frequency of bubble departure rises to the extent that vertical coalescence of successive bubbles at a given hole leads to the formation of vapor column at each primary nucleation site. The crest-like deposited regions around the holes acts as structural barriers, impeding horizontal coalescence between neighbouring primary bubbles. A slightly elevated nucleation activity on the deposited surface is also noted, characterized by the departure of small, isolated bubbles that fail to merge with the vapor columns.

Upon approaching CHF, consistent with Zuber's hydrodynamic instability theory, when the superficial vapor velocity within the vapor columns approaches that of the counterflowing liquid columns, it triggers hydrodynamic instability, resulting in CHF at 423.27 kW/m^2. At this stage, a characteristic mushroom-shaped vapor cloud emerges due to intensified interactions among vapor columns, marking the onset of CHF and the associated loss of surface rewetting capability.

In case of pre-treated smooth surface (No. 19), following major differences in boiling dynamics are observed relative to the pretreated and coated surface (No. 03). At low heat flux levels, bubble coverage area on the surface is less and it gradually expands on the surface with increasing heat flux. Additionally, it is observed that the secondary vapor generation via microscopic bubbles formation around hole regions was less pronounced. Importantly, unlike surface no 03, this surface shows frequent lateral coalescences between adjacent large bubbles, mainly due to the absence of effective structural barriers around the holes (primary nucleation sites). Lateral vapor spreading causes local hot spots, which eventually grow irreversibly and triggers early onset of CHF. As a result, this surface exhibits significantly lower boiling heat transfer intensity and CHF.

The untreated smooth surface (No. 20) shows weakest boiling activity at low heat flux. Sporadic bubbles are observed at 3.19 kW/m^2, and even at 15.96 kW/m^2, only small portion of the surface exhibits continuous vapor generation process. At this stage, small isolated bubbles are observed leaving the surface with relatively low departure frequency compared to that of other samples. Consequently, whole surface shows intensified vapor generation and its transport to bulk liquid, showing increasing bubbles interaction in lateral and vertical directions with increasing heat flux. This is followed by formation of large unstable vapor agglomerations, which eventually grow irreversibly, triggering CHF at 233.78 kW/m². At this stage, severe vapor blanketing covers entire surface, resulting in significant deterioration of heat transfer performance.

Overall, the results demonstrate that the pre-treated cold spray coated surfaces facilitate earlier bubble nucleation, faster bubble departure, and effective suppression of lateral vapor spreading., thereby simultaneously enhancing heat transfer intensity and CHF. This further highlight the strong potential of cold sprayed coatings on pre-treated surfaces in regulating bubble dynamics, enhancing boiling performance, and delaying critical heat flux conditions.

5.3.4 Influence of parameters

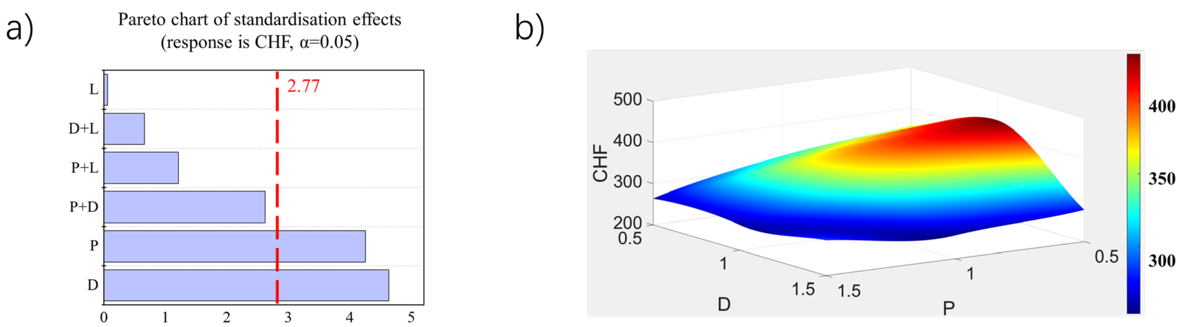

Figure. 49 Standardized Pareto chart and response surface analysis of the effects of hole diameter (D), Pitch (P), and coating layer number on CHF

Fig. 49 illustrates the standardized Pareto chart of the main factors and their interaction terms with CHF (critical heat flux) as the response variable. The red dashed line denotes the significance threshold of 2.776, corresponding to a significance level of $\alpha = 0.05$, which was used to determine whether a factor exerts a statistically significant effect. Factors with standardized effects exceeding this threshold are regarded as significant and should be emphasized in process optimization, whereas those below the threshold contribute only marginally and may be simplified.

From the figure, it can be observed that the main factors Diameter and Pitch exhibit standardized effects of approximately 4.7 and 4.2, both substantially higher than the reference line, indicating that these two geometric parameters play dominant roles in influencing CHF. In contrast, the factor Layer shows a standardized effect far below 2.776

and nearly approaches zero, suggesting that its contribution to CHF is negligible under the present processing conditions. Whether a single or double deposition layer was applied, the minor changes in surface morphology were insufficient to cause noticeable differences in boiling performance. Therefore, this parameter should not be treated as a key variable in subsequent designs or practical applications.

Specifically, Diameter exerts the strongest effect, underscoring the critical role of hole size in regulating bubble nucleation, departure, and liquid rewetting. An appropriate hole size provides a sufficiently large vapor–liquid interface and bubble growth space, thereby enhancing evaporation and delaying the onset of dryout. The effect of Pitch is also significant. As shown in Fig. 48, the combined influence of Diameter and Pitch on CHF is visualized using a three-dimensional response surface. The surface exhibits pronounced nonlinearity, indicating that CHF does not vary monotonically with either parameter alone, but is instead governed by their coupled interactions.

It can be further observed that when Diameter and Pitch are simultaneously set to intermediate levels (D = 1.0 mm, P = 0.5 mm), CHF reaches a maximum value exceeding 500 kW/m^2, corresponding to excellent boiling performance. This result is consistent with the Pareto analysis, which identified Diameter and Pitch as the significant factors. A moderate hole diameter provides sufficiently large cavities for vapor core formation and departure, while avoiding the disadvantages of undersized holes that hinder rewetting or oversized holes that weaken capillary supply. Meanwhile, an appropriate hole spacing helps maintain capillary-fed liquid supply channels within the hole array and prevents vapor coalescence or flow blockage caused by bubble interference.

In summary, CHF enhancement is primarily controlled by the geometric hole parameters, and optimizing the combination of hole diameter and hole spacing represents the most effective pathway to improving boiling performance. In contrast, deposition layer number can be simplified, provided that the basic coating quality is ensured.

5.4 Comparison with other additive enhancement techniques

Table. 7 summarizes several recent studies that employed additive manufacturing techniques to enhance boiling heat transfer performance, and compares their results with those obtained in the present work. It can be observed that, although various AM methods have achieved notable improvements in CHF, the hole-array aluminum coatings fabricated by cold spraying in this study delivered a far more pronounced enhancement, with the maximum CHF increase reaching 183%, significantly exceeding previously reported values.

It is also noteworthy that, compared with other AM processes, cold spraying not only offers high deposition efficiency but is also readily adaptable to a wide range of geometries, from flat to curved surfaces, thereby exhibiting excellent industrial compatibility. These results highlight the superior performance and broad application potential of cold spray technology in the field of boiling heat transfer enhancement.

Table.7 Comparison with other researchs

Research	CHF Improvement	Process Method	Ref
This research	183%	Cold Spray	
Yan et al.	161%	Cold Spray	[213]
R.J. MacNamara et al.	135%	Cold Spray	[214]
Donghwi Lee et al.	-11.6%	Cold Spray	[215]
Ahmed Elkholy et al.	120%	3D Printing	[216]
Leymus Yong Xiang Lum et al.	-40%	Selective Laser Melting	[217]
Houli Liu	140%	Selective Laser Melting	[218]

5.4 Summary

This study addresses the enhancement of pool boiling heat transfer at the engineering scale and proposes and validates a multiscale surface structuring strategy based on the integration of pre fabricated pore arrays with cold spray solid state deposition.

Functionalized coatings combining periodic pore structures and micron scale particle roughness were successfully constructed on aluminum substrates. Their morphological characteristics, boiling heat transfer behavior, and enhancement mechanisms were systematically analyzed. The results demonstrate that this approach achieves significant heat transfer improvement while maintaining process simplicity and industrial scalability. The main conclusions are summarized as follows.

1. Cold spray deposition exhibits high fidelity in replicating pre machined pore arrays. After deposition, key geometric parameters such as pore diameter and pore spacing remain stable, while particle accumulation significantly increases pore wall roughness, forming a multiscale surface architecture that integrates macroscopic order with microscopic roughness.
2. The pore array cold sprayed surfaces markedly reduce the onset superheat of nucleate boiling to a minimum of approximately 2.74 K, which is substantially lower than the 7.37 K required for the smooth substrate, indicating effective promotion of early nucleation.
3. In the high heat flux regime, the maximum critical heat flux reaches 423.27 kW m^{-2}, representing a 183 percent enhancement compared with the smooth substrate. The performance is also significantly superior to that of substrates with drilled pores alone, demonstrating a strong synergistic effect between geometric structuring and surface roughness.
4. High speed imaging reveals that the periodic pore geometry provides stable primary nucleation sites, while the rough pore walls increase effective nucleation site density. The solid ridges between pores suppress lateral bubble coalescence and delay dry spot propagation, thereby postponing hydrodynamic instability and increasing critical heat flux.
5. Orthogonal design and response surface analysis indicate that pore diameter and pore spacing are the dominant parameters governing critical heat flux, with effects significantly greater than that of the number of sprayed layers. Within the investigated range, coating thickness has a minor influence on critical heat flux. Optimal performance is achieved with intermediate pore diameter combined with relatively small pore spacing.

Overall, this study establishes a cold spray based pore array enhancement pathway that combines structural controllability with manufacturing feasibility, providing a new technical approach for the design of high efficiency boiling heat transfer surfaces at the engineering scale. Future work should focus on quantitative investigation of bubble generation frequency, departure dynamics, and effective nucleation site density to further advance the understanding of multiscale structure enhanced boiling mechanisms.

Chapter 6 Conclusion and prospects

6.1 Conclusion

This dissertation presents a systematic investigation into the formation mechanisms, structural controllability, and boiling heat transfer functionality of surface open pore structures generated during cold spray solid state additive manufacturing. The study establishes a complete research loop consisting of material driven pore formation, mechanistic elucidation, functional validation, mechanism extension, geometrically controlled design, and performance revalidation.

First, using Ti64 as a model material, a cold sprayed deposit exhibiting intrinsic surface open pore characteristics was successfully fabricated. Experimental observations demonstrate that a stable open pore network can form directly during the cold spray process on Ti64 surfaces. Cross sectional analysis and three dimensional reconstruction confirm that these pores are not isolated closed defects but through thickness channels directly connected to the external surface, thereby providing a structural foundation for subsequent heat transfer applications.

On this basis, the formation mechanism of the surface open pore structure was systematically elucidated. The results indicate that, even under constant macroscopic spraying parameters, particle velocities at the nozzle exit are not unique but exhibit pronounced dispersion due to combined variations in powder particle size, morphology, and density. A fraction of particles possesses velocities below the critical threshold required for effective deposition and therefore undergo rebound or extremely low deposition efficiency during the initial deposition stage, resulting in persistently low efficiency regions on the surface. As multilayer deposition proceeds, this initial non-uniformity is continuously inherited and amplified. Regions with high deposition efficiency evolve into wall like structures that support particle accumulation, whereas low efficiency regions ultimately develop into open pore channels penetrating the entire deposit thickness. These findings demonstrate that surface open pore formation in cold sprayed Ti64 fundamentally originates from selective deposition behavior during the initial stage rather than from the late stage evolution of random defects.

After clarifying the formation mechanism, the porous Ti64 surface was further evaluated as a functional material using pool boiling heat transfer as a performance assessment platform. The experimental results show that, compared with smooth substrates, cold sprayed porous Ti64 surfaces significantly reduce the wall superheat required for bubble nucleation and markedly enhance boiling heat transfer performance in the medium to high heat flux regime. Under optimal conditions, the critical heat flux exhibits an improvement of up to 60 percent relative to the smooth substrate. High speed imaging reveals that this enhancement arises from stable primary nucleation sites provided by the open pores, high density micro nucleation induced by rough pore walls, and effective suppression of lateral bubble coalescence by the solid ridges between pores, which collectively delay the onset of local dryout.

However, the study also reveals that the relatively low thermal conductivity of Ti64 leads to increasing additional thermal resistance with greater deposit thickness, thereby limiting further enhancement of boiling performance. This finding indicates that porous structures formed solely through intrinsic material deposition behavior exhibit inherent limitations in structural controllability and functional optimization.

Based on these insights, the identified mechanism of low deposition efficiency induced pore formation was extended from the Ti64 system to aluminum based substrates. By pre fabricating regular geometric features on aluminum surfaces to deliberately create regions unfavorable for effective deposition, low deposition efficiency zones analogous to those naturally formed in Ti64 were reproduced in a high deposition efficiency material system. Experimental results demonstrate that this geometry driven pore formation strategy enables the stable fabrication of regular and highly repeatable surface open pore structures on cold sprayed aluminum, with pore morphology closely matching the predefined geometric parameters. This confirms the material generality and design extensibility of the cold spray pore formation mechanism.

Subsequently, the boiling heat transfer performance of geometrically controlled aluminum based porous surfaces was systematically investigated. Orthogonal experimental design and statistical analysis reveal that pore diameter and pore spacing are the dominant parameters governing critical heat flux, with standardized effects significantly exceeding that of the number of deposited layers, while the influence of layer number on critical heat flux is negligible within the investigated parameter range. This result indicates that, provided basic coating integrity and surface roughness are ensured, effective boiling performance regulation primarily depends on appropriate geometric matching of pore structures. Under optimal conditions, the critical heat flux reaches up to 183 percent of that of a smooth surface. Response surface analysis further reveals a pronounced nonlinear coupling between pore diameter and pore spacing, with optimal critical heat flux achieved at intermediate pore diameters combined with relatively small pore spacing. The resulting performance substantially exceeds that of simple drilled substrates and other additive manufacturing based enhancement strategies.

In summary, starting from the natural formation of surface open pore structures in cold sprayed Ti64, this dissertation systematically elucidates the underlying mechanisms and successfully extends them into a geometrically controllable and material transferable surface pore fabrication strategy. By employing pool boiling heat transfer as a highly sensitive and quantitatively assessable validation platform, the study not only deepens the understanding of the relationship between deposition non-uniformity and porous structure evolution in cold spray processes but also provides new theoretical insights and engineering pathways for the design and fabrication of porous functional surfaces in solid state additive manufacturing.

6.2 Further work

Although this dissertation systematically elucidates the formation mechanisms of surface open pore structures generated by cold spray deposition and verifies their significant heat transfer enhancement through pool boiling experiments, the preceding research also establishes a broader structure–function framework that provides clear directions for further investigation.

First, at the mechanistic level, it is necessary to advance from qualitative observation to quantitative modeling. While high speed imaging in this study revealed the critical role of open pore structures in promoting nucleation, accelerating bubble departure, and suppressing lateral coalescence, the analysis remains largely phenomenological. Future work should systematically quantify key parameters, including bubble nucleation frequency, departure diameter, departure period, and effective nucleation site density, and examine their evolution with heat flux and pore geometry. By integrating experimental measurements with classical boiling models and hydrodynamic instability theories, quantitative relationships between pore geometric parameters and bubble dynamic behavior can be established, thereby significantly improving the rigor and predictive capability of mechanistic interpretation.

Second, from a structural design perspective, the present study reveals a distinct scale division effect. Small pores are more favorable for bubble nucleation and rapid departure, whereas larger pore walls play a critical role in restricting lateral vapor spreading and suppressing bubble coalescence. This finding suggests that a single scale pore structure is unlikely to simultaneously optimize bubble generation and vapor regulation. Therefore, future research may consider constructing hierarchical pore array structures composed of large and small pores through substrate pre machining prior to cold spray deposition. Larger pores may function as vapor management units, while smaller pores serve as high density primary nucleation sites. Subsequent cold spray deposition can faithfully replicate the predefined geometry and introduce microscale roughness on pore walls, enabling synergistic enhancement through geometric scale coordination and surface roughness modification. Such hierarchical architectures are expected to enhance nucleation efficiency while delaying large scale vapor coverage, thereby further increasing critical heat flux.

Third, regarding material system expansion, although the pore structuring strategy has been successfully extended from Ti64 to aluminum based substrates, the thermal conductivity of aluminum may still impose limitations under extremely high heat flux conditions. Future studies may extend the geometry driven pore structuring approach to copper and copper alloy systems. Owing to their higher thermal conductivity and superior lateral heat diffusion capability, copper based materials are expected to further reduce solid side thermal resistance under identical pore geometries, thereby improving overall heat transfer capacity. In addition, copper based materials possess direct engineering relevance in electronic packaging and high power device thermal management, facilitating the practical implementation of cold spray fabricated porous functional surfaces.

In summary, future research should focus on quantitative modeling of bubble dynamics, hierarchical pore structure design, and extension to high thermal conductivity material systems. These directions will not only deepen the understanding of boiling enhancement mechanisms associated with cold spray induced surface open pore structures, but also promote the transition from mechanistic validation toward structural optimization and practical engineering application, ultimately establishing a more comprehensive and transferable technological framework.

Reference

[1] X. Fan *et al.*, “Intermetallics Enhanced strength-ductility synergy in cold-sprayed CoCrFeNi-Ti high-entropy alloys via integrated post-processing strategy,” *Intermetallics*, vol. 188, no. September 2025, p. 109047, 2026, doi: 10.1016/j.intermet.2025.109047.

[2] Q. Wang and M. X. Zhang, “Review on recent research and development of cold spray technologies,” *Key Eng. Mater.*, vol. 533, pp. 1–52, 2013, doi: 10.4028/www.scientific.net/KEM.533.1.

[3] W. Sun, X. Chu, H. Lan, R. Huang, and J. Huang, “Current Implementation Status of Cold Spray Technology : A Short Review,” *J. Therm. Spray Technol.*, vol. 31, no. 4, pp. 848–865, 2022, doi: 10.1007/s11666-022-01382-4.

[4] R. C. Dykhuizen and M. F. Smith, “Gas Dynamic Principles of Cold Spray,” vol. 7, no. June, pp. 205–212, 1998.

[5] W. Li, C. Cao, and S. Yin, “Solid-state cold spraying of Ti and its alloys: A literature review,” *Prog. Mater. Sci.*, vol. 110, no. December 2019, p. 100633, 2020, doi: 10.1016/j.pmatsci.2019.100633.

[6] A. Srikanth, M. Thalib, G. Basha, and B. Venkateshwarlu, “ScienceDirect A Brief Review on Cold Spray Coating Process,” *Mater. Today Proc.*, vol. 22, pp. 1390–1397, 2020, doi: 10.1016/j.matpr.2020.01.482.

[7] G. N. Devi, S. K. Nitin, and P. W. Anjali, “Impact of Initial Feedstock on Corrosion Behavior of Cold- Sprayed Nickel Coatings,” *J. Therm. Spray Technol.*, 2026, doi: 10.1007/s11666-025-02149-3.

[8] Y. Wang, Y. Wu, Z. Wei, J. Lv, S. Hong, and J. Cheng, “Intermetallics Phase evolution and nanomechanical characteristics of cold-sprayed Cu-based amorphous coatings,” *Intermetallics*, vol. 188, no. October 2025, p. 109063, 2026, doi: 10.1016/j.intermet.2025.109063.

[9] T. Schmidt, F. Gaertner, and H. Kreye, “New Developments in Cold Spray Based on Higher Gas and Particle Temperatures,” vol. 15, no. December, pp. 488–494, 2006, doi: 10.1361/105996306X147144.

[10] S. Marx, A. Paul, A. Köhler, and G. Hüttl, “Cold Spraying : Innovative Layers for New Applications,” vol. 15, no. June, pp. 177–183, 2006, doi:

10.1361/105996306X107977.

[11] M. R. R. S. R. Nutt and C. A. W. V. K. Champagne, "Review of Relationship Between Particle Deformation , Coating Microstructure , and Properties in High-Pressure Cold Spray," *J. Therm. Spray Technol.*, vol. 26, no. 6, pp. 1308–1355, 2017, doi: 10.1007/s11666-017-0575-0.

[12] R. F. Vaz, A. Garfias, V. Albaladejo, J. Sanchez, and I. G. Cano, "A Review of Advances in Cold Spray Additive Manufacturing," 2023.

[13] S. Yin, M. Meyer, W. Li, H. Liao, and R. Lupoi, "Gas Flow, Particle Acceleration, and Heat Transfer in Cold Spray: A review," *J. Therm. Spray Technol.*, vol. 25, no. 5, pp. 874–896, 2016, doi: 10.1007/s11666-016-0406-8.

[14] N. N. Bayon *et al.*, "Synthesis and characterization of titanium nitride nanoparticles," *Mater. Express*, vol. 12, no. 9, pp. 1211–1215, 2022, doi: 10.1166/mex.2022.2241.

[15] S. Singh, R. K. S. Raman, C. C. Berndt, and H. Singh, "Influence of Cold Spray Parameters on Bonding Mechanisms : A Review," 2021.

[16] Y. Xiong *et al.*, "Enhancing strength and ductility in Ti64 Alloys: Optimizing dual-phase heterostructures and TRIP effects via high-entropy alloy content modulation," *Mater. Des.*, vol. 257, no. April, p. 114399, 2025, doi: 10.1016/j.matdes.2025.114399.

[17] Y. Xiong *et al.*, "Achieving superior strength-ductility combination in the heterogeneous microstructured Ti64 alloy via multi-eutectoid elements alloying with CoCrFeNiMn during laser powder bed fusion," *Virtual Phys. Prototyp.*, vol. 19, no. 1, 2024, doi: 10.1080/17452759.2024.2375106.

[18] J. Ge, J. Lin, Y. Chen, Y. Lei, and H. Fu, "Characterization of wire arc additive manufacturing 2Cr13 part: Process stability, microstructural evolution, and tensile properties," *J. Alloys Compd.*, vol. 748, pp. 911–921, 2018, doi: 10.1016/j.jallcom.2018.03.222.

[19] H. Liu *et al.*, "An Investigation on Microstructural Characteristics and Comprehensive Performances of Equiatomic Ratio NiTi Shape-Memory Alloy Produced by Selective Laser Melting," *Adv. Eng. Mater.*, vol. 2401245, pp. 1–12, 2024, doi: 10.1002/adem.202401245.

[20] Y. Xiong *et al.*, "A novel composites of laser 3D printed CoCrFeNiMn/Ti6Al4V

lattice structure with B4C/AlSi10Mg interpenetrating phases," *Compos. Part A Appl. Sci. Manuf.*, vol. 188, no. September 2024, p. 108579, 2025, doi: 10.1016/j.compositesa.2024.108579.

[21] J. P. Kruth, P. Mercelis, J. Van Vaerenbergh, L. Froyen, and M. Rombouts, "Binding mechanisms in selective laser sintering and selective laser melting," *Rapid Prototyp. J.*, vol. 11, no. 1, pp. 26–36, 2005, doi: 10.1108/13552540510573365.

[22] L. E. Murr *et al.*, "Invited Review Metal Fabrication by Additive Manufacturing Using Laser and Electron Beam Melting Technologies," *J. Mater. Sci. Technol.*, vol. 28, no. 1, pp. 1–14, 2012, doi: 10.1016/S1005-0302(12)60016-4.

[23] J. Meijer, "Laser beam machining (LBM), state of the art and new opportunities," vol. 149, pp. 2–17, 2004, doi: 10.1016/j.jmatprotec.2004.02.003.

[24] A. K. Dubey and V. Y. Ã, "Laser beam machining — A review," vol. 48, pp. 609–628, 2008, doi: 10.1016/j.ijmachtools.2007.10.017.

[25] L. Yan, Y. Chen, and F. Liou, "Additive manufacturing of functionally graded metallic materials using laser metal deposition," *Addit. Manuf.*, vol. 31, no. August 2019, p. 100901, 2020, doi: 10.1016/j.addma.2019.100901.

[26] C. Zhong, J. Liu, T. Zhao, T. Schopphoven, and J. Fu, "applied sciences Laser Metal Deposition of Ti6Al4V — A Brief Review," pp. 1–12, 2020, doi: 10.3390/app10030764.

[27] M. Ghasempour-mouziraji, J. Lagarinhos, and D. Afonso, "A review study on metal powder materials and processing parameters in Laser Metal Deposition," *Opt. Laser Technol.*, vol. 170, no. August 2023, p. 110226, 2024, doi: 10.1016/j.optlastec.2023.110226.

[28] S. V Klinkov and V. F. Kosarev, "Measurements of Cold Spray Deposition Efficiency," vol. 15, no. September, pp. 364–371, 2006, doi: 10.1361/105996306X124365.

[29] A. M. Vilardell, N. Cinca, A. Concustell, S. Dosta, I. G. Cano, and J. M. Guilemany, "Cold spray as an emerging technology for biocompatible and antibacterial coatings: state of art," *J. Mater. Sci.*, vol. 50, no. 13, pp. 4441–4462, 2015, doi: 10.1007/s10853-015-9013-1.

[30] X. He, F. Gu, and A. Ball, "Progress in Materials Science A review of numerical

analysis of friction stir welding," *Prog. Mater. Sci.*, vol. 65, pp. 1–66, 2014, doi: 10.1016/j.pmatsci.2014.03.003.

[31] S. Kumar and A. Kar, "A Review of Solid-State Additive Manufacturing Processes," *Trans. Indian Natl. Acad. Eng.*, vol. 6, no. 4, pp. 955–973, 2021, doi: 10.1007/s41403-021-00270-7.

[32] H. Singh, M. Kumar, and R. Singh, "Materials Today : Proceedings An overview of various applications of cold spray coating process," *Mater. Today Proc.*, vol. 56, pp. 2826–2830, 2022, doi: 10.1016/j.matpr.2021.10.160.

[33] X. Luo, C. Li, F. Shang, G. Yang, Y. Wang, and C. Li, "Surface & Coatings Technology High velocity impact induced microstructure evolution during deposition of cold spray coatings : A review," *Surf. Coat. Technol.*, vol. 254, pp. 11–20, 2014, doi: 10.1016/j.surfcoat.2014.06.006.

[34] S. Yin, P. Cavaliere, B. Aldwell, R. Jenkins, H. Liao, and W. Li, "Cold spray additive manufacturing and repair : Fundamentals and applications," *Addit. Manuf.*, vol. 21, no. August 2017, pp. 628–650, 2018, doi: 10.1016/j.addma.2018.04.017.

[35] T. Van Steenkiste and J. R. Smith, "Evaluation of Coatings Produced via Kinetic and Cold Spray Processes," vol. 13, no. June, pp. 274–282, 2004, doi: 10.1361/10599630419427.

[36] L. He and M. Hassani, *A Review of the Mechanical and Tribological Behavior of Cold Spray Metal Matrix Composites*, vol. 29, no. 7. Springer US, 2020. doi: 10.1007/s11666-020-01091-w.

[37] R. Article *et al.*, "An overview of cold spray coating in additive manufacturing , component repairing and other engineering applications," pp. 514–534, 2022.

[38] E. Irissou, J. G. Legoux, A. N. Ryabinin, B. Jodoin, and C. Moreau, "Review on cold spray process and technology: Part I - Intellectual property," *J. Therm. Spray Technol.*, vol. 17, no. 4, pp. 495–516, 2008, doi: 10.1007/s11666-008-9203-3.

[39] Dachlan 2014:1, "Modern Cold Spray: Materials, Process, and Applications," *Angew. Chemie Int. Ed. 6(11), 951–952.*, pp. 22–31, 2014.

[40] V. F. Kosarev, S. V. Klinkov, A. P. Alkhimov, and A. N. Papyrin, "On some aspects of gas dynamics of the cold spray process," *J. Therm. Spray Technol.*, vol. 12, no. 2, pp. 265–281, 2003, doi: 10.1361/105996303770348384.

[41] H. Yeom and K. Sridharan, "Annals of Nuclear Energy Cold spray technology in

nuclear energy applications : A review of recent advances," *Ann. Nucl. Energy*, vol. 150, p. 107835, 2021, doi: 10.1016/j.anucene.2020.107835.

[42] V. Champagne and D. Helfritch, "The unique abilities of cold spray deposition," *Int. Mater. Rev.*, vol. 61, no. 7, pp. 437–455, 2016, doi: 10.1080/09506608.2016.1194948.

[43] T. Schmidt, F. Gärtner, H. Assadi, and H. Kreye, "Development of a generalized parameter window for cold spray deposition," *Acta Mater.*, vol. 54, no. 3, pp. 729–742, 2006, doi: 10.1016/j.actamat.2005.10.005.

[44] M. Faizan, U. Rab, S. Zahiri, S. H. Masood, M. Jahedi, and R. Nagarajah, "Development of 3D Multicomponent Model for Cold Spray Process Using Nitrogen and Air," pp. 688–708, 2015, doi: 10.3390/coatings5040688.

[45] J. Wu, H. Fang, S. Yoon, H. Kim, and C. Lee, "The rebound phenomenon in kinetic spraying deposition," *Scr. Mater.*, vol. 54, no. 4 SPEC. ISS., pp. 665–669, 2006, doi: 10.1016/j.scriptamat.2005.10.028.

[46] J. Wu, H. Fang, S. Yoon, C. Lee, and H. J. Kim, "Critical velocities for high speed particle deposition in kinetic spraying," *Mater. Trans.*, vol. 47, no. 7, pp. 1723–1727, 2006, doi: 10.2320/matertrans.47.1723.

[47] T. Liao *et al.*, "Progress in Surface Science Multifunctional cold spray coatings for biological and biomedical applications : A review," *Prog. Surf. Sci.*, vol. 97, no. 2, p. 100654, 2022, doi: 10.1016/j.progsurf.2022.100654.

[48] M. A. A. Nyiak and A. A. Tiamiyu, "Recent advances on bonding mechanism in cold spray process : A review of single - particle impact methods," *J. Mater. Res.*, vol. 38, no. 1, pp. 69–95, 2023, doi: 10.1557/s43578-022-00764-2.

[49] S. Yin *et al.*, "Towards high-strength cold spray additive manufactured metals: Methods, mechanisms, and properties," *J. Mater. Sci. Technol.*, vol. 170, pp. 47–64, 2024, doi: 10.1016/j.jmst.2023.05.047.

[50] S. Chalivendra, "A Review of Advances in Cold Spray Coating Process," pp. 53–62, 2024.

[51] P. Richer, B. Jodoin, L. Ajdelsztajn, and E. J. Lavernia, "Substrate Roughness and Thickness Effects on Cold Spray Nanocrystalline Al-Mg Coatings," vol. 15, no. June, pp. 246–254, 2006, doi: 10.1361/105996306X108174.

[52] H. Assadi, H. Kreye, F. Gärtner, and T. Klassen, "Cold spraying – A materials

perspective," *Acta Mater.*, vol. 116, pp. 382–407, 2016, doi: 10.1016/j.actamat.2016.06.034.

[53] T. S. Price, P. H. Shipway, and D. G. Mccartney, "Effect of Cold Spray Deposition of a Titanium Coating on Fatigue Behavior of a Titanium Alloy," vol. 15, no. December, pp. 507–512, 2006, doi: 10.1361/105996306X147108.

[54] F. Gärtner, T. Schmidt, T. Stoltenhoff, and H. Kreye, "Recent developments and potential applications of cold spraying," *Adv. Eng. Mater.*, vol. 8, no. 7, pp. 611–618, 2006, doi: 10.1002/adem.200600048.

[55] E. Science, "On the Characteristics of Cold Spray Technology and Its Application in Aerospace Industries On the Characteristics of Cold Spray Technology and Its Application in Aerospace Industries", doi: 10.1088/1755-1315/719/3/032023.

[56] T. H. V. Steenkiste, J. R. Smith, and R. E. Teets, "Aluminum coatings via kinetic spray with relatively large powder particles," *Surf. Coatings Technol.*, vol. 154, no. 2–3, pp. 237–252, 2002, doi: 10.1016/S0257-8972(02)00018-X.

[57] M. Yu, W. Y. Li, F. F. Wang, and H. L. Liao, "Finite element simulation of impacting behavior of particles in cold spraying by Eulerian approach," *J. Therm. Spray Technol.*, vol. 21, no. 3–4, pp. 745–752, 2012, doi: 10.1007/s11666-011-9717-y.

[58] W. Y. Li and W. Gao, "Some aspects on 3D numerical modeling of high velocity impact of particles in cold spraying by explicit finite element analysis," *Appl. Surf. Sci.*, vol. 255, no. 18, pp. 7878–7892, 2009, doi: 10.1016/j.apsusc.2009.04.135.

[59] S. Yin *et al.*, "Deposition behavior of thermally softened copper particles in cold spraying," *Acta Mater.*, vol. 61, no. 14, pp. 5105–5118, 2013, doi: 10.1016/j.actamat.2013.04.041.

[60] P. C. King, S. H. Zahiri, and M. Jahedi, "Focused ion beam micro-dissection of cold-sprayed particles," *Acta Mater.*, vol. 56, no. 19, pp. 5617–5626, 2008, doi: 10.1016/j.actamat.2008.07.034.

[61] G. Bae, J. Il Jang, and C. Lee, "Correlation of particle impact conditions with bonding, nanocrystal formation and mechanical properties in kinetic sprayed nickel," *Acta Mater.*, vol. 60, no. 8, pp. 3524–3535, 2012, doi: 10.1016/j.actamat.2012.03.001.

[62] M. Grujicic, J. R. Saylor, D. E. Beasley, W. S. DeRosset, and D. Helfritch,

"Computational analysis of the interfacial bonding between feed-powder particles and the substrate in the cold-gas dynamic-spray process," *Appl. Surf. Sci.*, vol. 219, no. 3–4, pp. 211–227, 2003, doi: 10.1016/S0169-4332(03)00643-3.

[63] K. H. Kim, W. Li, and X. Guo, "Detection of oxygen at the interface and its effect on strain, stress, and temperature at the interface between cold sprayed aluminum and steel substrate," *Appl. Surf. Sci.*, vol. 357, pp. 1720–1726, 2015, doi: 10.1016/j.apsusc.2015.10.022.

[64] Y. Xiong, K. Kang, G. Bae, S. Yoon, and C. Lee, "Dynamic amorphization and recrystallization of metals in kinetic spray process," *Appl. Phys. Lett.*, vol. 92, no. 19, pp. 4–7, 2008, doi: 10.1063/1.2928218.

[65] G. Bae *et al.*, "Bonding features and associated mechanisms in kinetic sprayed titanium coatings," *Acta Mater.*, vol. 57, no. 19, pp. 5654–5666, 2009, doi: 10.1016/j.actamat.2009.07.061.

[66] G. Bae, Y. Xiong, S. Kumar, K. Kang, and C. Lee, "General aspects of interface bonding in kinetic sprayed coatings," *Acta Mater.*, vol. 56, no. 17, pp. 4858–4868, 2008, doi: 10.1016/j.actamat.2008.06.003.

[67] H. Assadi, F. Gärtner, T. Stoltenhoff, and H. Kreye, "Bonding mechanism in cold gas spraying," *Acta Mater.*, vol. 51, no. 15, pp. 4379–4394, 2003, doi: 10.1016/S1359-6454(03)00274-X.

[68] M. Grujicic, C. L. Zhao, W. S. DeRosset, and D. Helfritch, "Adiabatic shear instability based mechanism for particles/substrate bonding in the cold-gas dynamic-spray process," *Mater. Des.*, vol. 25, no. 8, pp. 681–688, 2004, doi: 10.1016/j.matdes.2004.03.008.

[69] W. Y. Li, C. Zhang, X. Guo, C. J. Li, H. Liao, and C. Coddet, "Study on impact fusion at particle interfaces and its effect on coating microstructure in cold spraying," *Appl. Surf. Sci.*, vol. 254, no. 2, pp. 517–526, 2007, doi: 10.1016/j.apsusc.2007.06.026.

[70] C. J. Li, W. Y. Li, and Y. Y. Wang, "Formation of metastable phases in cold-sprayed soft metallic deposit," *Surf. Coatings Technol.*, vol. 198, no. 1-3 SPEC. ISS., pp. 469–473, 2005, doi: 10.1016/j.surfcoat.2004.10.063.

[71] S. Guetta *et al.*, "Influence of particle velocity on adhesion of cold-sprayed splats," *J. Therm. Spray Technol.*, vol. 18, no. 3, pp. 331–342, 2009, doi: 10.1007/s11666-

009-9327-0.
[72] K. H. Ko, J. O. Choi, and H. Lee, "The interfacial restructuring to amorphous: A new adhesion mechanism of cold-sprayed coatings," *Mater. Lett.*, vol. 175, pp. 13–15, 2016, doi: 10.1016/j.matlet.2016.03.132.
[73] V. K. Champagne, M. K. West, M. Reza Rokni, T. Curtis, V. Champagne, and B. McNally, "Joining of Cast ZE41A Mg to Wrought 6061 Al by the Cold Spray Process and Friction Stir Welding," *J. Therm. Spray Technol.*, vol. 25, no. 1–2, pp. 143–159, 2016, doi: 10.1007/s11666-015-0301-8.
[74] P. C. King, C. Busch, T. Kittel-Sherri, M. Jahedi, and S. Gulizia, "Interface melding in cold spray titanium particle impact," *Surf. Coatings Technol.*, vol. 239, pp. 191–199, 2014, doi: 10.1016/j.surfcoat.2013.11.039.
[75] K. Taylor, B. Jodoin, and J. Karov, "Particle Loading Effect in Cold Spray," vol. 15, no. June, pp. 273–279, 2006, doi: 10.1361/105996306X108237.
[76] S. An, B. Joshi, A. L. Yarin, M. T. Swihart, and S. S. Yoon, "Supersonic Cold Spraying for Energy and Environmental Applications : One-Step Scalable Coating Technology for Advanced Micro- and Nanotextured Materials," vol. 1905028, pp. 1–34, 2020, doi: 10.1002/adma.201905028.
[77] H. Koivuluoto, A. Coleman, K. Murray, M. Kearns, and P. Vuoristo, "High Pressure Cold Sprayed (HPCS) and Low Pressure Cold Sprayed (LPCS) Coatings Prepared from OFHC Cu Feedstock : Overview from Powder Characteristics to Coating Properties," vol. 21, no. September, pp. 1065–1075, 2012, doi: 10.1007/s11666-012-9790-x.
[78] R. Della Gatta, A. S. Perna, A. Viscusi, and A. Astarita, "Cold spray deposition of metallic coatings on polymers : a review," *J. Mater. Sci.*, vol. 57, no. 1, pp. 27–57, 2022, doi: 10.1007/s10853-021-06561-2.
[79] H. Parmar, "Metallisation of polymers and polymer matrix composites by cold spray : state of the art and research perspectives," vol. 67, no. 4, pp. 385–409, 2022, doi: 10.1080/09506608.2021.1954805.
[80] A. Nourian, T. Schwartz, S. Boese, and S. Mu, "Effects of Process Parameters on Cold Spray Deposition of Al-6061 Alloy," pp. 2517–2536, 2022, doi: 10.1007/s11666-022-01456-3.
[81] K. Malamousi, K. Delibasis, B. Allcock, and S. Kamnis, "Surface & Coatings

Technology Digital transformation of thermal and cold spray processes with emphasis on machine learning," *Surf. Coat. Technol.*, vol. 433, no. January, p. 128138, 2022, doi: 10.1016/j.surfcoat.2022.128138.

[82] M. Hassani-Gangaraj, D. Veysset, K. A. Nelson, and C. A. Schuh, "In-situ observations of single micro-particle impact bonding," *Scr. Mater.*, vol. 145, pp. 9–13, 2018, doi: 10.1016/j.scriptamat.2017.09.042.

[83] W. Y. Li, C. J. Li, and H. Liao, "Significant influence of particle surface oxidation on deposition efficiency, interface microstructure and adhesive strength of cold-sprayed copper coatings," *Appl. Surf. Sci.*, vol. 256, no. 16, pp. 4953–4958, 2010, doi: 10.1016/j.apsusc.2010.03.008.

[84] W. Y. Li, H. Liao, G. Douchy, and C. Coddet, "Optimal design of a cold spray nozzle by numerical analysis of particle velocity and experimental validation with 316L stainless steel powder," *Mater. Des.*, vol. 28, no. 7, pp. 2129–2137, 2007, doi: 10.1016/j.matdes.2006.05.016.

[85] A. Sova, S. Klinkov, V. Kosarev, N. Ryashin, and I. Smurov, "Preliminary study on deposition of aluminium and copper powders by cold spray micronozzle using helium," *Surf. Coatings Technol.*, vol. 220, pp. 98–101, 2013, doi: 10.1016/j.surfcoat.2012.09.036.

[86] J. Pattison, S. Celotto, A. Khan, and W. O'Neill, "Standoff distance and bow shock phenomena in the Cold Spray process," *Surf. Coatings Technol.*, vol. 202, no. 8, pp. 1443–1454, 2008, doi: 10.1016/j.surfcoat.2007.06.065.

[87] W. Y. Li *et al.*, "Effect of standoff distance on coating deposition characteristics in cold spraying," *Mater. Des.*, vol. 29, no. 2, pp. 297–304, 2008, doi: 10.1016/j.matdes.2007.02.005.

[88] C. J. Li, W. Y. Li, Y. Y. Wang, and H. Fukanuma, "Effect of spray angle on deposition characteristics in cold spraying," *Therm. spray*, pp. 91–96, 2003.

[89] S. Yin, X. Suo, J. Su, Z. Guo, H. Liao, and X. Wang, "Effects of substrate hardness and spray angle on the deposition behavior of cold-sprayed ti particles," *J. Therm. Spray Technol.*, vol. 23, no. 1–2, pp. 76–83, 2014, doi: 10.1007/s11666-013-0039-0.

[90] W. Wong, E. Irissou, A. N. Ryabinin, J. G. Legoux, and S. Yue, "Influence of helium and nitrogen gases on the properties of cold gas dynamic sprayed pure

titanium coatings," *J. Therm. Spray Technol.*, vol. 20, no. 1–2, pp. 213–226, 2011, doi: 10.1007/s11666-010-9568-y.

[91] A. Choudhuri, P. S. Mohanty, and J. Karthikeyan, "Bio-ceramic composite coatings by cold spray technology," in *Thermal Spray 2009. Proc. Int. Thermal Spray Conf*, 2009.

[92] W. Sun, A. W. Y. Tan, N. W. Khun, I. Marinescu, and E. Liu, "Effect of substrate surface condition on fatigue behavior of cold sprayed Ti6Al4V coatings," *Surf. Coatings Technol.*, vol. 320, pp. 452–457, 2017, doi: 10.1016/j.surfcoat.2016.11.093.

[93] S. Yin, X. Suo, H. Liao, Z. Guo, and X. Wang, "Significant influence of carrier gas temperature during the cold spray process," *Surf. Eng.*, vol. 30, no. 6, pp. 443–450, 2014, doi: 10.1179/1743294414Y.0000000276.

[94] R. Article *et al.*, "E ff ect of post - processing treatments on mechanical performance of cold spray coating – an overview," 2023.

[95] N. W. Khun, A. W. Y. Tan, K. J. W. Bi, and E. Liu, "Effects of working gas on wear and corrosion resistances of cold sprayed Ti-6Al-4V coatings," *Surf. Coatings Technol.*, vol. 302, pp. 1–12, 2016, doi: 10.1016/j.surfcoat.2016.05.052.

[96] B. Jodoin, S. Rahmati, R. G. A. Veiga, and A. Zu, "PEER REVIEWED A Numerical Approach to Study the Oxide Layer Effect on Adhesion in Cold Spray," pp. 1777–1791, 2021, doi: 10.1007/s11666-021-01245-4.

[97] R. Nikbakht, C. V Cojocaru, and M. Aghasibeig, "Cold Spray and Laser-Assisted Cold Spray of CrMnCoFeNi High Entropy Alloy Using Nitrogen as the Propelling Gas," pp. 1129–1142, 2022, doi: 10.1007/s11666-022-01361-9.

[98] T. Hussain, "Cold Spraying of Titanium: A Review of Bonding Mechanisms, Microstructure and Properties," *Key Eng. Mater.*, vol. 533, pp. 53–90, 2012, doi: 10.4028/www.scientific.net/kem.533.53.

[99] W. Wong, P. Vo, E. Irissou, A. N. Ryabinin, J. G. Legoux, and S. Yue, "Effect of particle morphology and size distribution on cold-sprayed pure titanium coatings," *J. Therm. Spray Technol.*, vol. 22, no. 7, pp. 1140–1153, 2013, doi: 10.1007/s11666-013-9951-6.

[100] S. Kumar, G. Bae, and C. Lee, "Influence of substrate roughness on bonding mechanism in cold spray," *Surf. Coatings Technol.*, vol. 304, pp. 592–605, 2016,

doi: 10.1016/j.surfcoat.2016.07.082.
[101] M. Fukumoto *et al.*, "Effect of substrate temperature on deposition behavior of copper particles on substrate surfaces in the cold spray process," *J. Therm. Spray Technol.*, vol. 16, no. 5–6, pp. 643–650, 2007, doi: 10.1007/s11666-007-9121-9.
[102] S. Kabir *et al.*, "Ultrasonic vibration-assisted laser directed energy deposition : effects on material movement in vertical and horizontal direction," 2026.
[103] C. L. Cramer, E. Cakmak, and S. S. Babu, "Preliminary hyperspectral neutron radiography of binder jet 3D printed and melt infiltrated Si – SiC," no. August 2025, pp. 1–10, 2026, doi: 10.1111/ijac.70109.
[104] Y. Zhang *et al.*, "Additive manufacturing of HA-TCP catalytic porous ceramics by stereolithography technology," vol. 347, no. July 2025, 2026, doi: 10.1016/j.matchemphys.2025.131412.
[105] M. Hu, W. Tang, S. Lyu, and D. Mo, "Additively Manufactured Micro-/Multi-Scale Porous Copper: Enhanced Mass Transport for High-Performance Hydrogen Evolution," 2026, doi: 10.1021/acs.nanolett.5c04978.
[106] A. I. N. Press, "npj Materials Degradation Article in Press A comparative study on the corrosion resistance of Ti-6Al-4V produced via material extrusion and other additive manufacturing technologies TI ES TI IN Abstract," no. June 2025, 2026.
[107] N. T. Aboulkhair, N. M. Everitt, I. Ashcroft, and C. Tuck, "Reducing porosity in AlSi10Mg parts processed by selective laser melting ☆," *Addit. Manuf.*, vol. 1–4, pp. 77–86, 2014, doi: 10.1016/j.addma.2014.08.001.
[108] K. Loic *et al.*, "Porosity formation from disrupted gas flow in laser powder bed fusion of 316 stainless steel," *J. Manuf. Process.*, vol. 90, no. February, pp. 333–340, 2023, doi: 10.1016/j.jmapro.2022.12.032.
[109] X. Yuan, Y. Zhang, X. Chen, S. Su, M. Deng, and W. Li, "Porosity evaluation of additive manufacturing components by deep learning-assisted nonlinear ultrasonic technique Porosity evaluation of additive manufacturing components by deep learning-assisted nonlinear ultrasonic technique".
[110] F. Yu *et al.*, "Hierarchically ordered porous transition metal compounds from one-pot type 3D printing approaches," 2025.
[111] S. Zhao *et al.*, "Additive manufacturing of silica aerogels," *Nature*, vol. 584, no. August, 2020, doi: 10.1038/s41586-020-2594-0.

[112] N. Kamboj, M. A. Rodríguez, R. Rahmani, and K. Gokuldoss, "Bioceramic scaffolds by additive manufacturing for controlled delivery of the antibiotic vancomycin," pp. 185–190, 2019.

[113] B. Chen, Q. Jiang, and J. Jiang, "Direct Ink Writing Additive Manufacturing of Polyimide Aerogels," pp. 1–29, 2025.

[114] F. Zhang, Y. Ma, J. Liao, V. Breedveld, and R. P. Lively, "Solution-Based 3D Printing of Polymers of Intrinsic Microporosity," vol. 1800274, pp. 1–7, 2018, doi: 10.1002/marc.201800274.

[115] N. Jha, D. P. Mondal, J. D. Majumdar, A. Badkul, A. K. Jha, and A. K. Khare, "Highly porous open cell Ti-foam using NaCl as temporary space holder through powder metallurgy route," *Mater. Des.*, vol. 47, pp. 810–819, 2013, doi: 10.1016/j.matdes.2013.01.005.

[116] S. Su, Z. Hong, Y. Huang, Y. Liu, X. Li, and J. Wu, "Preparation , characterization and designing of porous Ti – 6Al – 4V through metal injection molding without space holder," *J. Mater. Res. Technol.*, vol. 27, no. July, pp. 5651–5661, 2023, doi: 10.1016/j.jmrt.2023.10.269.

[117] R. Nikbakht, R. R. Chromik, and B. Jodoin, "A novel approach for manufacturing cellular metallic structures using pulsed gas dynamic spraying process," *Addit. Manuf.*, vol. 66, no. February, p. 103473, 2023, doi: 10.1016/j.addma.2023.103473.

[118] T. Chen *et al.*, "High speed impact induced dehydrogenation of titanium hydride and formation of cellular structure via cold spray," *Scr. Mater.*, vol. 256, no. November 2024, p. 116443, 2025, doi: 10.1016/j.scriptamat.2024.116443.

[119] Z. L. Zhang, D. Gitardi, M. Scarafile, A. Valente, M. Afrasiabi, and M. Bambach, "Experimental and numerical investigations of pore formation mechanisms in cold spray," *J. Manuf. Process.*, vol. 127, no. April, pp. 488–510, 2024, doi: 10.1016/j.jmapro.2024.08.006.

[120] X. Ye, X. Shi, X. Miao, P. Lu, and M. Wu, "The influence mechanism of fractal design method on mechanical properties and corrosion behavior of sheet Gyroid porous structures formed by LPBF," vol. 41, no. July, 2024.

[121] A. Qadeer *et al.*, "Prediction and control of structured porosity in laser powder bed fusion (LPBF) additive manufacturing using multi-scale modeling ☆," *Mater. Des.*, vol. 258, no. August, p. 114627, 2025, doi: 10.1016/j.matdes.2025.114627.

[122] Y. Xue *et al.*, “Linking LPBF process to pore structure and permeability in stochastically porous AlSi10Mg : towards controllable additive manufacturing,” *Prog. Addit. Manuf.*, vol. 11, no. 1, pp. 649–672, 2026, doi: 10.1007/s40964-025-01369-x.

[123] S. Leonardi, C. Dupuy, P. Peyre, A. Helbert, and M. G. Tarantino, “ScienceDirect Architected metallic metallic cellular cellular materials materials with with random random pore pore features : features : Architected computer design , design , LPBF LPBF fabrication fabrication and and mechanical mechanical properties properties computer,” *Procedia Struct. Integr.*, vol. 53, no. 2023, pp. 327–337, 2024, doi: 10.1016/j.prostr.2024.01.040.

[124] H. Gong, K. Rafi, H. Gu, T. Starr, and B. Stucker, “Analysis of defect generation in Ti – 6Al – 4V parts made using powder bed fusion additive manufacturing processes ☆,” *Addit. Manuf.*, vol. 1–4, pp. 87–98, 2014, doi: 10.1016/j.addma.2014.08.002.

[125] W. E. King *et al.*, “Technology Observation of keyhole-mode laser melting in laser powder-bed fusion additive manufacturing,” *J. Mater. Process. Tech.*, vol. 214, no. 12, pp. 2915–2925, 2014, doi: 10.1016/j.jmatprotec.2014.06.005.

[126] P. J. Withers, I. Todd, and P. B. Prangnell, “The Influence of Porosity on Fatigue Crack Initiation in Additively Manufactured Titanium Components,” *Sci. Rep.*, no. February 2016, pp. 1–13, 2017, doi: 10.1038/s41598-017-06504-5.

[127] C. Lun *et al.*, “The effect of powder oxidation on defect formation in laser additive manufacturing,” *Acta Mater.*, vol. 166, pp. 294–305, 2019, doi: 10.1016/j.actamat.2018.12.027.

[128] S. Romano, A. Brückner-foit, A. Brandão, J. Gumpinger, T. Ghidini, and S. Beretta, “Fatigue properties of AlSi10Mg obtained by additive manufacturing : Defect-based modelling and prediction of fatigue strength,” *Eng. Fract. Mech.*, vol. 187, pp. 165–189, 2018, doi: 10.1016/j.engfracmech.2017.11.002.

[129] D. Shim, J. Seo, H. Yoon, K. Lee, and W. Oh, “Additive manufacturing of porous metals using laser melting of Ti6Al4V powder with a foaming agent Additive manufacturing of porous metals using laser melting of Ti6Al4V powder with a foaming agent”.

[130] T. Debroy *et al.*, “Progress in Materials Science Additive manufacturing of

metallic components – Process , structure and properties," vol. 92, pp. 112–224, 2018, doi: 10.1016/j.pmatsci.2017.10.001.

[131] T. Y. Kwak *et al.*, "Additive manufacturing of a porous titanium layer structure Ti on a Co e Cr alloy for manufacturing cementless implants," *J. Mater. Res. Technol.*, vol. 10, pp. 250–267, 2020, doi: 10.1016/j.jmrt.2020.11.080.

[132] T. Zhao *et al.*, "Some factors affecting porosity in directed energy deposition of," vol. 143, no. June, 2021, doi: 10.1016/j.optlastec.2021.107337.

[133] D. J. Ryu, H. Y. Ban, E. Y. Jung, C. Sonn, and D. H. Hong, "Osteo-Compatibility of 3D Titanium Porous Coating Applied by Direct Energy Deposition (DED) for a Cementless Total Knee Arthroplasty Implant : In Vitro and In Vivo Study," 2020.

[134] C. K. B. El-dasher, G. F. Gallegos, W. E. King, and A. Sisto, "Density of additively-manufactured , 316L SS parts using laser powder-bed fusion at powers up to 400 W," pp. 65–78, 2014, doi: 10.1007/s00170-014-5954-9.

[135] A. J. Pinkerton, "Advances in the modeling of laser direct metal deposition," vol. 15001, no. April 2019, 2025, doi: 10.2351/1.4815992.

[136] S. M. Kelly and S. L. Kampe, "Microstructural Evolution in Laser-Deposited Multilayer Ti-6Al-4V Builds : Part II . Thermal Modeling," vol. 35, no. June, pp. 1869–1879, 2004.

[137] T. Lee, J. Hyung, S. L. Semiatin, and C. Soo, "Materials Science & Engineering A Internal-variable analysis of high-temperature deformation behavior of Ti – 6Al – 4V : A comparative study of the strain-rate-jump and load-relaxation tests," *Mater. Sci. Eng. A*, vol. 562, pp. 180–189, 2013, doi: 10.1016/j.msea.2012.11.023.

[138] F. Martina, P. A. Colegrove, S. W. Williams, and J. Meyer, "Microstructure of Interpass Rolled Wire + Arc Additive Manufacturing Ti-6Al-4V Components," *Metall. Mater. Trans. A*, vol. 46, no. 12, pp. 6103–6118, 2015, doi: 10.1007/s11661-015-3172-1.

[139] X. Wei, H. Zhou, and S. Cong, "Materials Science & Engineering A Microstructure and performance nonuniformity in cold spray additive manufacturing of titanium , copper , and aluminum ☆," *Mater. Sci. Eng. A*, vol. 956, no. January, p. 149903, 2026, doi: 10.1016/j.msea.2026.149903.

[140] J. Wen, Y. Dan, X. Liu, and H. Li, "Promoting microalgal biofilm formation by crushed oyster shell-hydroxyapatite layer on micropatterned aluminum coating for

heavy metal ions removal," *Colloids Surfaces B Biointerfaces*, vol. 243, no. September 2023, p. 114168, 2024, doi: 10.1016/j.colsurfb.2024.114168.

[141] T. Liao *et al.*, "Surface Characteristics and Bone Biocompatibility of Cold-Sprayed Porous Titanium on Polydimethylsiloxane Substrates," 2023, doi: 10.1021/acsbiomaterials.2c01506.

[142] W. Li, H. Liao, C. Li, G. Li, C. Coddet, and X. Wang, "On high velocity impact of micro-sized metallic particles in cold spraying," vol. 253, pp. 2852–2862, 2006, doi: 10.1016/j.apsusc.2006.05.126.

[143] R. Jenkins, S. Yin, B. Aldwell, M. Meyer, and R. Lupoi, "Journal of Materials Science & Technology New insights into the in-process densification mechanism of cold spray Al coatings : Low deposition efficiency induced densification," *J. Mater. Sci. Technol.*, vol. 35, no. 3, pp. 427–431, 2019, doi: 10.1016/j.jmst.2018.09.045.

[144] W. Li, C. Zhang, X. P. Guo, G. Zhang, H. L. Liao, and C. Coddet, "Deposition characteristics of Al – 12Si alloy coating fabricated by cold spraying with relatively large powder particles," vol. 253, pp. 7124–7130, 2007, doi: 10.1016/j.apsusc.2007.02.142.

[145] Y. Wang, J. Adrien, and B. Normand, "Porosity characterization of cold sprayed stainless steel coating using three-dimensional X-ray microtomography," *Coatings*, vol. 8, no. 9, 2018, doi: 10.3390/COATINGS8090326.

[146] J. Gu, J. Ding, S. W. Williams, H. Gu, and P. Ma, "The effect of inter-layer cold working and post-deposition heat treatment on porosity in additively manufactured aluminum alloys," vol. 230, pp. 26–34, 2016.

[147] B. Zhang, Y. Li, and Q. Bai, "Defect Formation Mechanisms in Selective Laser Melting : A Review," *Chinese J. Mech. Eng.*, vol. 30, no. 3, pp. 515–527, 2017, doi: 10.1007/s10033-017-0121-5.

[148] I. Journal, E. Manufacturing, and A. Manuscript, "Recent advances in metal hybrid additive manufacturing: a comprehensive review," 2026.

[149] S. Eshraghi and S. Das, "Mechanical and microstructural properties of polycaprolactone scaffolds oriented porous architectures produced by selective laser sintering," *Acta Biomater.*, vol. 6, no. 7, pp. 2467–2476, 2010, doi: 10.1016/j.actbio.2010.02.002.

[150] Z. Zhang, G. Liu, A. Wang, J. Su, Y. Ding, and J. Ning, “Journal of Alloys and Metallurgical Systems The effects of selective laser melting (SLM) process parameters on the microstructure and mechanical properties of FeCrMnNi nitrogen-containing stainless steel,” *J. Alloy. Metall. Syst.*, vol. 10, no. April, p. 100181, 2025, doi: 10.1016/j.jalmes.2025.100181.

[151] Y. Wang, C. Chang, P. Liu, and C. Lin, “Feasibility evaluation of a new lattice for porous surface design in additive manufacturing medical implants under interfacial tensile bonded testing,” *Addit. Manuf.*, vol. 66, no. July 2022, p. 103455, 2023, doi: 10.1016/j.addma.2023.103455.

[152] T. Alloy *et al.*, “The Effect of Process-Induced Porosity on Fatigue Properties of,” 2022.

[153] T. De Terris *et al.*, “Optimization and comparison of porosity rate measurement methods of Selective Laser Melted metallic parts,” *Addit. Manuf.*, vol. 28, no. September 2018, pp. 802–813, 2019, doi: 10.1016/j.addma.2019.05.035.

[154] O. Surgery, “Development and Verification of a Porous Acetabular Shell Design Manufactured Using Additive Technology M AHWAH , N EW J ERSEY R OBIN S TAMP , P H D M AHWAH , N EW J ERSEY M AHWAH , N EW J ERSEY ABSTRACT,” vol. 34.

[155] Z. Min, “Experimental Investigation on Additively Manufactured Transpiration and Film Cooling Structures,” vol. 141, no. March, pp. 1–10, 2019, doi: 10.1115/1.4042009.

[156] Y. Liang *et al.*, “High-Strength micro-close d-cell aluminum foams fabricate d by laser additive manufacturing and reactive foaming,” *J. Mater. Sci. Technol.*, vol. 263, pp. 261–272, 2026, doi: 10.1016/j.jmst.2025.11.002.

[157] T. Chen, J. Lan, Z. Xing, Z. Cao, and D. Dai, “International Journal of Refractory Metals and Hard Materials Dual laser-powder bed fusion additive manufacturing of difficult-to-process 98W composite porous structures : Porosity-microstructure evolution and compressive properties,” *Int. J. Refract. Met. Hard Mater.*, vol. 137, no. November 2025, p. 107675, 2026, doi: 10.1016/j.ijrmhm.2026.107675.

[158] S. Li *et al.*, “Evaporative cooling of additive manufacturing-assisted metal porous structure under high heat flux,” *Int. J. Heat Mass Transf.*, vol. 258, no. October 2025, p. 128307, 2026, doi: 10.1016/j.ijheatmasstransfer.2025.128307.

[159] K. Ni, Q. Li, and M. Huang, “NDT and E International Ultrasonic characterisation of process-induced pores in selective laser melted TiB 2 / Al composites,” vol. 160, no. September 2025, 2026.

[160] S. Trivedi, R. C. Fernandes, and G. Agarwal, “Hydrogen porosity modelling and material characterization of wire arc additively manufactured hypoeutectic Al – Si alloy,” *Prog. Addit. Manuf.*, vol. 11, no. 1, pp. 627–647, 2026, doi: 10.1007/s40964-025-01368-y.

[161] X. Hou *et al.*, “The fracture mechanism of Al – Mg-Sc-Zr alloy with high-Sc content fabricated by wire arc additive manufacturing,” *J. Mater. Res. Technol.*, vol. 40, no. January, pp. 3816–3830, 2026, doi: 10.1016/j.jmrt.2026.01.089.

[162] T. Ledwaba, K. Moore, D. Kouprianoff, and C. Steenkamp, “Increased warping associated with lack of fusion porosity in additively manufactured PBFLB / Ti6Al4V cantilevers,” *Prog. Addit. Manuf.*, vol. 11, no. 1, pp. 205–231, 2026, doi: 10.1007/s40964-025-01342-8.

[163] B. Ching and M. W. Fu, “Unraveling of the statistical correlation between porosity , permeability and diffusivity of cold-sprayed Ti6Al4V,” vol. 152, no. October 2024, pp. 375–389, 2025, doi: 10.1016/j.jmapro.2025.08.028.

[164] M. Fakourihassanabadi *et al.*, “Fabrication of a Ti-based 3D porous transport layer for PEMWEs using ShockWave-induced spraying and cold spray,” *Surf. Coat. Technol.*, vol. 477, no. October 2023, p. 130353, 2024, doi: 10.1016/j.surfcoat.2023.130353.

[165] D. S. Bolintineanu *et al.*, “Quantifying Pore Morphology in Spray-Formed Tantalum Using X-ray Micro-computed Tomography,” *Metall. Mater. Trans. A*, vol. 54, no. 10, pp. 4100–4127, doi: 10.1007/s11661-023-07156-z.

[166] K. Wathanyu, K. Tuchinda, S. Daopiset, and S. Sirivisoot, “Corrosion resistance and biocompatibility of cold-sprayed titanium on 316L stainless steel,” *Surf. Coat. Technol.*, vol. 445, no. May, p. 128721, 2022, doi: 10.1016/j.surfcoat.2022.128721.

[167] S. Weiller, D. Francesco, W. François, and T. Alain, “Influence of Porosity on Ultra - High Vacuum Gas - Tightness in Cold - Sprayed Aluminum Coatings,” *Transp. Porous Media*, vol. 144, no. 2, pp. 339–366, 2022, doi: 10.1007/s11242-022-01806-3.

[168] Y. Zhang *et al.*, “Review of recent advancing pool boiling heat transfer through

surface engineering," *Renew. Sustain. Energy Rev.*, vol. 230, no. December 2025, p. 116734, 2026, doi: 10.1016/j.rser.2026.116734.

[169] B. Bhusan, R. Lochan, and M. Kumar, "Progress in Nuclear Energy A critical analysis of correlations for saturated nucleate pool-boiling heat transfer over vertical tubes and tube bundles : Development of improved models," *Prog. Nucl. Energy*, vol. 190, no. June 2025, p. 105893, 2026, doi: 10.1016/j.pnucene.2025.105893.

[170] X. Zhang, J. Wan, N. Rensch, and X. Cheng, "Progress in Nuclear Energy Assessment and experimental validation of the new wall boiling heat transfer model under different boundary conditions," *Prog. Nucl. Energy*, vol. 191, no. March 2025, p. 106043, 2026, doi: 10.1016/j.pnucene.2025.106043.

[171] V. K. Dhir, "Boiling heat transfer," *Annu. Rev. Fluid Mech.*, vol. 30, no. 1, pp. 365–401, 1998.

[172] J. Zhou, W. Xu, N. Zhao, and X. Liu, "Annals of Nuclear Energy The radiation-induced effects on the surface structure , wettability and boiling characteristics of heat transfer surfaces : a review," *Ann. Nucl. Energy*, vol. 227, no. PB, p. 112019, 2026, doi: 10.1016/j.anucene.2025.112019.

[173] J. Rogiers, I. T. Jollyn, J. Nonneman, and M. De Paepe, "Flow boiling under non-uniform or time-varying heat flux conditions : a review," *Int. J. Heat Mass Transf.*, vol. 257, no. May 2025, p. 128134, 2026, doi: 10.1016/j.ijheatmasstransfer.2025.128134.

[174] H. Tian, B. Zhang, T. Cong, X. Wang, and M. Cai, "Numerical simulation of the effect of micro-layer slopes on bubble growth and heat transfer during nucleate pool boiling," *Prog. Nucl. Energy*, vol. 191, no. August 2025, p. 106017, 2026, doi: 10.1016/j.pnucene.2025.106017.

[175] Y. Yao *et al.*, "Experimental study on two-phase heat transfer enhancement in narrow rectangular channels during reflooding process," *Prog. Nucl. Energy*, vol. 193, no. December 2025, p. 106207, 2026, doi: 10.1016/j.pnucene.2025.106207.

[176] G. Wang, Y. Liu, X. Liu, X. Chai, and T. Zhang, "Heat transfer transition of fuel rod caused by CRUD growth," vol. 220, no. April 2025, 2026.

[177] Y. Hou, X. Liu, and H. Wang, "Numerical simulation of liquid film heat transfer in nucleate boiling zone caused by droplet impact," *Ann. Nucl. Energy*, vol. 226,

no. April 2025, p. 111800, 2026, doi: 10.1016/j.anucene.2025.111800.

[178] J. Farrell, E. T. Hurlburt, and A. Mahvi, "A comprehensive review of nucleate boiling fundamentals applied to thin film annular flow," vol. 118, no. January 2025, 2026, doi: 10.1016/j.ijheatfluidflow.2025.110199.

[179] Q. Wang, H. Hsieh, X. Cai, S. Wang, K. Li, and C. Lin, "Heat transfer enhancement using different Ag / GPE nanofluid mixing conditions on a downward-facing heating surface," *Prog. Nucl. Energy*, vol. 190, no. June 2025, p. 106012, 2026, doi: 10.1016/j.pnucene.2025.106012.

[180] A. Fazeli and S. Moghaddam, "A New Paradigm for Understanding and Enhancing the Critical Heat Flux (CHF) Limit," *Sci. Rep.*, vol. 7, no. 1, pp. 1–12, 2017, doi: 10.1038/s41598-017-05036-2.

[181] S. Dong and T. Hibiki, "Effect of channel geometry on the onset of significant void and void fraction profiles of vertical upward boiling flows," *Prog. Nucl. Energy*, vol. 194, no. January, p. 106256, 2026, doi: 10.1016/j.pnucene.2026.106256.

[182] S. Niu, J. Bi, Y. Li, and G. Lu, "Prediction of critical heat flux and position in narrow rectangular channels using deep feed-forward neural networks coupling with empirical correlations," *Int. J. Heat Mass Transf.*, vol. 221, no. December 2023, 2024, doi: 10.1016/j.ijheatmasstransfer.2023.125042.

[183] D. Zhao, J. P. Duarte, W. Liu, M. L. Corradini, J. Wang, and J. Bi, "DNB type critical heat flux prediction in rod bundles with simplified grid spacer based on Liquid Sublayer Dryout model," *Nucl. Eng. Des.*, vol. 351, no. February, pp. 94–105, 2019, doi: 10.1016/j.nucengdes.2019.05.012.

[184] H. Yeom *et al.*, "Pool boiling critical heat flux studies of accident tolerant fuel cladding materials," *Nucl. Eng. Des.*, vol. 370, no. July, p. 110919, 2020, doi: 10.1016/j.nucengdes.2020.110919.

[185] X. Yuan, J. Su, Y. Du, Y. Lin, J. Shi, and C. Wang, "Separated liquid-vapor pathways for pool boiling enhancement with ultra-high heat flux : a critical review," *Renew. Sustain. Energy Rev.*, vol. 230, no. December 2025, p. 116675, 2026, doi: 10.1016/j.rser.2025.116675.

[186] J. Song, L. Lei, N. Zhou, and J. Zhang, "Research Progress on Heat Transfer of Herringbone Plate Heat Exchangers Under Single-Phase / Two-Phase Flow," 2026.

[187] N. Xu, Z. Liu, X. Yu, J. Gao, and H. Chu, "Processes, models and the influencing

factors for enhanced boiling heat transfer in porous structures," *Renew. Sustain. Energy Rev.*, vol. 192, no. November 2023, p. 114244, 2024, doi: 10.1016/j.rser.2023.114244.

[188] Y. Yuan, Z. Ma, Y. Ma, Z. Zhou, and L. Zhang, "Experimental study on geyser boiling parameter characteristics in vertical sodium heat pipes," *Prog. Nucl. Energy*, vol. 194, no. January, p. 106270, 2026, doi: 10.1016/j.pnucene.2026.106270.

[189] M. Song, Z. Chen, J. Xia, H. Li, W. Xu, and X. Liu, "Prediction of post-dryout heat transfer based on physics-embedded machine learning with Bayesian optimization algorithm," *Prog. Nucl. Energy*, vol. 194, no. January, p. 106263, 2026, doi: 10.1016/j.pnucene.2026.106263.

[190] P. Barmavatu, J. Heeraman, M. Kumar, D. Ramalinga, and V. Mangalaraja, "Synergistic integration of micro - channels and thermal storage systems for energy efficiency enhancement in heat transfer applications - a critical review," *J. Therm. Anal. Calorim.*, 2025, doi: 10.1007/s10973-025-15165-w.

[191] H. A. Nabwey, "Exploring the Effects of Reduced Gravitational Field Impacts on Convective Heat Transfer : A Comprehensive Review," pp. 764–774, 2026, doi: 10.1002/htj.70106.

[192] S. Nukiyama, "The maximum and minimum values of the heat a transmitted from metal to boiling water under atmospheric pressure," *Int. J. Heat Mass Transf.*, vol. 9, no. 12, pp. 1419–1433, 1966.

[193] N. Zuber, "Hydrodynamic Aspects Of Boiling Heat Transfer," 1959. doi: 10.2172/4175511.

[194] B. Chu *et al.*, "Hybrid graphene oxide/crumpled graphene film via subcooled boiling-induced self-assembly for highly efficient boiling heat transfer," *Mater. Today Energy*, vol. 22, p. 100868, 2021, doi: 10.1016/j.mtener.2021.100868.

[195] B. Hou, C. Wu, X. Li, J. Huang, and M. Chen, "Contact line-based model for the Cassie-Wenzel transition of a sessile droplet on the hydrophobic micropillar-structured surfaces," *Appl. Surf. Sci.*, vol. 542, no. September 2020, p. 148611, 2021, doi: 10.1016/j.apsusc.2020.148611.

[196] M. Calati *et al.*, "Water pool boiling in metal foams: From experimental results to a generalized model based on artificial neural network," *Int. J. Heat Mass Transf.*,

vol. 176, p. 121451, 2021, doi: 10.1016/j.ijheatmasstransfer.2021.121451.

[197] Y. Yang, X. Ji, and J. Xu, "Effect of inclination angle on the pool boiling heat transfer of ultra-light copper foams," *Heat Mass Transf. und Stoffuebertragung*, vol. 46, no. 7, pp. 695–706, 2010, doi: 10.1007/s00231-010-0620-8.

[198] Y. Shah, H. G. Kim, W. W. Choi, and S. M. Kim, "Experimental pool boiling study on novel multistage cross-flow porous structure using FC-72 for high-heat-flux electronic applications," *Int. J. Heat Mass Transf.*, vol. 213, 2023, doi: 10.1016/j.ijheatmasstransfer.2023.124270.

[199] S. Mori, F. Yokomatsu, and Y. Utaka, "Enhancement of critical heat flux using spherical porous bodies in saturated pool boiling of nanofluid," *Appl. Therm. Eng.*, vol. 144, no. 135, pp. 219–230, 2018, doi: 10.1016/j.applthermaleng.2018.08.047.

[200] L. Abu-farah and N. Germann, "Temperature-driven phase change : boiling and condensation," *Open Transp.*, vol. 1, no. 1, pp. 1–28, 2026, doi: 10.1515/ot-2026-0001.

[201] B. Suriyaprasaad, A. Upadhyay, A. Thakur, and R. Raj, "A roadmap for decoding the sound of boiling," 2026.

[202] L. Du, X. Chen, Q. Cheng, W. Zhang, J. Sun, and W. Cai, "Transient numerical studies on Departure from Nucleate Boiling (DNB) crisis in petal-shape fuel rod bundle assembly," *Prog. Nucl. Energy*, vol. 191, no. May 2025, p. 106025, 2026, doi: 10.1016/j.pnucene.2025.106025.

[203] Z. Ma, Z. Zhou, L. Zhang, Y. Ma, and S. Tang, "Experimental study on nucleation superheat-pressure evolution and its impact on geyser boiling characteristics in sodium heat pipes," *Prog. Nucl. Energy*, vol. 192, no. November 2025, p. 106096, 2026, doi: 10.1016/j.pnucene.2025.106096.

[204] F. T. Xia *et al.*, "Numerical investigation of critical heat flux in single rod channel under extremely low flow conditions," *Prog. Nucl. Energy*, vol. 190, no. March 2025, p. 105980, 2026, doi: 10.1016/j.pnucene.2025.105980.

[205] S. Dong and T. Hibiki, "Modeling flow quality for predicting axial void fraction development of boiling flows in rectangular channels at elevated pressure conditions," *Prog. Nucl. Energy*, vol. 194, no. January, p. 106255, 2026, doi: 10.1016/j.pnucene.2026.106255.

[206] J. Chen *et al.*, "Thermal design of asymmetrical layout in printed circuit steam

generators for molten salt-cooled high temperature reactor," *Prog. Nucl. Energy*, vol. 193, no. January, p. 106225, 2026, doi: 10.1016/j.pnucene.2025.106225.

[207] X. Chen *et al.*, "Response of steam generator thermal-hydraulic characteristics under seismic loading," *Prog. Nucl. Energy*, vol. 192, no. February 2025, p. 106161, 2026, doi: 10.1016/j.pnucene.2025.106161.

[208] J. Zhao, Y. Dai, W. Tao, and Y. Wang, "A review of heat removal technologies across heat flux frontiers : From high to ultra high level," *Int. Commun. Heat Mass Transf.*, vol. 172, no. P5, p. 110516, 2026, doi: 10.1016/j.icheatmasstransfer.2026.110516.

[209] J. Shi *et al.*, "Progress in Nuclear Energy Thermal fluid solid interaction numerical research of casing tube once-through steam generator ☆," *Prog. Nucl. Energy*, vol. 191, no. July 2025, p. 106082, 2026, doi: 10.1016/j.pnucene.2025.106082.

[210] N. Fan, "Solid-state Deposition of Bulk Metallic Glass and High-entropy Alloy via Cold Spray," 2024.

[211] V. K. Champagne, D. J. Helfritch, S. P. G. Dinavahi, and P. F. Leyman, "Theoretical and Experimental Particle Velocity in Cold Spray," vol. 20, no. March, pp. 425–431, 2011, doi: 10.1007/s11666-010-9530-z.

[212] R. Falco and S. Bagherifard, "Cold Spray Additive Manufacturing: A Review of Shape Control Challenges and Solutions," *J. Therm. Spray Technol.*, vol. 34, no. 4, pp. 1023–1041, 2025, doi: 10.1007/s11666-025-01970-0.

[213] Y. Chen *et al.*, "Nucleate pool boiling enhancement on Ti64 cold spray additive manufacturing coatings," *Appl. Therm. Eng.*, vol. 277, no. December 2024, p. 127126, 2025, doi: 10.1016/j.applthermaleng.2025.127126.

[214] R. J. MacNamara, T. L. Lupton, R. Lupoi, and A. J. Robinson, "Enhanced nucleate pool boiling on copper-diamond textured surfaces," *Appl. Therm. Eng.*, vol. 162, no. June, p. 114145, 2019, doi: 10.1016/j.applthermaleng.2019.114145.

[215] R. V. Umretiya, B. Elward, D. Lee, M. Anderson, R. B. Rebak, and J. V. Rojas, "Mechanical and chemical properties of PVD and cold spray Cr-coatings on Zircaloy-4," *J. Nucl. Mater.*, vol. 541, pp. 50–65, 2020, doi: 10.1016/j.jnucmat.2020.152420.

[216] A. Elkholy and R. Kempers, "Enhancement of pool boiling heat transfer using 3D-printed polymer fixtures," *Exp. Therm. Fluid Sci.*, vol. 114, no. January, p. 110056,

2020, doi: 10.1016/j.expthermflusci.2020.110056.

[217] L. Y. X. Lum, P. Liu, and J. Y. Ho, "Micro/nanostructuring of metal additively manufactured aluminum alloy for enhanced pool boiling of dielectric fluids," *Int. J. Heat Mass Transf.*, vol. 221, no. November 2023, p. 125090, 2024, doi: 10.1016/j.ijheatmasstransfer.2023.125090.

[218] H. Liu, C. Zhang, J. Wang, and L. Zhang, "Critical heat flux enhancement using composite porous structure produced by selective laser melting," *Appl. Therm. Eng.*, vol. 197, no. April, p. 117396, 2021, doi: 10.1016/j.applthermaleng.2021.117396.

Supplementary materials

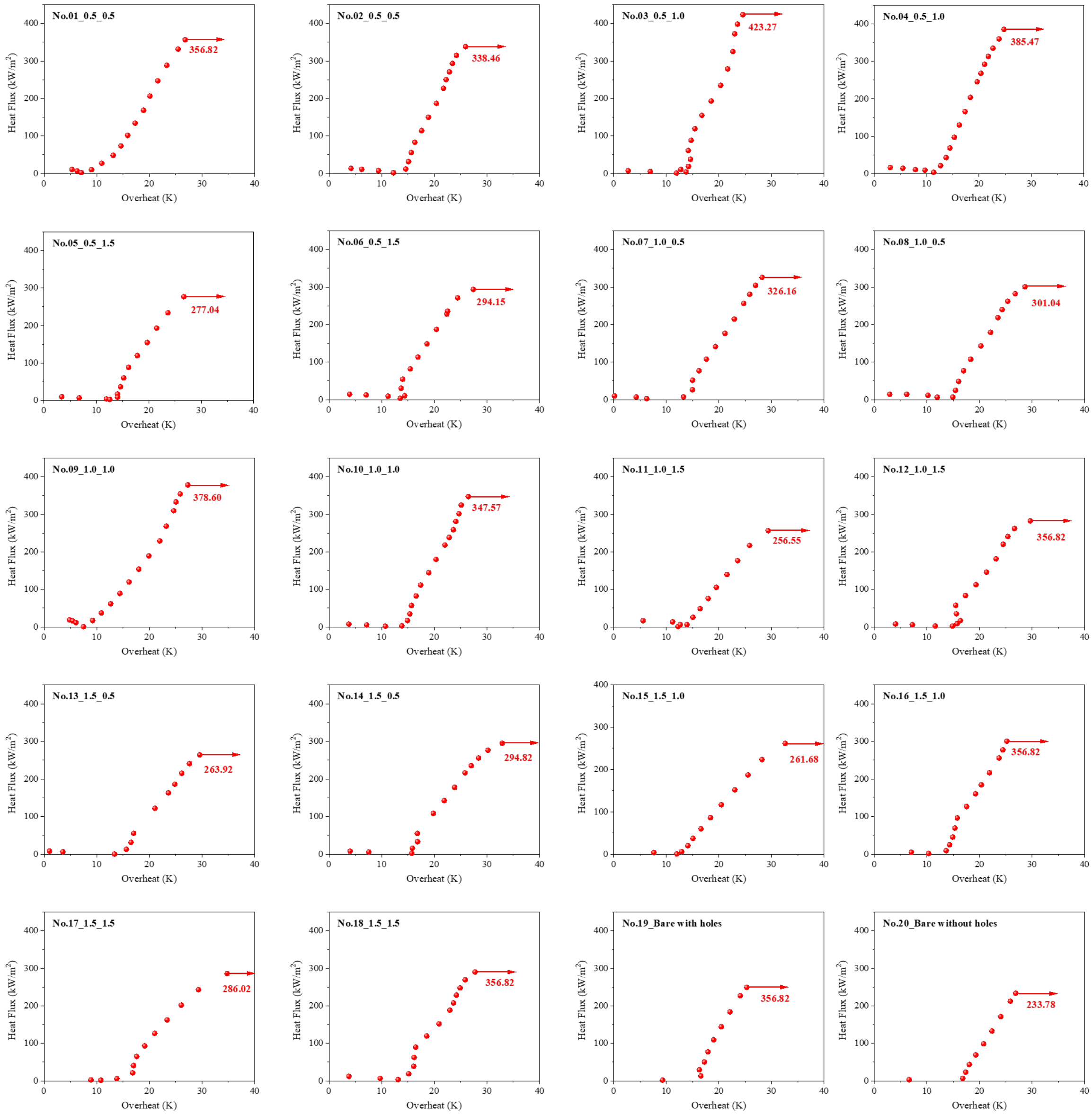

Figure. 50 Boiling curve test results for all samples